$BaTiO_3$-$NaNbO_3$ based solid solutions for high field, temperature-stable multilayer ceramic capacitors

By:

Yongbo Fan

Supervisors:

Prof. Ian M. Reaney

Prof. Derek C. Sinclair

A thesis submitted in partial fulfilment of the requirements for the degree of

Doctor of Philosophy

Department of Materials Science and Engineering

Faculty of Engineering

The University of Sheffield

July 2023

Acknowledgements

I wish to express my sincere gratitude to my supervisor Prof. Ian Reaney for his supervision and continuous guidance through my PhD project. His insight into material science and wisdom of life has been very inspiring to me during the past few years. I shall remember his teaching for the rest of my life.

I would like to thank my co-supervisor Prof. Derek Sinclair for his guidance with analysing the electrical measurement data. I have learned a lot from his insightful understanding and perspectives of analysing and interpreting the data.

I am very thankful to Dr. Zhilun Lu for his kind support and guidance with the experimental work at the beginning of this project. My sincere gratitude goes to Dr. Ge Wang for his guidance during the project and helps with the experiments. I would like to thank Dr. Xinzhen Wang for his support and advice during the project. I would like to thank Prof. Dawei Wang for helping with the electrical measurement in the project. I would like to thank Prof. Antonio Feteira at Sheffield Hallam University for providing the access to the ferroelectric measurement system. I appreciate very much the help of Dr. Edoardo Mantheakis with the device fabrication work. I would also like to thank the colleagues of our lab for their support and helpful discussions. I would like to thank the supporting stuffs in our department for their effort to run the facilities, allowing smooth environment for research to take place.

I am very grateful to my Parents for supporting me to pursue a PhD degree in Sheffield. It's an unforgettable experience of my life. I am very grateful to my wife, Shuling, for her loving accompany and constant support for me in life.

Publications:

Yongbo Fan, Xinzhen Wang, Hongtian Li, Antonio Feteira, Dawei Wang, Ge Wang, Derek C. Sinclair, Ian M. Reaney; Pb, Bi, and rare earth free X6R barium titanate–sodium niobate ceramics for high voltage capacitor applications. Appl. Phys. Lett., 122(14), 2023, 143901.

Yongbo Fan, Weijia Wang and Dengwei Hu, Structural control of plate-like $NaNbO_3$ via topochemical synthesis, 2021 IEEE International Symposium on Applications of Ferroelectrics (ISAF), 2021, pp. 1-3

Xinzhen Wang, **Yongbo Fan**, Bin Zhang, Ali Mostaed, Linhao Li, Antonio Feteira, Dawei Wang, Derek C. Sinclair, Ge Wang, Ian M. Reaney, High discharge energy density in novel $K_{1/2}Bi_{1/2}TiO_3$-$BiFeO_3$ based relaxor ferroelectrics, J. Euro. Ceram. Soc., 42(15), 2022, 7381-7387

Conferences attended:

"Sodium niobate – barium titanate based electroceramics for electrical energy storage application" 9th International Conference on Materials Science & Smart Materials, Reggio Emilia, Italy, June, 2023.

"Templated growth of $NaNbO_3$ crystal with Aurivillius compounds" Materials Science and Engineering Congress 2022, Damstadt, Germany, September, 2022.

"Donor/Acceptor doped barium titanate – sodium niobate solid solution for energy storage applications" 8th International Conference on Materials Science & Smart Materials, London, UK, July, 2022

"The effect of magnesium doping on barium titanate-sodium niobate solid solutions" 2022 IEEE International Symposium on Applications of Ferroelectrics, Tours, France, July, 2022.

"The structural control of plate-like $NaNbO_3$ crystal via topochemical process" 2021 IEEE International Symposium on Applications of Ferroelectrics, Sydney, Australia, May, 2021.

"Crystal and domain structure of $AgNbO_3$ ceramics" International Forum on Advanced Materials 2020, Xi'an, China, November, 2020.

Nomenclatures

Abbreviations

CN	Coordination number
EDX	Energy-dispersive X-ray spectroscopy
PSA	Particle size analysis
RE	Rare earth ion
XRD	X-ray diffraction
SEM	Scanning electron microscopy
SSR	Solid state reaction
BT	Barium titanate $BaTiO_3$
NN	sodium niobate $NaNbO_3$
AN	Silver niobate $AgNbO_3$
BF	Bismuth ferrite $BiFeO_3$
KNN	Potassium sodium niobate $K_{0.5}Na_{0.5}NbO_3$
ST	Strontium titanate $SrTiO_3$
NBT	Sodium bismuth titanate $Na_{0.5}Bi_{0.5}TiO_3$
YSZ	Yttria-stabilised zirconia
MLCC	Multilayer ceramic capacitor
AFE	antiferroelectric

Symbols

Voltage	V
Current	I
Charge	Q
Area	A
Electrical field strength	E
Ionic radius of element A	r_A
Ionic radius of element B	r_B
Ionic radius of oxygen	r_O
Tolerance factor	t
permittivity	ε
Dielectric loss tangent	tan δ
Polarisation	P
Recoverable energy density	W_{rec}
Total energy density	W_{total}
Energy storage efficiency	η
Density	ρ
Wavelength	λ
Oxygen vacancy	V_O

Abstract

Barium titanate (BT) and sodium niobate (NN) form a complete solid solution across the compositional range. Ti^{4+} and Nb^{5+} are known as 'd^0 ions in which the outer s-shells are full, but the d-shells empty which engenders a large ionic polarizability and therefore permittivity when in octahedral coordination. Previous studies have focused on the low field dielectric performance or the piezoelectric/strain behaviour of this solid solution. To date, there have been few systematic studies of the structure - high field/energy storage performance of the BT-NN solid solution. In this thesis, the BT and NN rich ends are explored with a view to developing next generation, high field and high energy density multilayer ceramic capacitors (MLCCs).

For the BT rich end, a heterogeneous microstructure was present based on two broad anomalies in the permittivity vs. temperature curves. BT10NN was selected to investigate the role of donor and acceptor doping on conductivity. Mg^{2+} ($0 \leq x \leq 0.05$) was used as an acceptor dopant. However, XRD patterns suggest that Mg^{2+} at least in part substituted on the A rather than B-site compensating for Na^{+} loss at low concentrations before entering the B-site at higher values of x (>0.02). As x increased, the conduction mechanism changed from n to p-type for x = 0.02, before reverting to n-type as x increased. Doping with Mg^{2+} further enhanced the temperature-stability to achieve X6R specification in the Electronic Industry Alliance codes. At x > 0.02, a single broad peak was observed in the permittivity vs. temperature data but impedance spectra nonetheless revealed two components in the electrical response. An energy density (W_{rec}) of 3.4 J/cm^3 was achieved with efficiency (η) of 82.6% for x = 0.01 but higher concentrations of Mg^{2+} promoted the formation of oxygen vacancies (n-type behaviour) and led to inferior dielectric performance.

For the NN rich end of the solid solution, the crystal structure transformed from orthorhombic to tetragonal phase with increasing BT concentration ($0 \leq x \leq 0.25$). In addition, the oxygen transport number (t_{ion}) was reduced by two orders of magnitude. Polarisation – Electric field (P-E) response and permittivity-temperature data was obtained for all compositions and based on these measurements, NN15BT and NN25BT were chosen as suitable materials for further optimization. Based on previous work, a third end member ($Nd(Mg_{2/3}Nb_{1/3})O_3$, NMN) was added to the solid solution to decrease the correlation length of polar order.[1] Compositions were pseudocubic for x > 0.02 and phase transitions shifted to below room temperatures. NMN generally suppressed the polarisation but increased E_{max} (maximum pulsed field before breakdown) giving rise to W_{rec} = 3.95 J/cm^2 for NN15BT10NMN ceramics with η = 70.67 % and W_{rec} = 1.62 J/cm^2 and η = 81.43 % for NN25BT10NMN.

Within the explored compositions, Mg doped BT-NN (x = 0.01) showed the highest energy density and best temperature stability and therefore was chosen to fabricate multilayers. Multilayers showed good temperature stability (X6R) and energy storage performance with W_{rec} of 3.36 J/cm^3 and η of 80.6 %, confirming the potential of BT-NN solid solutions for high field MLCC applications, particularly considering that they are Bi, rare-earth as well as Pb free.

Contents

1 Introduction

In this chapter, the concept of a capacitor, the different market categories and the need for higher voltages/energy density are discussed.

1.1 What Is a Capacitor?

1.1.1 Principles of Operation

A capacitor is a device that stores electrical energy between two surfaces which experience a voltage difference. When a capacitor is charged so there is a voltage difference (V) between the positive and negative electrode, its capacitance is defined as:

$$C = \frac{Q}{V} \tag{1.1}$$

where Q is the positive or negative charge accumulated on each electrode. The capacitance provides a direct representation of the ability of a capacitor to store electric charge with a given voltage. In practice, both direct current (DC) and alternating current (AC) signals may be applied to a capacitor in operation, so the differential capacitance (C_d) is also a critical parameter:

$$C_d = \frac{dQ}{dV} \tag{1.2}$$

where dQ and dV are the incremental charge and voltage difference at V. The total energy stored in a charged capacitor is therefore:

$$W = \int_0^Q V(q)dq = \int_0^V C_d dV \tag{1.3}$$

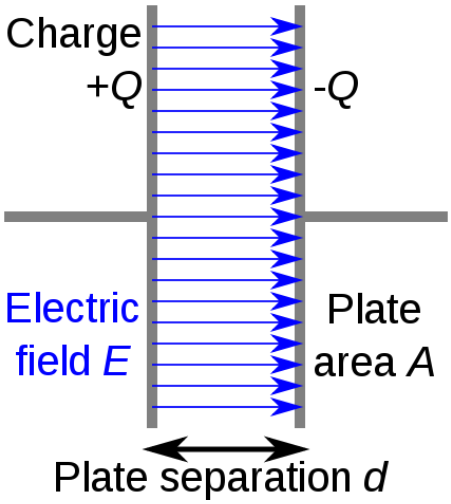

Fig.1.1 Schematic diagram of a parallel plate capacitor with a charge of Q on each plate.

If a simple capacitor is considered that consists of two parallel conductive plates with an area A separated by a layer of dielectric material with thickness d, Gauss's law gives a field strength:

$$E = \frac{\sigma}{\varepsilon} \tag{1.4}$$

where σ is the charge density on the top or bottom surface of the dielectrics, and ε is the permittivity of the dielectrics. By substituting equation (1.4) into equation (1.1), the capacitance is:

$$C = \frac{\sigma A}{dE} = \frac{\varepsilon A}{d} \tag{1.5}$$

Based on equation (1.5), the capacitance may be increased from a material perspective by increasing ε and from a device perspective, the area of electrode can be increased and the thickness of dielectric between the electrodes decreased.

1.1.2 Types of Capacitors

For a capacitor with a conventional isolating layer, the dielectric and electrode have distinctive boundary conditions that follow Gauss's law, equation (1.5). There are mainly three types of such capacitor, the multilayer ceramic (MLCC), the metalised film and the electrolytic capacitor.

MLCCs are composed of many layers of very thin dielectrics and alternating electrodes connecting by two terminal electrodes, equivalent to many small capacitors in parallel. For a given case size, the capacitance is higher if the dielectric layers are thinner, increasing the volumetric efficiency. They are usually small, with a capacitance of 1 pF-100 µF and a working voltage of 5-500 V. The equivalent series resistance (ESR) and equivalent series inductance (ESL) are low for high frequency signals. Their small case size and good electrical performance make them suitable for a wide range of electronic applications.

Metalised film capacitors are made with an organic layer with a thin vacuum deposited metal electrode. Some adopt the same configuration as MLCCs, but the majority are made with two layers of metalized film wound together, taking advantage of the flexible nature of the organics. This configuration provides a large electrode area and thin dielectric layer, which gives a capacitance 1 nF to over 500 µF and a working voltage of 50-2000 V. The thin electrode of such a capacitor is burnt out during electrical breakdown, isolating itself from the rest of the capacitor. This self-healing feature is the main reason for its reliability.

In an electrolytic capacitor, the direction of electric field needs to be fixed during operation, to avoid destroying the dielectric layer. The dielectric of this type of capacitor is formed with a chemical process called anodization. This process enables a large area (A) for the dielectric since it covers the surface of a porous anode. The dielectric layer is thin, giving a large capacitance. A solid or liquid electrolyte covers the dielectric layer and serves as a cathode. They usually have a voltage rating between 10 and 450 V, and a capacitance from 0.1 to 4700 µF.

Supercapacitors consist of an ionic conducting electrolyte with two electrodes. The Helmholtz double layer or the faradaic redox reaction at the electrolyte-electrode interface enables the storage of large amount of electrical energy. These devices store 10-100 times more energy than electrolytic capacitors and deliver charge faster than batteries. Supercapacitors fill the gap between conventional capacitors and batteries in terms of energy storage.

1.2 Market for Capacitors

The global capacitor market size was around $22.1 billion in 2021, and is projected to reach $31.2 billion by 2027, growing at a Compound Annual Growth Rate (CAGR) of 5.9% from 2021 to 2027. [2] According to a report by the Engineering Construction Industry Association (ECIA), ceramic capacitors take up the majority of the market with around 55% share. Aluminium electrolytic capacitors have around 18% market share; tantalum electrolytic capacitors 16%; paper/film capacitors 9% and the rest (2%) are supercapacitors.[3]

The global MLCC market was valued at $11.6 billion in 2021, and is projected to reach $16.6 billion by 2027, with a CAGR of 6.0% from 2022-2027. [4] By 2030, MLCCs in base stations are expected to double to support enhanced network performance (5G/6G). There is also a shift from consumer electronics to computing, with the emergence of the Internet of Things, the cloud and artificial intelligence. Most importantly, the market share of MLCCs used in the automotive industry has experienced significant growth over the past few years, making it comparable with that of consumer electronics [5] The demand for automotive-grade MLCCs is expected to continue for the foreseeable future.

1.3 Need for High Voltage Capacitors

With the move from gasoline to Hybrid Electrical Vehicles (HEVs) and Electrical Vehicle (EVs), car battery voltages have also experienced a significant increase from 12 to 400 V. The increase is expected to continue as the effective capacity of batteries increases and the charging times decrease. [6] MLCCs are preferred for on board electronic and power electronic EV applications due to their small size and high reliability. The demand for automotive-grade MLCC is strong with some used in the powertrains and invertors, driving development toward higher voltages that meet the AEC-Q200 standard. This thesis will explore compositions and MLCC prototypes that have a higher voltage capability than those designed for consumer electronics and by default a high energy density.

2 Literature Review

In this chapter, the scientific background underpinning capacitor technology is presented from structural, crystal chemical, dielectric and ferroelectric perspectives. In addition, consumer $BaTiO_3$ based dielectrics, and Pb and Pb-free high voltage dielectrics are discussed.

2.1 Perovskites and Their Crystal Chemistry

2.1.1 Crystallography

As with all crystal structure types, perovskites may be classified by their symmetries. According to the relative length and angles between each crystal axis, they are divided into seven classes: triclinic, monoclinic, orthorhombic, tetragonal, hexagonal, rhombohedral and cubic.

In the seven crystal classes, primitive lattices have a lattice point on each corner of the cell. When another lattice point is added at the base centre, body centre or face centre, they may be further classified into the 14 Bravais lattices.

Crystal symmetry may also be classified into 32 point groups with the following symmetry operations: (i) reflection; (ii) rotation; (iii) inversion and (iv) improper rotation (which is combined operation of rotation and inversion). If translational operations are included such as (i) screw axes and (ii) glide planes, 230 different symmetries or space groups may be defined.

2.1.2 Perovskite Crystal Chemistry

Perovskite is a class of material with similar crystal structure to $CaTiO_3$, with a chemical formula ABO_3 in which the 12 coordinated A-site is larger than the 6 coordinate B site cation. The stability and distortion of the perovskite structure may be evaluated using the Goldschmidt tolerance factor:

$$t = \frac{r_A + r_o}{\sqrt{2}(r_B + r_O)} \tag{2.1}$$

where r_A, r_B, and r_O are the ionic radii of A, B, and O ions, respectively. When t = 1, a highly symmetric cubic phase is stabilised, e.g. $SrTiO_3$. When t < 1, the A-site ion is too small to support the cubic lattice, and the BO_6 octahedra rotate or tilt to stabilise the structure, e.g. $CaTiO_3$. Some of these materials are not ferroelectric, with symmetry defined only by the octahedral tilting arrangement. In other systems, octahedral tilting combines with polar displacements, such as in the Q phase of Na niobate and in $BiFeO_3$.[7-9] When t > 1, the B site ion is small for octahedral coordination and, particularly if it has a d^0 outer electron shell such as Ti^{4+}, may displace off centre generating a spontaneous polarisation, e.g. $BaTiO_3$. In general, when $0.8 \leq t \leq 1.06$, the perovskite structure is stable but if t is out of this range, an alternative structure forms. [10]

Glazer's notation is used to classify the type of octahedral distortion along three orthogonal directions of a pseudocubic unit cell. [11] a, b and c imply the tilting or rotations are around x, y, z but unequal. Repetition of a letter means tilting is of the same amplitude. Superscripts denote the phase of tilting. A positive sign indicates the neighbouring tilting is in the same direction (in phase); a negative sign indicates that it is in the opposite sense (out of phase).

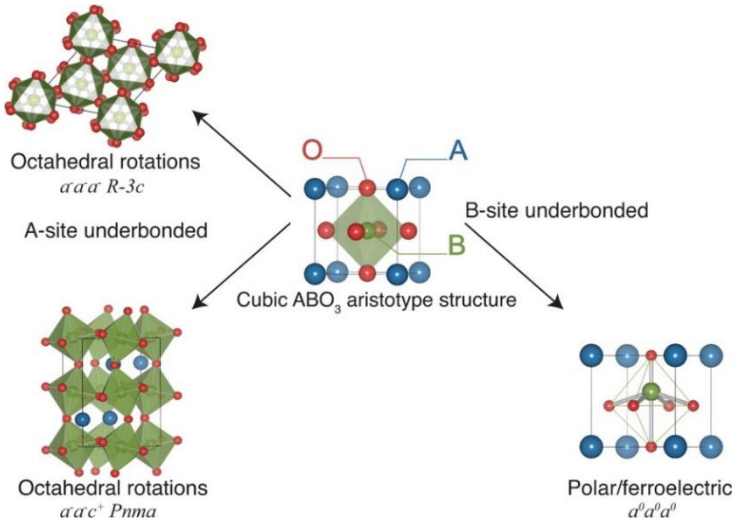

Fig. 2.1 cubic perovskite structure with t = 1, and common structural distortions with t < 1 (left) and t > 1 (right). [12]

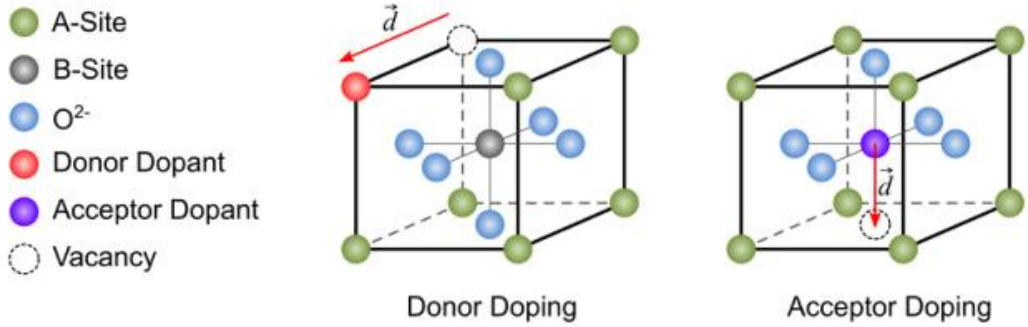

Fig. 2.2 Effect of aliovalent doping in perovskite structure. Red array indicates the defect dipole associate with the particular dopant. [13]

2.1.3 Crystallography of $BaTiO_3$ and $NaNbO_3$

$BaTiO_3$ is a perovskite in rhombohedral phase (R3m) at temperatures below -90 ℃, which transforms into orthorhombic phase (Amm2) with increased temperature, then to a tetragonal phase (P4mm) at 5 ℃, and finally to a cubic phase ($Pm\bar{3}m$) at 120 ℃. [14] It is a ferroelectric material at room temperature, with Ti^{4+} displacement contributing to the spontaneous polarisation. [15] The large ionic radius of the A-site ion, Ba^{2+}, in comparison with the B-site Ti^{4+}, gives rise to a large tolerance factor and encourages a large off-centre displacement of Ti^{4+} at the paraelectric to ferroelectric phase transition, as illustrated in Fig.2.1.

$NaNbO_3$ is a perovskite which undergoes several phase transitions from -100 to 640 ℃. [16] At room temperature it is dominantly in the antiferroelectric, P phase (Pbcm) but there are almost always trace amounts of the ferroelectric Q phase ($Pmc2_1$) which has a similar free energy. At high temperature it transforms to the antiferroelectric R phase (Pnma). The structure of P, Q and R phases are shown in Fig. 2.3. With higher temperature, the structure is transformed into paraelectric T phase and finally to the paraelectric C phase. [17]

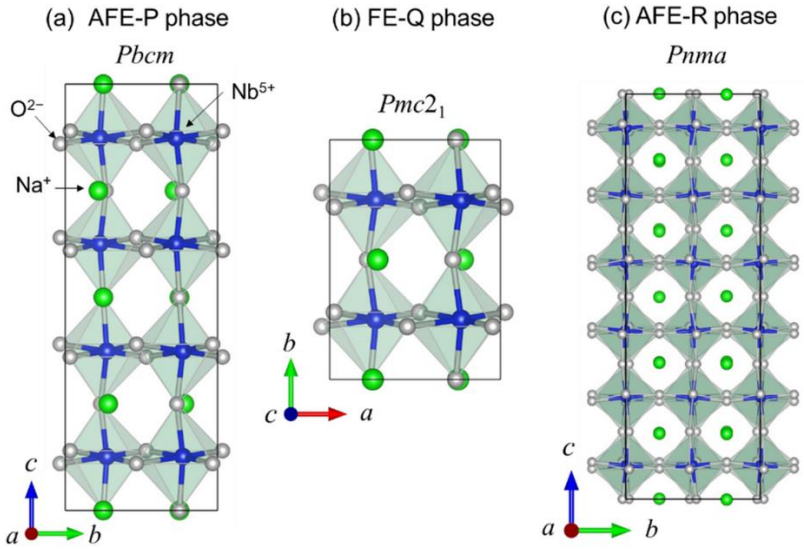

Fig. 2.3 Crystal structure of $NaNbO_3$ in (a) AFE-P phase with Pbcm space group, (b) FE-Q phase with $Pmc2_1$ space group, (c) AFE-R phase with Pnma space group.[18]

2.1.4 Dopants in Perovskites

In perovskites, doping is a very effective strategy to tune the structure and functional properties of the material. Dopants enter the A or B site of the perovskite depending on their ionic radius and that of the ions occupying the sites in the parent structure. When the dopant ion is isovalent, no additional site vacancy is created to keep charge neutrality. However, when the dopant is aliovalent, site vacancies are usually present to maintain charge neutrality. For donor doping, A or B site vacancies are expected. For acceptor doping, oxygen vacancies are expected.

As shown in Fig. 2.2, the dopant – cation/anion vacancy may bind with each other to form a defect dipole. However, the likelihood for the defect dipoles to form is dependent on their binding energy. Generally, the acceptor-oxygen vacancy pairs are more likely to bind, while the donor-cation vacancy pairs dissociate easily. [19, 20] Defect migration under field and the effect of defect dipoles on domain wall movement are both important factors impacting on the functional properties of the material. [21]

2.2 Theory of Dielectrics, Ferroelectrics and Relaxors

Dielectrics are electrical insulators which store electrical energy in the form of polarisation. The various types of polarisations are shown in Fig. 2.3: electronic, orientation (dipolar in ferroelectrics), ionic and interfacial/electrode polarisation.

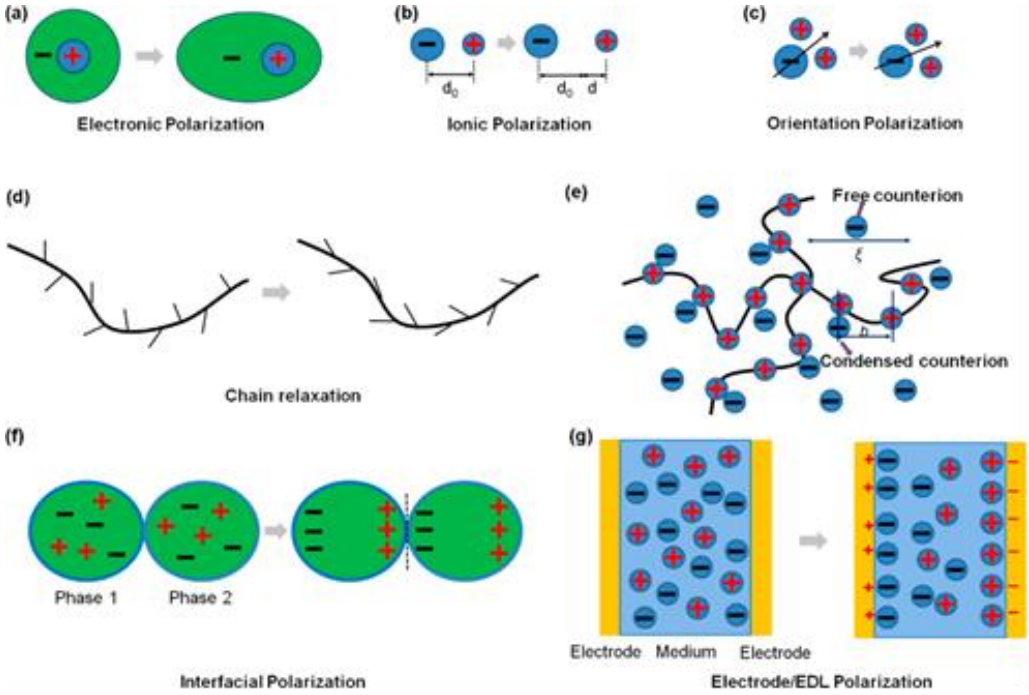

Fig. 2.4 Schematic diagrams of (a) electronic polarisation, (b) ionic polarisation, (c) orientation polarisation, (d) chain relaxation polarisation, (e) free counterion and condensed counterion polarisations in a polyelectrolyte, (f) interfacial polarisation, and (g) electrode or electric double layer (EDL) polarisation. [22]

Polarisation (P) and permittivity (ε) are described by:

$$P = \varepsilon E \tag{2.2}$$

where E is the electric field applied to the material.

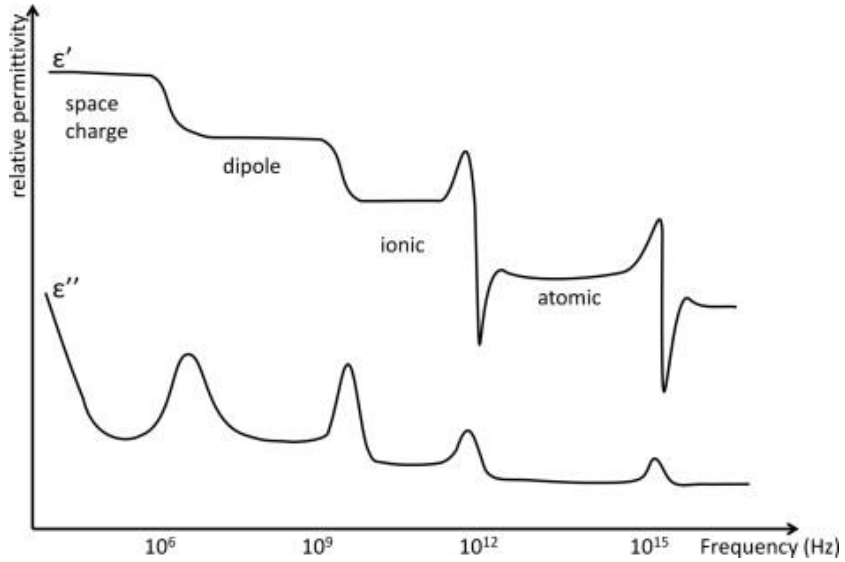

Fig. 2.5 Schematic diagram of the contribution of typical different polarisation mechanisms in a dielectric material to permittivity over the frequency spectrum. [23]

The polarisation mechanisms depicted in Fig. 2.4 act on different scales which influence their response to AC field. A schematic of how the polarisation mechanisms in electroceramics contribute to complex permittivity and how they relax out or resonate at different frequency ranges is shown in Fig. 2.5. In high permittivity materials, all mechanisms may contribute depending on frequency and thus strategies at different scales are implemented to tune their dielectric response.

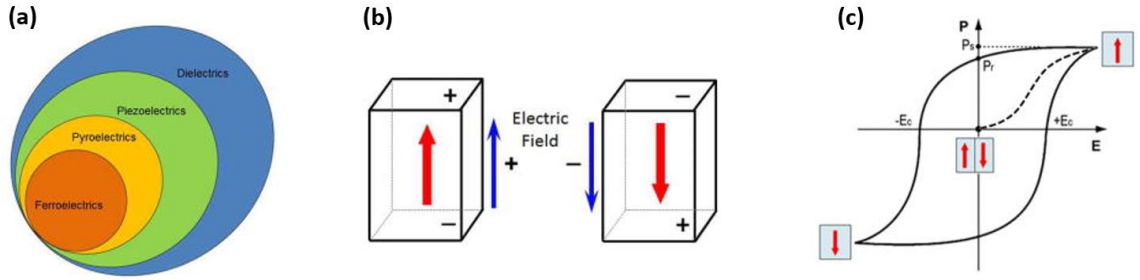

Fig. 2.6 (a) The relationships between dielectric, piezoelectric, pyroelectric, and ferroelectric materials; (b) polar state of ferroelectrics which could be switched by electric field; (c) the Polarisation-Electric field (P-E) hysteresis loop of ferroelectric material.

When a material shows a dielectric response, it sometimes exhibits other related functional properties. The relationships between some of these responses are shown in Fig. 2.6 (a). Piezoelectricity is the characteristic of a material to show polarisation along certain crystallographic directions upon applied mechanical stress. When an electric field is applied to a piezoelectric material, it induces a polarisation in the material, causing the atoms or molecules within the material to shift position. This shift in position leads to a change in the material's dimensions, resulting in mechanical strain. Conversely, when a mechanical stress is applied to a piezoelectric material, it generates an electric field due to the displacement of charges within the material. Pyroelectric materials develop polarisation through uniform changes in temperature. Ferroelectricity is the characteristic of a material to show a spontaneous polarisation which is reversible by external electric field (Fig. 2.6 (b)). The electric field dependant behaviour is usually characterised by the Polarisation-Electric field (P-E) hysteresis loop (Fig. 2.6 (c)). The saturation polarisation or maximum polarisation (P_{max}), remnant polarisation (P_r) and coercive field (E_c) define the shape of the hysteresis loop. There are also some cases where dielectric polarisation couples with magnetic and optical properties to show interesting effects. [24-27]

In non-linear dielectrics, the integral form of equation (2.2) should be used to denote the relationship between P and ε:

$$P = \int_0^E \varepsilon dE \tag{2.3}$$

where ε is the permittivity at each field strength of the integration.

From the P-E hysteresis loop, the electrical energy per unit volume released into the circuit during withdrawal of the electric field (W_{rec}) and its ratio with the energy charged into the material (η) are:

$$W_{rec} = \int_{P_r}^{P_{max}} E \, dP \tag{2.4}$$

$$\eta = \frac{W_{rec}}{W_{total}} * 100\% \tag{2.5}$$

where W_{total} is the total energy density. These parameters are attracting growing research interest since they reflect the energy storage performance of dielectrics, and their optimization is critical to create high energy density and by default high voltage/field capacitors with large volumetric efficiency.

In ferroelectric materials, domains and domain boundaries are important structural characteristics. A domain is a region of spontaneously polarised unit cells with the same direction of polarisation for ferroelectrics (Fig. 2.7 (c)(e)). In ferroelectrics, there are two main types of domain boundaries: twin or orientation boundaries in which the direction of polarisation changes across the boundary through a non-180° angle and inversion boundaries in which the direction of polarisation rotates through 180°. The former only occur if the spontaneous polarisation is coupled to the appearance of spontaneous strain at the paraelectric to ferroelectric phase transition. The appearance of non-180° domains occurs as result of clamping in a polycrystalline ceramic and inhibits anisotropic distortion of the grains. In contrast, 180° domains form because of the depolarising field which opposes the formation of polar order (electric field) over large distances.

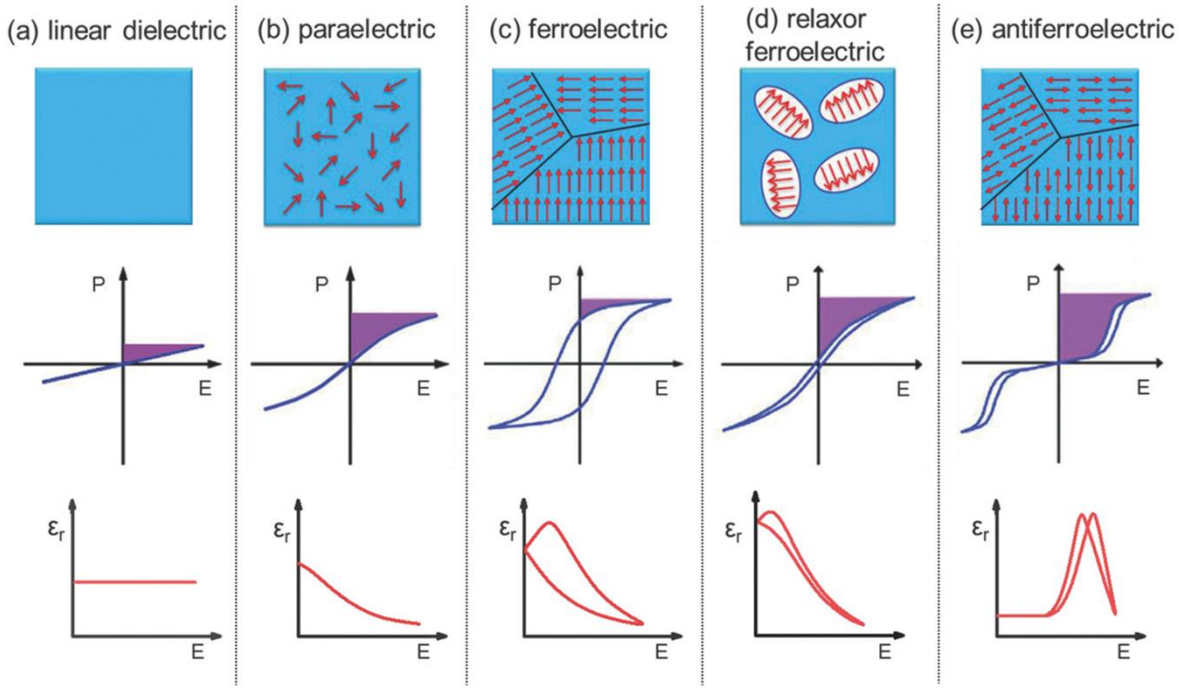

Fig. 2.7 Dipole and domain structures (top panel), P-E loop (middle panel) and permittivity-field dependence (bottom panel) for (a) linear dielectric, (b) paraelectric, (c) ferroelectric, (d)

relaxor ferroelectric, and (e) antiferroelectrics materials. The purple shaded area in P-E loop is the recoverable energy density. The area within the P-E loop is the energy loss.[28]

There are five main types of dielectric material with distinctive dipole/domain structure, P-E loops and field dependant dielectric response (Fig. 2.7). Linear dielectrics have no spontaneous polarisation but exhibit a linear P-E loop and a constant ε with electric field. Paraelectrics have no permanent dipole/polarisation with no electric field but exhibit a non-linear P-E loop and a decrease in ε with electric field. Ferroelectrics have spontaneous polarisation and domain structure with a hysteresis loop that exhibits a characteristic non-linear ε-E response. The peak in the ε-E response is associated with domain switching. Antiferroelectrics have anti-parallel dipoles in neighbouring fundamental unit cells, which provide an overall net zero polarisation. Upon applying sufficient electric field, antiferroelectrics undergo a transition to a ferroelectric state. The peak in ε-E plot is associated with the field induced phase transition. Relaxors are a unique type of dielectric with no microdomains, but instead have polar nanoregions, which are typically easier to switch than ferroelectric microdomains.

Based on equation (2.4), approaches to achieve a high W_{rec} include: i) enhancing the dielectric breakdown strength (BDS) by optimizing the microstructure (eliminating pores, and controlling grain growth) [29], establishing a homogeneous electrical microstructure [1, 30, 31] through control of defect chemistry and choosing materials with a large intrinsic band gap such as $NaNbO_3$; [32] ii) increasing polarisability per unit cell volume by incorporating d_0 (Ti^{4+} and Nb^{5+}) and electron lone-pair ions (Bi^{3+} and Pb^{2+}) on the B- and A-sites, respectively [33, 34] and iii) enhancing P_{max}-P_r by inducing relaxor behaviour through alloying or doping to make pseudo- ternary and quaternary solid solutions. [35] Based on equation (2.5), a higher η is achieved by either inducing relaxor behaviour (narrower P-E hysteresis loop) or reducing the field difference between antiferroelectric and ferroelectric states in antiferroelectric compositions. [36, 37]

2.3 $BaTiO_3$ Based Dielectrics for Consumer Electronics

2.3.1 Composition of $BaTiO_3$ MLCCs

$BaTiO_3$ is currently the most widely used material in class II MLCCs. To achieve high capacitance with small case size, hundreds of dielectric layers with less than 1 µm thickness are stacked alternatively with an inner electrode. In these capacitors, 100-200 nm $BaTiO_3$ particles are used with dopants to tune the dielectric properties. For X7R (-55 to +125 ^oC and +/-15% ΔC) MLCCs, a core-shell microstructure creates the required temperature stability with the core region of a grain remaining ferroelectric tetragonal $BaTiO_3$, and the shell containing various dopants that give rise to a range of Curie temperatures.[38, 39]

One of the most effective set of dopants in MLCC technology are rare earths which when processed correctly induce the core-shell structure in $BaTiO_3$, tuning the dielectric properties. Some of the most intensively investigated dopants are shown in Table 2.1. Rare earth ions with intermediate radius, such as Dy^{3+}, Ho^{3+}, Y^{3+} and Er^{3+} are able to occupy both

A and B site in the $BaTiO_3$ lattice, resulting in both donor and acceptor behaviour. They are widely used in MLCCs since they provide the best reliability as well as X7R temperature stability. [40-42] They are often used in conjunction with MgO which helps suppress the movement of V_O through the formation of $Mg - V_O$ defect dipoles.[40,43]

Class II dielectrics are classified by the Electronics Industries Alliance (EIA) based on their temperature stability using a 3-digit code specified in the "EIA standard RS-198," as presented in Table 2.2. The first two characters of the EIA code indicate the lower and upper temperature limits for operation, respectively, while the third character represents the maximum allowable change in capacitance within the designated temperature range.

In addition to the widely utilized X7R MLCC, there are other composition types incorporating $BaTiO_3$ content to address varying application requirements. In cases where lower temperature stability of permittivity suffices, $BaTiO_3$ is also combined with $BaZrO_3$ and $CaZrO_3$ to form dielectrics exhibiting Z5U and Y5V characteristics, respectively. For applications with greater demands for temperature stability but lower capacitance, $BaTiO_3$ is employed in conjunction with TiO_2, $CaTiO_3$, and $Nd_2Ti_2O_7$ to achieve the desired performance. A comprehensive overview of these compositions is provided in Table 2.3.

Table 2.1 Ionic radii of some common rare earth dopant ions. Radii of Eu, Gd, Dy, Ho, Y, Er, Yb and Lu ions in 12 fold coordination are extrapolated from Shannon and Prewitt. [44]

Coordination number / Dopant ion	6	12
large ionic radius		
La^{3+}	1.032	1.360
Ce^{3+}	1.010	1.340
Nd^{3+}	0.983	1.270
Intermediate ionic radius		
Sm^{3+}	0.958	1.240
Eu^{3+}	0.947	1.266
Gd^{3+}	0.938	1.253
Dy^{3+}	0.912	1.229
Ho^{3+}	0.901	1.218
Y^{3+}	0.900	1.251
Er^{3+}	0.890	1.208
Small ionic radius		
Yb^{3+}	0.868	1.188
Lu^{3+}	0.861	1.178

Table 2.2 EIA code for Class II dielectrics. [45]

Symbol	Low temperature Limit (℃)	Symbol	High Temperature Limit (℃)	Symbol	Maximum Capacitance Change (%)
Z	+10	4	+65	A	± 1.0
Y	-30	5	+85	B	± 1.5
X	-55	6	+105	C	± 2.2
		7	+125	D	±3.3
		8	+150	E	±4.7
				F	±7.5
				P	±10.0
				R	±15.0
				S	±22.0
				T	+22/-33
				U	+22/-56
				V	+22/-82

Table 2.3 Typical ceramic dielectric materials for MLCC with different EIA specifications. [46]

EIA designation	Class	Temp. range (℃)	Temp.-cap. Change (%)	ε_r up to	BT content (%)	Other dopants	Grain Size (μm)
NP0(C0G)	1	-55 to 125	± 30 ppm	100	10-50	TiO_2, $CaTiO_3$, $Nd_2Ti_2O_7$	1
X7R(BX)	2	-55 to 125	± 15	4000	90-98	MgO, MnO, Nb_2O_5, CoO, Rear-earth	<1.5
Z5U	2	10 to 85	+22/-56	14000	80-90	$CaZrO_3$, $BaZrO_3$	3-10
Y5V	2	-30 to 85	+22/-82	18000	80-90	$CaZrO_3$, $BaZrO_3$	3-10

2.3.2 Fabrication of MLCCs

MLCC fabrication involves a complex process integrating tape-casting, screen printing, and co-firing of ceramic dielectrics with a metal internal electrode. A schematic of the process is shown in Fig. 2.8 which illustrates the following generic steps. First, the ceramic powder is mixed with solvent, binder, plasticisers and dispersant to form a homogeneous suspension. Then the slurry is cast into a thin sheet on a plastic film using a doctor blade. After the sheet is dried to form a flexible tape, an electrode ink is applied to the tape using screen printer to achieve desired pattern and thickness. The sheets are stacked layer by layer and laminated. After cutting/dicing, the green devices undergo binder burnout and sintering process. Finally, terminal electrodes are applied to the devices to allow electrical characterisation.

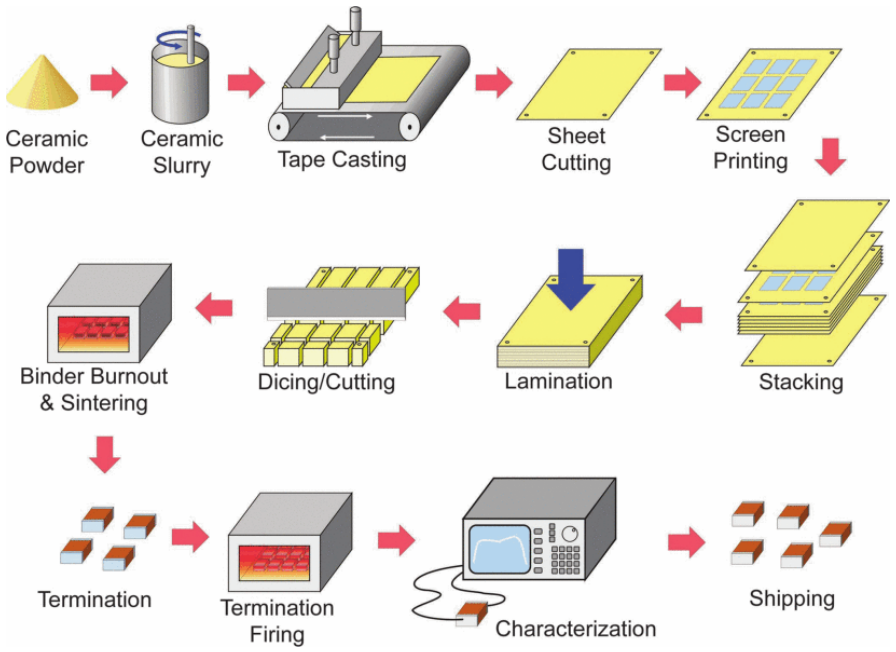

Fig. 2.8 Schematic diagram of the MLCC fabrication process. [45]

The manipulation of material properties via crystal chemistry is combined with engineering the dielectric layer thickness and co-firing with base metal electrode (BME), to achieve the desired MLCC properties at a reasonable cost. [46] The development of MLCCs is an exceptional example of how powder-based slurry technology may be used to mass produce essential components in electronics. A US company invented MLCC during the Apollo programme in 1961 to meet the demand for compact, high volumetric efficiency capacitors. [47] But the wide spread use of MLCC did not happen until the increase in production of cell phones and computers in the 1990s. [46] The capacitance of MLCCs of the same case size has been improved greatly in the past few decades by decreasing the dielectric layer thickness which is a result of improved manufacturing procedures. Since the mid-1990s, progress in development of non-reducible dielectrics coupled with novel sintering methods and the use of base metal internal electrodes, such as Ni and Cu, have decreased the cost of the component greatly.[48]

2.4 High Energy Density Capacitors

In the following section, the criteria for evaluating the energy storage performance of dielectrics are discussed along with the dielectric/energy storage characteristics of different materials depending on their polar/domain structure.

2.4.1 Lead Based

Lead-based ceramics are commercialized in piezoelectric devices and capacitors for their exceptional properties that arise in part from the high polarizability of Pb^{2+}. [49, 50] A range of lead-based materials from relaxor ferroelectrics to AFEs have been investigated for energy storage performance. Lead-based relaxors that have been investigated include $Pb(Mg_{1/3}Nb_{2/3})O_3$–$PbTiO_3$ (PMN–PT), PMN–$Pb(Sn,Ti)O_3$ (PMN–PST), $Pb(Zn_{1/3}Nb_{2/3})O_3$–$PbTiO_3$

(PZN–PT), $Pb(In_{1/2}Nb_{1/2})O_3$-$Pb(Mg_{1/3}Nb_{2/3})O_3$-$PbTiO_3$ (PIN-PMN-PT) and (Sr,Pb,Bi)-TiO_3 (SPBT) [51-56] Excellent thermal stability and W_{rec} = 0.85 J/cm^3 was reported in PMN-PST relaxor ceramic, due to the coexistence of ferroelectric domains and PNRs as observed by piezoelectric force microscopy. [57]

Besides relaxors, $PbZrO_3$ (PZ) based materials have also been investigated. PZ is the first known AFE and exhibits a reversible transition to a FE phase under applied field. [58] The AFE-FE phase transition field along with other properties is tuned through the use of dopants such as, Sn, Ti, Ca, Nb and RE-ions. Compositions include: (Pb, La) (Zr, Ti)O_3 (PLZT); [59-61] (Pb, La) (Zr, Sn, Ti)O_3 (PLZST); [62-64] and (Pb, La) (Zr, Sn)O_3 (PLZS). [65, 66] Other Pb-based AFE materials include $PbHfO_3$, $PbIn_{1/2}Nb_{1/2}O_3$, $PbYb_{1/2}Nb_{1/2}O_3$, $PbLu_{1/2}Ta_{1/2}O_3$, $Pb(Tm_{1/2}Nb_{1/2})O_3$, $Pb(Lu_{1/2}Nb_{1/2})O_3$. [67-70] with some investigated for their energy storage properties, usually either in solid solution or doped to enhance performance. [71-73]

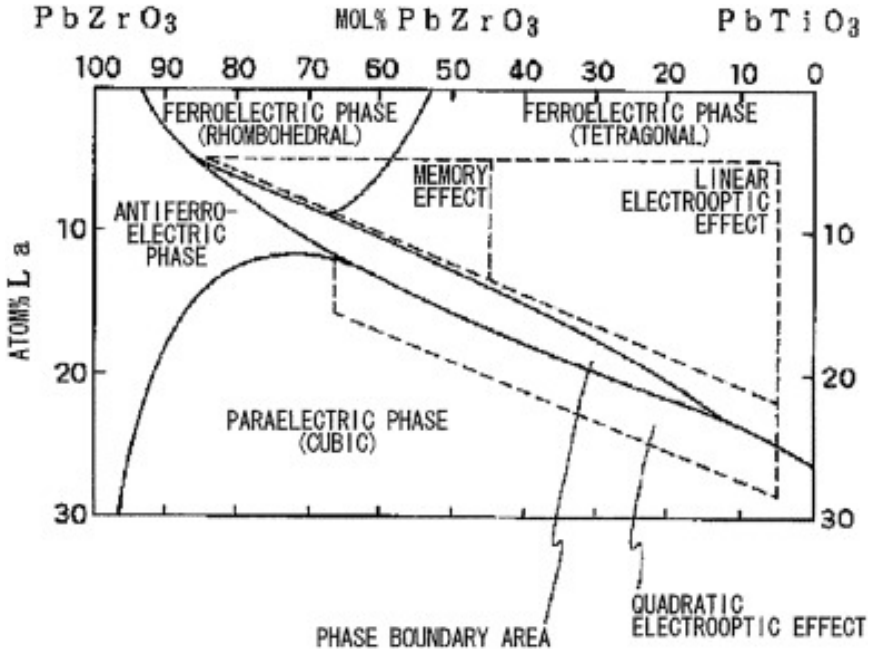

Fig. 2.9 Phase diagram of PLZT solid solution with 0 - 30% La content. [74]

The phase diagram of PLZT is shown in Fig. 2.9. The y axis represents the percentage of La with respect to Zr:Ti ratio (x axis). Formulations of PLZT assume an ionic compensation model through V''_{Pb} to maintain electroneutrality. [75, 76 77, 78] Generally speaking, the large W_{rec} provided by the AFE phase occurs in Zr-rich compositions. For compositions with lower Zr concentration, there is a slim relaxor region in the phase diagram PLZT but this has not been significantly explored for energy storage.

The incorporation of La^{3+} ions in the A site of the crystal lattice is expected to stabilise the AFE phase, due to a reduction in tolerance factor (t) caused by the smaller La^{3+} with respect to Pb^{2+} ion. [33] Further modification of PLZT, such as doping with Mn^{2+} ions in the B site of PLZT to enlarge the denominator in t, improves the stability of AFE phase and thus, the energy storage performance. [75]

PLZST is one of the best-known examples of this family of materials, with the B site ions partly replaced by Sn^{4+}. Similar to PLZT, PLZST is mostly investigated in films due to its large AFE-FE transition field and high BDS. For compositions with 5 % - 45 % of Sn^{4+} on the B-site, forward switching field (E_{A-F}) and backward switching field (E_{F-A}) increase as Sn concentration decreases accompanied by an increase in maximum polarisation, yielding a large W_{rec} of 5.6 J/cm^3 and η of 67 % at room temperature [63] but the AFE and FE phase distribution and switching require further investigation. [79, 80]

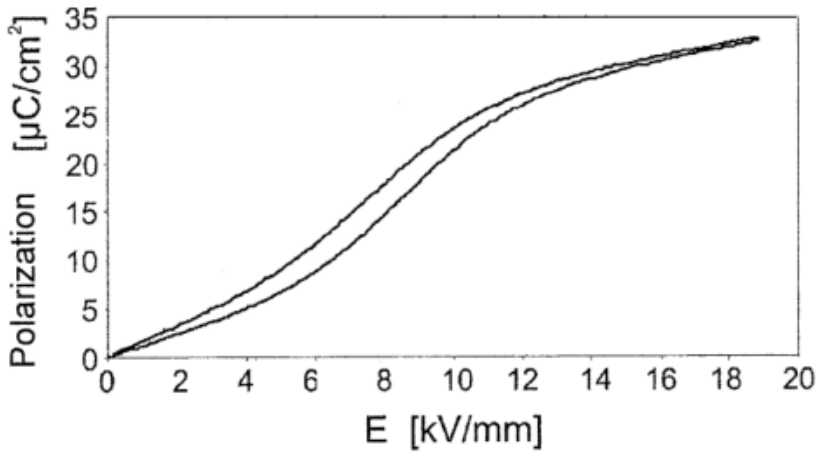

Fig. 2.10 The P-E loop of a MLCC with $(Pb_{0.87}La_{0.07}Na_{0.05})(Zr_{0.86}Ti_{0.14})O_3$ as dielectric and Cu inner electrode. [81]

PLZT based high field MLCCs were developed by Ceralink™ in 2010, [82, 83] and target the power electronics market. Na^+/K^+ ions are substituted on the A site to increase the switching field of the composition and decrease the firing temperature. A small amount of other dopants such as Mn^{2+}, Fe^{3+}, and rare earth elements are used to tune the donor-acceptor ratio and improve the reliability of the MLCC. [81] Copper inner electrodes are co-fired with the composition under controlled atmosphere, with replacing the La^{3+} with e.g. Ba^{2+}, Sr^{2+}, and Ca^{2+} ions prioritised to reduce the cost of the material. [84] The P-E loop of a ceralink MLCC is shown in Fig. 2.10.

2.4.2 Lead Free

Due to the toxicity of lead-based compounds, extensive research has recently focused on lead-free ceramics to replace PLZT in relevant applications. Research has mainly focussed ceramics based on BT, $K_{0.5}Na_{0.5}NbO_3$ (KNN), $BiFeO_3$ (BF), $Na_{0.5}Bi_{0.5}TiO_3$ (NBT), $SrTiO_3$ (ST), $NaNbO_3$ (NN) and $AgNbO_3$ (AN) which are introduced in the following sections.

BT is the mainstay of the MLCC industry however, base metal X7R and Z5U capacitors used in consumer electronics have a comparatively low BDS (< 150 kV/cm) and an operating temperature < 125 ^oC. [45, 85] Attempts to improve BT based materials have focussed on various strategies including: (i) introducing insulating oxides, such as Al_2O_3, SiO_2, La_2O_3, MgO, to enhance the BDS of the material; [86-89] (ii) utilising novel processing techniques, such as

spark plasma sintering (SPS), cold sintering, constrained sintering, and citrate precursor to produce dense ceramic, improve the temperature stability or reduce the sintering temperature; [38, 90-92] (iii) employing sintering aids, such as $CuBi_2O_4$, $ZnNb_2O_6$ and $NiNb_2O_6$ to decrease the sintering temperature and increase ceramic density [93-95] and (iv) incorporating more end members, such as $Bi(Mg_{2/3}Nb_{1/3})O_3$, [96] $Bi(Zn_{2/3}Nb_{1/3})O_3$, [97] $BiYbO_3$, [98] $Bi_{0.5}Na_{0.5}TiO_3$, [99] $Bi(Zn_{1/2}Ti_{1/2})O_3$, [100] $Bi(Mg_{1/2}Ti_{1/2})O_3$, [101] $Bi(Mg_{1/2}Zr_{1/2})O_3$, [102] $Nd(Zn_{1/2}Ti_{1/2})O_3$, [103] $K_{0.5}Bi_{0.5}O_3$, [104] to form solid solutions with enhanced relaxor characteristics, thus achieving higher W_{rec} and η. For example, good temperature stability and energy density from room temperature to 350 °C were demonstrated in a 1 µF MLCC made of $BaTiO_3$ - $Bi(Zn_{1/2}Ti_{1/2})O_3$ with Ag - Pd electrodes. [100] In BT based ceramics, the most effective method of improving energy storage is through the substitution of $Bi(B'_{1/2}B''_{1/2})O_3$ into the crystal lattice, where B' and B'' denotes two different ionic species. The large polarizability of Bi^{3+} in the A site arising from the lone pair $6s^2$ electron configuration improves the average polarisation per unit volume of the material but long-range polar coupling is disrupted with the presence of ions with different radius as well as valence on both A and B-sites.

For KNN based ceramics, similar strategies as in BT are used. For example, ST is introduced to form a solid solution with KNN which decreases the grain size, thereby raising the BDS to 400 kV/cm with a commensurately large W_{rec} of 4.03 J/cm^3. [105] KNN - $Bi(Me_{2/3}Nb_{1/3})O_3$ solid solutions generally form relaxor ferroelectrics with unsaturated polarisation at 300 kV/cm and η <90 %. [106] In addition, sintering aids such as CuO and ZnO, have been introduced in KNN based systems to achieve ceramics with lower porosity and reduced sintering temperatures. [107, 108]

BF based material have attracted attention for their potential in high temperature applications, due to their high T_c and large spontaneous polarisation. Volatilization of Bi^{3+} ions during the sintering process of BF leads to variation of Fe valence and a high concentration of oxygen vacancies in the ceramic. The high leakage current associated with oxygen vacancies has to date prohibited the commercialization of BF based material. However, a low loss was achieved in MLCCs made from 0.4BF - 0.6ST for up to 300 °C. The discharge performance of the device was stable up to 200 °C, opening up a new market for energy storage capacitors inbetween class I and class II ceramics. [109] In 2019, electrically homogeneous BF - BT materials were reported by Lu et al by alloying with an end-member and doping with heterovalent cations. A signal arc in IS spectrum confirmed the electrical homogeneity. [1]

Similar to BF, NBT based ceramics also have high polarisation and high T_c in comparison with BT, with volatilisation of Bi^{3+} ions and Na^+ ions also problematic. The perovskite TiO_3^{2-} octahedral sublattice and its multivalent A site ions enable a greater variation of dopants to enter the NBT matrix such as K^+, Li^+, Ba^{2+}, Sr^{2+}, La^{3+}, Nd^{3+}, Dy^{3+}, etc. [110-113] Co-doping of A and B site of the lattice is also common[114-116] with oxides such as ZrO_2, MnO, MgO and Fe_2O_3 sometimes used as dopants to control defect chemistry. [117-120]

ST is an incipient ferroelectric with high permittivity (300) and low loss (0.01) and thus a promising base material for energy storage applications. The flexible crystal matrix allows doping of ions, such as Mg^{2+}, Ba^{2+}, Dy^{3+} and Bi^{3+} on the A site and Sn^{4+} and Mn^{4+} on the B site.

[35] Sintering aids and alternative sintering techniques have been employed to fabricate ceramics with enhanced properties. [121-123] Perovskite end members may be introduced to from solid solutions such as $0.9(Sr_{0.7}Bi_{0.2})TiO_3$ - $0.1Bi(Mg_{0.5}Me_{0.5})O_3$ ceramic which has a BDS of 460 kV/cm with thermal stability of energy storage properties up to 200 °C. [124]

NN is a lead-free AFE material with high saturation polarisation of 30 $\mu C/cm^2$. [125] Due to the small difference in Gibbs free energy of the AFE and FE phases of NN, the double hysteresis loop sometimes does not appear in NN ceramics but doping the A-site with a smaller or the B-site with larger ions, decreases t and helps stabilise the AFE phase.[126] W_{rec} is enhanced by improving the BDS and the polarisation under high electric field with η improved through inducing a relaxor state. Doping with $Bi(B'_{1/2}B''_{1/2})O_3$ is a common strategy used in NN based systems to achieve better energy storage performance. Qi et al. fabricated 0.76NN - 0.24NBT relaxor ceramic with $W_{rec} \approx 12.2$ J/cm^3 and $\eta \approx 69\%$ under 680 kV/cm applied field. [32]

AN has also been considered as a candidate for energy storage applications due to its high saturation polarisation of 45 $\mu C/cm^2$ at comparatively low field (144 kV/cm) combined with a low remnant polarisation of 4 $\mu C/cm^2$. [127] Various strategies have been used to stabilise the AFE phase and reduce the hysteresis area in the field induced FE phase. For example, Sr^{2+}, Ba^{2+}, Ca^{2+}, La^{3+}, Bi^{3+}, Gd^{3+} and Sm^{3+} ions have been doped into the A site and Ta^{5+}, Mn^{4+} and W^{6+} ions into the B site of AN. In combination dopants tend to reduce the grain size, delay the E_{A-F} and increase the η of energy storage. [35, 128-130] End members such as $BiMnO_3$ and $Bi(Zn_{2/3}Nb_{1/3})O_3$ have also been incorporated within AN and achieve similar outcomes. [131, 132]

The energy storage performance of lead-free ceramics has improved markedly over the last few years due to the extensive research being devoted to this area and they now demonstrate superior performance with respect to lead-based counterparts. For example, the highest W_{rec} of 12.2 J/cm^3 in electroceramics was achieved in NN based material at 680 kV/cm[32] with high η of 92% obtained in relaxor NBT-SBT-BMN ceramics (W_{rec} of 7.5 J/cm^3) which is superior to most lead containing materials.[31] For practical applications and to replace the current commercial products, the charge-discharge performance, temperature stability, fatigue behaviour and frequency stability of the lead-free ceramics require further investigation. In emerging application, such as on/near engine electronics and sensors on ultra-deep drills, both the high temperature performance and the mechanical stress resistance is of great importance for ceramic based devices. [133, 134] These engineering problems require extensive efforts before the commercialization of lead free ceramics can be considered. In addition, low cost internal electrode systems are required to reduce costs.

2.5 $BaTiO_3$-$NaNbO_3$ Based Dielectrics

The $BaTiO_3$-$NaNbO_3$ (BT-NN) solid solution was first investigated Roy et al in the 1950s. [135] In 1978, Raevskii et al confirmed that BT and NN could form a complete solid solution, and constructed a phase diagram from visual polythermal, thermographic and dielectric investigations. [136] Although the exact characteristics of the ferroelectric and antiferroelectric

regions in the phase diagram are still under debate, [137-139] there is consensus that relaxor characteristics exist from 2% - 85% NN content, and dopants such as Zr^{4+}, Er^{3+} and Pr^{3+} and end members, such as $Bi(Mg_{1/2}Ti_{1/2})O_3$ tune the electrical properties of the solid solution. [140, 141]

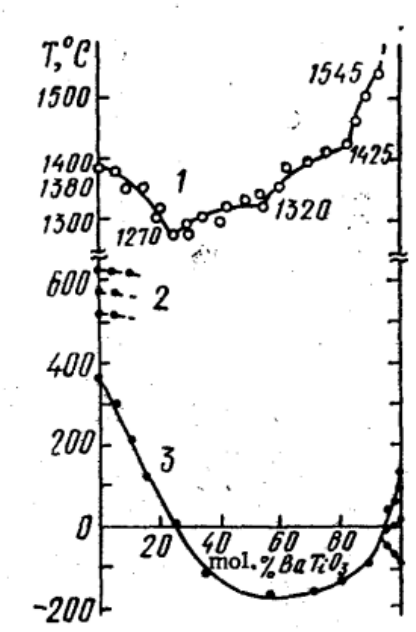

Fig. 2.11 Phase diagram of BT-NN solid solution. [136]

A patent based on the BT rich (⩾70%) end of the solid solution highlights the potential of these compositions in dielectric capacitor applications [142] whereas the NN rich end of the solid solution has mainly been investigated for piezoelectric applications, since NN has a high Curie temperature and high piezoelectric activity. [143, 144] There are several further patents on BT-NN based piezoelectric materials as well as components [145-147] and their electrostrictive behaviour has been investigated by Zuo et al for low hysteresis actuation. [148] BT-NN thin films have also been investigated for potential dielectric, ferroelectric and piezoelectric applications. [149-151]

Only very recently have researchers begun to evaluate BT-NN from an energy storage perspective. In a study by Zhao et al, W_{rec} of 3.07 J/cm^3 was achieved in 0.6BT-0.4NN ceramics with η of 92.6% at 10 Hz. [152]

2.6 Premise of The Research

In this thesis, both the BT rich and NN rich end of the BT-NN solid solution are explored, with doping and alloying with a stoichiometric end member used to optimize the low field dielectric temperature stability and the high field energy storage performance. One of the limitations current class II (X7R) MLCCs is that their permittivity greatly reduces at high field with effective ε_r tuned from ~2000 to only 300 in state of the art MLCCs with dielectric layer thickness <0.5 μm. Thus, unipolar P-E loops in addition to classic low field impedance

measurements are used in this study to characterise the material, since they provide a more accurate representation of the high field performance of a material.

3 Experimental Methods

In this chapter, the experimental techniques used in the project for the fabrication and characterisation of ceramics and multilayers are introduced.

3.1 Fabrication of Ceramics

3.1.1 Particle Size Analysis (PSA)

The structure and electrical properties of ceramics are heavily associated with their grain size. [153] To control the grain size, it is essential to control the particle size of the raw materials. Thus, the particle size of raw material before and after milling, and the particle size of milled calcined powder were measured with using a Mastersizer 3000 (Malvern Instrument Ltd.).

The principle of measurement based on laser diffraction and Mie scattering theory is shown in Fig. 3.1. The Mie scattering theory uses Maxwell's equation that describes the electromagnetic field around a homogeneous sphere during interaction with a plane wave. [154] For particles with diameters over 40 times that of the laser wavelength, the reflection, refraction and absorption of the laser may be omitted, allowing use of the Fraunhofer diffraction equation:

$$\sin\theta_n = \frac{n \cdot \lambda}{x} \tag{3.1}$$

where θ_n is the diffraction angle, n is the ordinal number of the diffraction angle and λ is the wavelength of the laser. From equation 3.1, the larger the particle, the smaller the diffraction angle for diffracted light with the same ordinal number. However, for particles with diameter < 25 μm, the scenario is usually more complex, since the reflection, refraction and absorption need to be considered. [155] Thus, the reflection index and absorption index of the particle should be inputted into the software for a more accurate measurement.

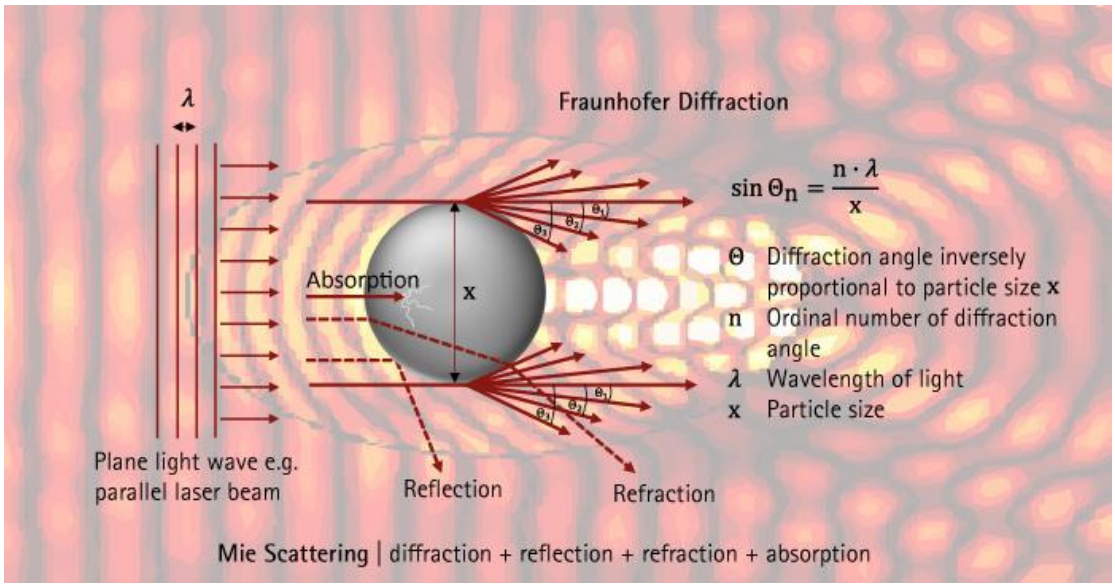

Fig. 3.1 Schematic diagram showing the principle of Mie scattering, with the equation for Fraunhofer diffraction inserted, and the background of the simulated electromagnetic field around the particle. [156]

3.1.2 Density

Density is crucial for the performance of electroceramics. A higher relative density means there are less pores in the ceramic, and therefore less interface between the ceramic substance and air in the sample, giving less place for space charge to accumulate, increasing their reliability and reproducibility.

The densities of ceramic samples were determined using a digital densitometer (Mettler Toledo, MS104S) using the Archimedes' Principle which states that the buoyancy of an object in liquid equals to the weight of liquid with the volume of the object. Thus, the density of an object (ρ) may be calculated by comparing the apparent weight of the object in air and in liquid using the equation:

$$\rho = \frac{A}{A-B}(\rho_0 + \rho_L) + \rho_L \tag{3.2}$$

where A and B are the weight of sample in air and in liquid, ρ_0 and ρ_L are the density of air and liquid, respectively.

The theoretical density (ρ_{the}) is deduced from the XRD data, assuming the chemical composition of the material is exactly the same as the nominal composition, using the equation:

$$\rho_{the} = \frac{n \cdot M}{N_A \cdot V_{cell}} \tag{3.3}$$

where M is the molecular weight of the material, n is the number of formula unit per unit cell, N_A is the Avogadro constant (6.023×10^{23} mol^{-1}), and V_{cell} is the volume of the unit cell extracted by Rietveld refinement of the XRD data.

The relative density of the sample (ρ_{rel}) is calculated with:

$$\rho_{rel} = \frac{\rho}{\rho_{the}} \times 100\% \tag{3.4}$$

where ρ is the density and ρ_{the} is the theoretical density of the sample.

3.2 Structural and Microstructural Characterisation

3.2.1 X-Ray Diffraction (XRD)

XRD is used to determine the crystalline phase of the fabricated materials and was performed on a Bruker D2 phaser diffractometer equipped with Cu Kα radiation (λ = 1.5418 Å) source operating at 40 kV and 30 mA. K_β radiation was filtered using a Ni plate. Data was

collected between 20° and 60°, with a step size of 0.02°. The interference of diffracted radiation at an angle (θ) satisfies Bragg's law:

$$n\lambda = 2d\sin\theta \tag{3.5}$$

where n is the order of diffraction, λ is the wavelength of the incident wave, and d is the spacing between crystal planes. A reflection is considered indexed when its Miller indices, or more accurately, its components of reciprocal lattice vectors, are determined based on the known wavelength and the scattering angle 2θ. This indexing process provides information about the unit-cell parameters, including the lengths and angles of the unit-cell, as well as its space group. While Bragg's law is insufficient for interpreting the relative intensities of reflections, it does not provide a solution for determining the arrangement of atoms within the unit-cell. To address this aspect, a Fourier transform method must be employed.

Phase analysis was performed by comparing the diffraction pattern with the data in ICDD PDF4+ database. To further analyse the crystal structure, full-pattern Rietveld refinement was performed using TOPAS 5 software. [157] The 'fundamental parameter' approach was adopted, in which the peak shape is calculated from the instrument parameters [158] and specimen characteristics, space group, and initial structural data are optimised. The fitting was converged using a least squares method.

3.2.2 Raman Spectroscopy

Raman spectroscopy is commonly employed for the examination of the vibrational modes associated with molecules or chemical bonds. The vibrational modes of a molecule depend on various factors, including the arrangement of its atoms and bonds, the atomic mass of the atoms, bond order, and hydrogen bonding. Each vibrational mode corresponds to a specific frequency, typically falling within the infrared region of the electromagnetic spectrum. Similar to atomic energy levels, these modes exhibit quantization. The occurrence of Raman spectroscopy is linked to molecular vibrations inducing a "change in polarizability" of the molecule. This technique proves particularly valuable for investigating the overall state of chemical bonding within an approximate area of ~μm2 on a sample's surface. Raman spectra can effectively distinguish between different phases, even in cases where subtle structural differences are present. [159]

The measurement was performed on a Renishaw inVia Confocal Raman Microscope (Renishaw), with a green Ar laser (λ = 514.5nm). The data was recorded by "WiRE 3.4" software, with Raman shift in the range of 100-1000 cm^{-1}. Number of accumulations and exposure time vary from 1-10 and 10-20s, respectively, based on the specimen.

3.2.3 Scanning Electron Microscopy (SEM)

SEM is performed using the interaction between an accelerated electron beam and the atoms on the sample surface. Secondary (SE) and backscatter electrons (BSE) emitted from

the surface are used for imaging and the characteristic X-rays are used to undertake energy dispersive X-ray (EDX) analysis for semi-quantitative determination of the percentage and distribution of elements on the sample surface. SEM was performed on an Inspect F50 scanning electron microscope (FEI) using an accelerating voltage of 20 kV, spot size of 3.5 and a working distance of 10-12 mm.

Before imaging, samples were polished with abrasive papers, then with 3 and 1 µm diamond paste on a synthetic polishing cloth. The polished samples were heat treated at 90% of the sintering temperature for 20 minutes to expose the grain boundary. The samples were then mounted on the aluminium stub using Ag-dag and sputtered with carbon to increase the surface conductivity prevent charging.

3.3 Electrical Characterisation

3.3.1 Permittivity vs. Temperature (LCR) Measurements

When the capacitance (C) of a sample with circular electrodes of same diameter on two opposite surfaces are measured, ε of the sample may be calculated with:

$$\varepsilon = \frac{4Ct}{\pi\varepsilon_0 d^2} \tag{3.6}$$

where t is the sample thickness, ε_0 is the permittivity of free space (8.854×10^{-12} F/m), and d is the diameter of the electrode.

The dielectric loss tangent is the ratio between the imaginary part and real part of permittivity:

$$\tan\delta = \frac{\varepsilon''}{\varepsilon'} \tag{3.7}$$

For measurement of C in a ceramic sample with the electrode configuration described above, the auto-balancing bridge method is typically used, since it provides the widest impedance measurement range in the frequency range of 20 - 100MHz. [160] A schematic of this method is shown in Fig. 3.2, where an I-V converter is used to balance the current I_x flowing through the Device Under Test (DUT) and the current I_r flowing through a range resistor R_r. The voltage at the Low point is kept at 0 V. Thus, the Low point is called the virtual ground. The impedance of the DUT may then be calculated with the equations in Fig. 3.2. In practice, the configuration of the circuit differs with different instrument, but the principle shown here is universal.

Samples are coated with gold paste (T-10112, Metalor Technologies UK Ltd.) and fired at 800 ℃ for 2 hours to adhere the electrode to the sample. An Agilent E4980A LCR meter (Agilent Technology) is used with measurements taken at 1kHz, 10kHz, 100kHz, 250kHz, and 1MHz at each temperature, with rate of heating/cooling at 1 $℃/\mathrm{min}$. A non-inductively wound tube furnace (TSH10/38/130, Elite Thermal Systems Ltd.) is used for high

temperature and a closed-cycle He refrigerator (Optistat, Oxford Instrument Ltd.) for low temperature runs.

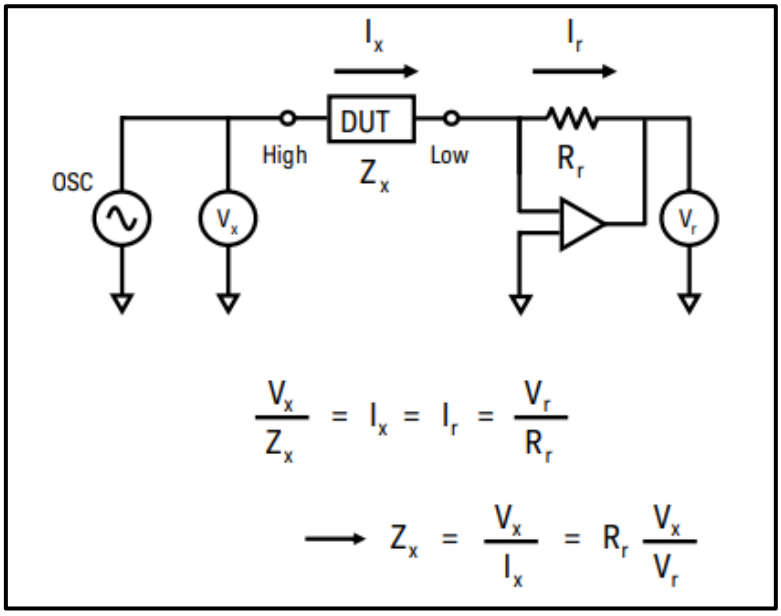

Fig. 3.2 Auto-balancing bridge method for impedance/LCR measurement. [161]

3.3.2 Impedance Spectroscopy (IS)

3.3.2.1 Principle and Set Up

In Fig. 3.3, the instrument, the testing fixture, testing channel and Device Under Test (DUT) are shown to illustrate the key points of an impedance measurement: the H_c terminal supplies the test signal and the H_p and L_p terminals detect the Hi and Lo potential of the DUT. In the L_c terminal, the current flowing through the DUT is detected and converted to a voltage to ensure (1) the current flowing through R_r balance with the current flowing through the DUT and (2) the potential of L_c terminal is kept at 0 V.

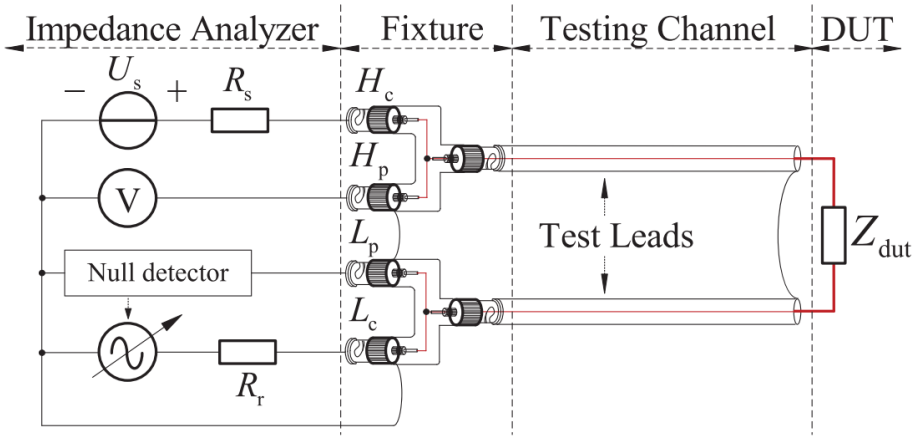

Fig. 3.3 Schematic diagram of the impedance measurement showing the wiring between the impedance analyser and the DUT. [162]

The testing fixture and leads are surrounded by grounded shells to protect against the interference from electromagnetic fields. To eliminate the influence of the testing fixture, channel and jig on the impedance data, a close circuit and open circuit correction was performed. This correction is crucial for obtaining an accurate interpretation of the sample.

The samples are prepared in the same way as in LCR measurement. A Solartron SI 1260 impedance analyser (Solartron Group Ltd.) was used to obtain impedance measurements from 1 Hz - 1 MHz. The applied voltage was 100 mV for all samples. A geometric factor (A/t, where A is the electrode area, and t is the sample thickness) was used to normalise the result for sample geometry. Different oxygen partial pressure was applied by using atmosphere gases, including N_2, O_2 and air. Zview software (Scribner Associates Inc.).

As illustrated in section 3.3.1., the data are collected in the form of voltage outputs. The complex impedance (Z*), complex admittance (Y* or A*), complex modulus (M*) and complex capacitance/permittivity (C* or ε*) are the four most useful parameters to analyse a sample for simple electrode configurations (i.e with low inductance). The equations for the calculation and conversion of these parameters as follow:

(1) For Z*:

$$Z^* = Z' - \vec{j}Z'' = R - \vec{j}X \tag{3.8}$$

where Z' is the real part of impedance, Z" is the imaginary part of impedance, R (= Z') is the resistance, X (= Z") is the reactance, and $\vec{j} = \sqrt{-1}$.

(2) For Y*:

$$Y^* = Y' + \vec{j}Y'' = G + \vec{j}B \tag{3.9}$$

where Y' is the real part of admittance, Y" is the imaginary part of admittance, G (= Y') is the conductance, B (= Y") is the susceptance. Y* and Z* are associated by:

$$Y^* = \frac{1}{Z^*} = \frac{1}{Z' - \vec{j}Z''} = \frac{Z'}{(Z')^2 + (Z'')^2} + \vec{j}\frac{Z''}{(Z')^2 + (Z'')^2} \tag{3.10}$$

(3) For M*:

$$M^* = M' + \vec{j}M'' \tag{3.11}$$

where M' is the real part of electric modulus, and M" is the imaginary part of electric modulus. M* is associated to Z* by:

$$M^* = \vec{j}\omega C_0 Z^* = \omega C_0 Z'' + \vec{j}\omega C_0 Z' \tag{3.12}$$

where ω is the angular frequency of the test and C_0 is the vacuum capacitance of the measuring cell:

$$\omega = 2\pi f \tag{3.13}$$

$$C_0 = \varepsilon_0 \frac{A}{d} \tag{3.14}$$

in which f is the testing frequency, ε_0 is the permittivity of free space (8.854×10^{-12} F/m), A is the cell electrode area and d is the cell thickness.

(4) For C*:

$$C^* = C' - \vec{j}C'' \tag{3.15}$$

where C' is the real part of capacitance, and C" is the imaginary part of capacitance. The relationship between C*, M* and Z* are:

$$C^* = \frac{1}{M^*} = \frac{1}{\vec{j}\omega C_0 Z^*} = \frac{1}{\omega C_0}\left(\frac{Z''}{(Z')^2 + (Z'')^2} - \vec{j}\frac{Z'}{(Z')^2 + (Z'')^2}\right) \tag{3.16}$$

From one set of data, it is simple to derive the other three sets using the above equations. A combined pair of formalisms should be used for analysis of impedance response, due to the frequency dependence of these parameters. For example, (Z*, M*) are usually used for parallel circuit analysis, and (Y*, C*) for series circuit analysis.

3.3.2.2 Parallel and Series R-C Component

The principles of using pairs of formalisms are illustrated in Fig. 3.4 and Fig. 3.5 by analysing the parallel and series R-C component.

For a parallel R-C circuit, the Z* plots and M* plots shown in Fig. 3.4(a) and (b) are both arcs, with the same peak condition of ωRC = 1. It should be noted that Z' decrease, while M' increase with increasing frequency. Thus, both Z* and M* should be considered when analysing the response of a parallel R-C element. The Y* plots and C* plots are just a straight line with little direct information for interpretation, so are usually not used for such circuits.

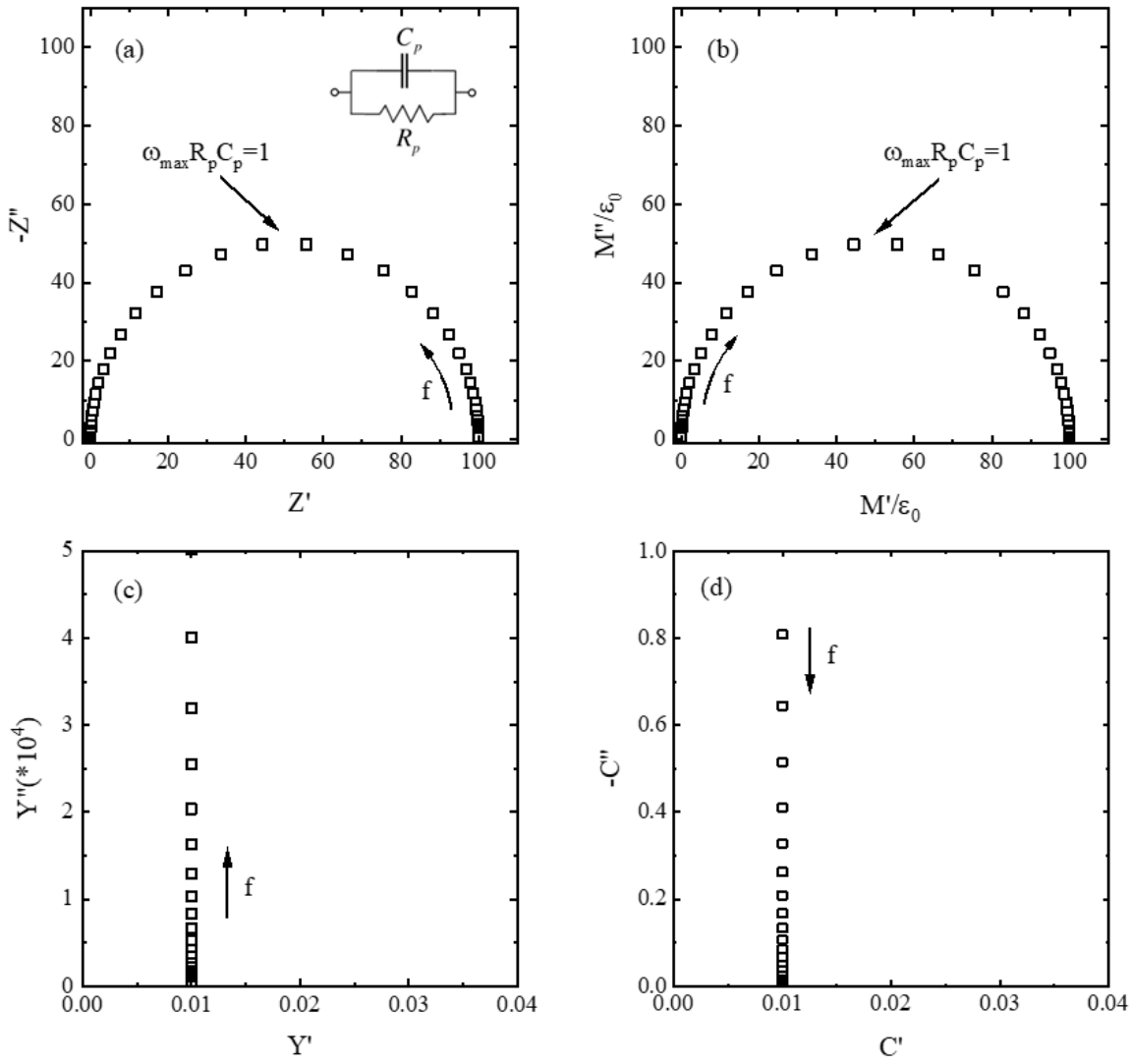

Fig. 3.4 Simulated (a) Z*, (b) M* plots with the peak condition indicated; (c) Y*, (d) C* plots of a parallel R-C circuit with a resistor of 100 Ω and a capacitor of 10 mF.

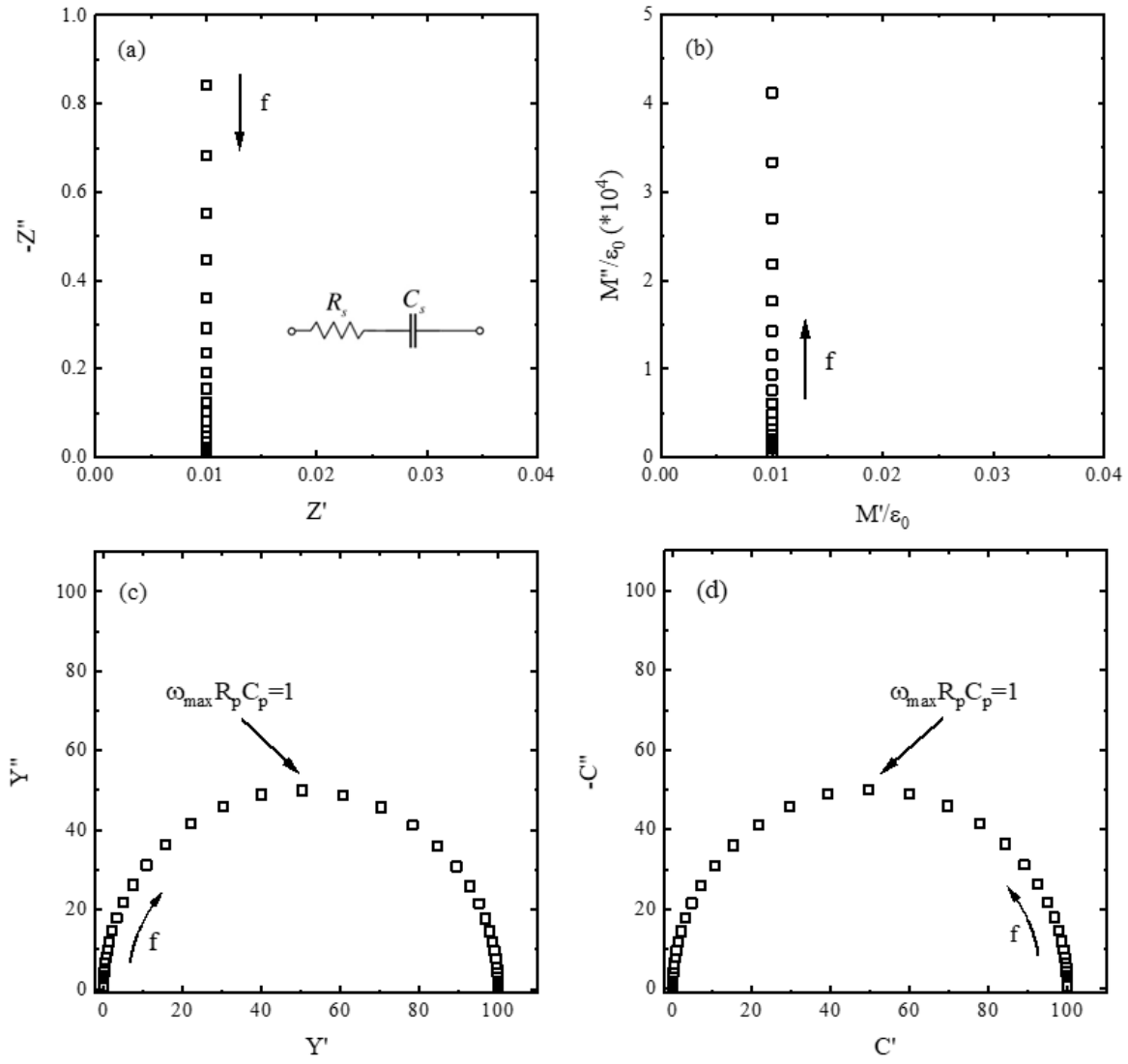

Fig. 3.5 Simulated (a) Z*, (b) M*, (c) Y*, (d) C* plots of a parallel R-C circuit with a resistor of 10 mΩ and a capacitor of 100 F.

For a series R-C circuit, the situation is reversed. As shown in Fig. 3.5, the Z* plots and M* plots are a straight line, and the Y* plots and C* plots are arcs with peak condition of ωRC = 1. Thus, Y* and C* are usually analysed for such circuits.

The impedance response of most materials consists of one or more parallel R-C elements. For ceramics, the response of core and shell of grains, grains, grain boundaries, and sometimes electrode-ceramic interfaces are detected as separate R-C elements. An ideal case is given in Fig. 3.6, where each of the responses could be fitted with a parallel R-C element. However, in practice the response of the sample couldn't be accurately represented by a few simple R-C elements. Thus, additional elements such as constant phase element (CPE) and Warburg-type resistance element (W) are introduced to simulate non-ideal Debye relaxation and the diffusion phenomena at the sample/electrode interface, respectively.

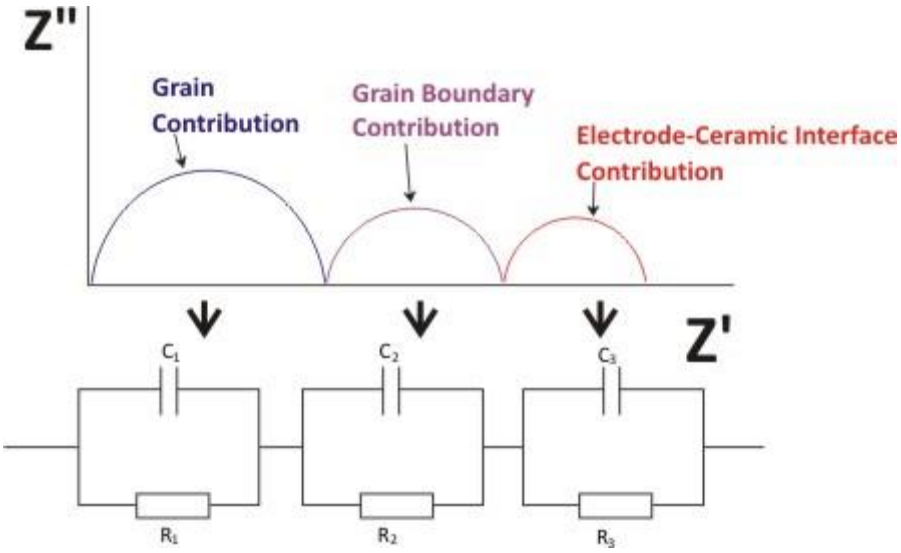

Fig. 3.6 schematic Z* plots of a ceramic with grain, grain boundary and electrode-ceramic interface contributions to the impedance response.

3.3.2.3 Constant Phase Element (CPE)

In 1977, Jonscher summarized the dielectric relaxation of a wide range of materials, and proposed the universal power law of dielectric behaviour which applies to the high frequency part of the frequency spectrum of conductivity between 0.1 Hz to 1 GHz:

$$\sigma \propto \omega^n \tag{3.17}$$

where σ is the conductivity, ω is the angular frequency, and n is the order number. He proposed that the distribution of relaxation time in the material led to the continuous spectrum of relaxation processes, resulting in the power law dependence. [163]

A component which has such response is called a CPE. The impedance response of a CPE takes the form:

$$Z^*_{CPE} = \left[A(j\omega)^n \right]^{-1} \tag{3.17}$$

where A and n are two frequency-independent but usually temperature dependent parameters. The phase angle of CPE is –nπ/2 for all frequency. From a phase angle perspective, it could be concluded that the electrical performance of a CPE is somewhere between a resistor (ϕ = 0) and a capacitor (ϕ = -π/2) when 0 < n < 1, which is the case for most materials. More recently, cases where n > 1 have been observed in a wide range of disordered materials including polymers, molecular liquids, ionic liquids, supercooled liquids, glasses, ionic conductors and doped semiconductors. [164-167]

A CPE is very useful in describing the non-ideal relaxation process that take place across the material. As shown in Fig. 3.7, without the CPE element, the conductivity would not show a power law dependence at high frequency as in real materials. Many theories have been proposed regarding the physical meaning of CPE such as ionic diffusion at the material-

electrode interface [168, 169] or inhomogeneity on different scale lengths, including ionic (defects), lattice, core-shell, grain, grain boundary and different bulk regions. [170, 171] It is widely accepted that the fitting of impedance response of real material requires CPE but no consensus has been reached regarding its exact physical implication.

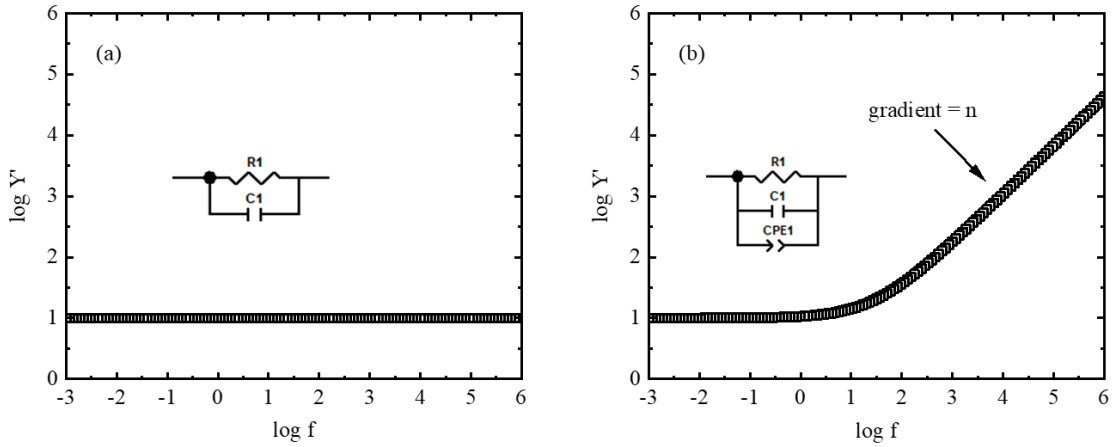

Fig. 3.7 log conductivity-frequency spectrum of (a) a parallel R-C element, and (b) a parallel R-C-CPE element.

3.3.2.4 Warburg Impedance (W)

In an electrochemical system, the diffusion of charged species (ions or electrons) is the dominant transport mechanism. The Warburg impedance arises due to the slow diffusion of these charged species in the electrode.

To analyse this diffusion phenomenon, we may consider a one-dimensional diffusion equation with a constant diffusion coefficient (D) by using second Fick's law of diffusion:

$$\frac{\partial C(x,t)}{\partial t} = D\frac{\partial^2 C(x,t)}{\partial x^2} \tag{3.18}$$

where C(x,t) is the concentration of species at the coordination of x and the time of t.

If one boundary is set at x = 0, which is the electrode-electrolyte Interface, another one is set at x = L, which is in the electrode or electrolyte with the x axis towards the direction of diffusion, a general solution to equation (3.18) could be obtained:

$$C = A\sinh[\sqrt{\frac{i\omega}{D}}(L-x)] + B\cosh[\sqrt{\frac{i\omega}{D}}(L-x)] \tag{3.19}$$

When the system has an open boundary and finite diffusion length, the Dirichlet boundary condition ($C_{x=L} = C_0$) can be applied to equation (3.18), yielding a simplified solution of:

$$C = A\sinh[\sqrt{\frac{i\omega}{D}}(L-x)] \tag{3.20}$$

In this case, when the measurement frequency is high, the impedance response is a 45° spike in the Z* plane, and when the measurement frequency is closing to zero, the spike gradually collapses to the Z' axis, which is referred to as a resistive cut-off (solid lines in Fig. 3.8). For electroceramics, the Warburg impedance is usually generated by the diffusion of ions in the electrode. And for samples with an ion-blocking electrode, the value of this intercept is usually the electronic resistance.

When the system has a blocked boundary with finite diffusion length, the Zero flux Neuman boundary condition (dC/dx = 0) could be applied to equation (3.18), and a general solution of:

$$C = B\cosh[\sqrt{\frac{i\omega}{D}}(L-x)] \tag{3.21}$$

is obtained. In this case, when the measurement frequency is high, the impedance response is still a 45° spike in the Z* plane, and when the measurement frequency is closing to zero, the Z* plot will become close to parallel to the Z" axis, which is the response of a R-C network connected in series with a capacitor, so is often referred to as a capacitive cut-off (dashed lines in Fig. 3.8).

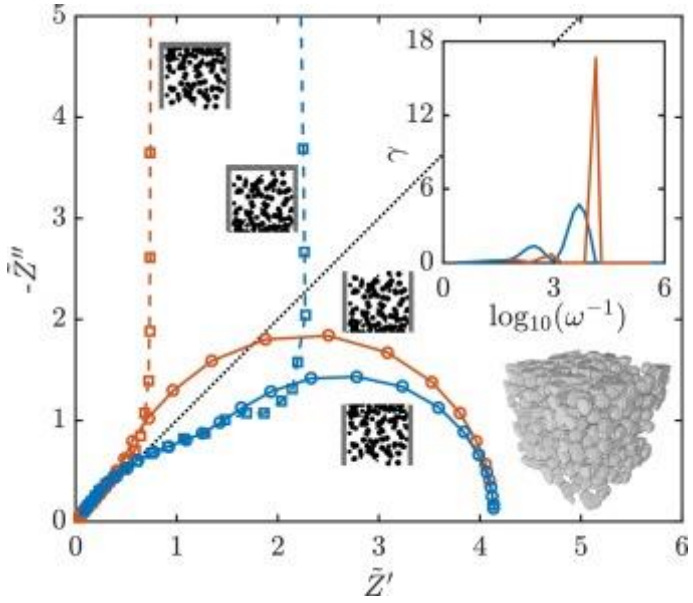

Fig. 3.8 Simulated impedance spectra for a synthetic packing of spherical particles with porosity linearly increasing (blue lines) or decreasing (red lines) from bottom to top. The top boundary can be either open (solid lines) or closed (dashed lines). The inset shows the distribution of relaxation times for the cases with open boundaries. [172]

The equivalent circuit which depicts the Warburg impedance is more complex than the first few components introduced. The transmission line model which composes of a series of R and C has been used for the description of the diffusion behaviour, as shown in Fig. 3.9(a). This model is sometimes confused with the case for a porous electrode in an electrolyte without any diffusion phenomenon. As explained in Fig. 3.9, although the two phenomena

result in the same equivalent circuit model, the physical implication of the model is quite different.

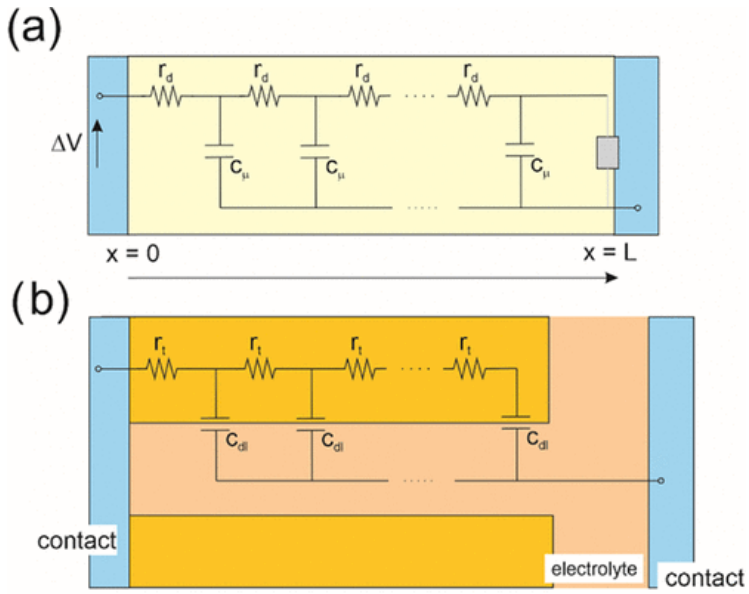

Fig. 3.9 (a) transmission line model for the diffusion in a layer with a thickness of L, distributed chemical capacitance C_μ and diffusion resistance r_d. The perturbation of voltage is applied at x = 0. The element at x = L varies with different boundary condition for the diffusion. For a blocked boundary, it is an open circuit; for an absorbing boundary, it is a close circuit. (b) transmission line model for a porous electrode with distributed double layer capacitance C_{dl} and transport resistance r_t. [173]

3.3.3 Electromotive Force Measurement (EMF)

Electromotive force (EMF) is the energy transferred to an electric circuit per unit charge:

$$E = \frac{W}{Q} \tag{3.22}$$

where W is the work done by moving the charge Q from the low potential point in a circuit to a high potential point. Thus, EMF is not a physical force, but the source voltage of a circuit, with the unit of V.

By comparing the EMF difference of the sample and a reference oxide ion conductor, such as yttria-stabilised zirconia (YSZ), under the same oxygen partial pressure (pO_2) difference and temperature, the oxygen ion transport number of the sample could be calculated. Take the system shown in Fig. 3.10 as an example. Based on the Nernst equation of electrochemical system, the potential difference between a pair of electrodes out of the tube and inside the tube can be expressed as:

$$E = t_{ion} \frac{kT}{4e} \ln\left(\frac{p_{O_2}^{in}}{p_{O_2}^{out}}\right) \tag{3.23}$$

where k is the Boltzmann constant, T is the temperature in kelvin, e is the elementary charge of 1.602*10^{-19} C, $p_{O_2}^{in}$ is the oxygen partial pressure inside the tube, $p_{O_2}^{out}$ is the oxygen partial pressure outside the tube, and t_{ion} is the oxygen transport number between the two electrode:

$$t_{ion} = \frac{\sigma_{O^{2-}}}{\sigma_{total}} \tag{3.24}$$

where $\sigma_{O^{2-}}$ and σ_{total} are the oxygen ion conductivity and total conductivity, respectively. For a set of measurement taken at certain temperature, the sample and YSZ tube are in the same pO_2 gradient, so the t_{ion} of the sample can be calculated with:

$$t_{ion,sample} = \frac{E_{sample}}{E_{YSZ}} t_{ion,YSZ} \tag{3.25}$$

YSZ is considered to be a pure oxide ion conductor (i.e. t_{ion} = 1) at high temperatures (> 600 °C). Thus, $t_{ion,\ sample}$ could be obtained straight forward with equation (3.25).

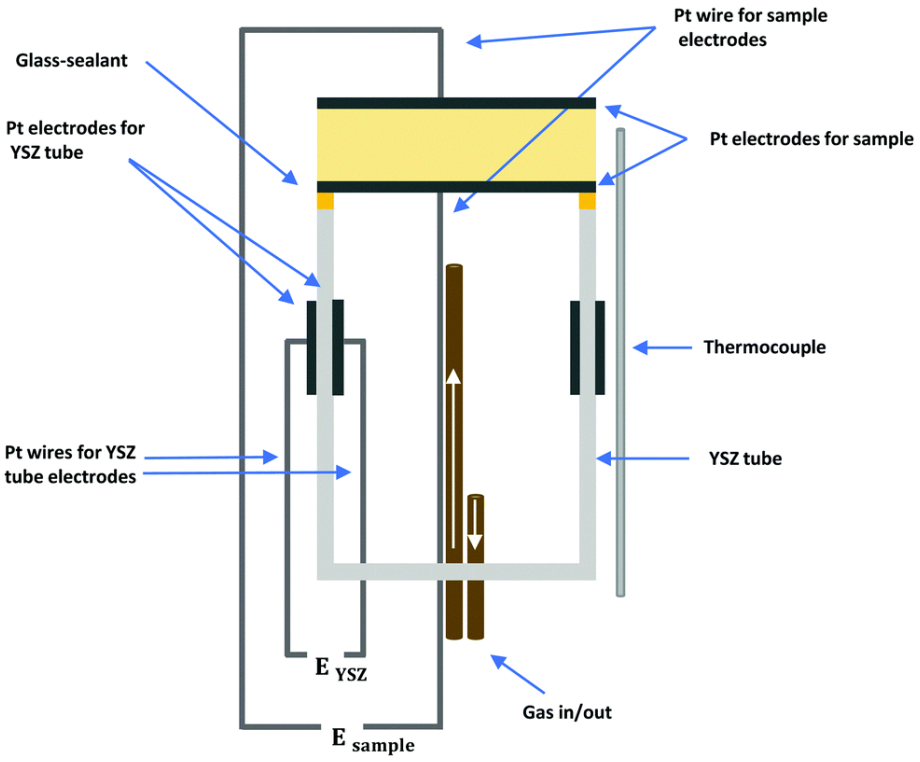

Fig. 3.10 Schematic diagram of the set-up used for oxygen ion transport number measurements. [174]

Oxygen ion transport number measurements were performed using a Probostat system (NorECs Norwegian Electro Ceramics AS). A sample coated was sealed onto an YSZ tube using a commercial glass frit. During the measurement, lab air was used as the outer tube atmosphere and flowing N_2 gas (99.998 % purity) as the inner tube atmosphere to generate a pO_2 gradient. The pO_2 difference was monitored by measuring the voltage across the inner and outer electrodes on the YSZ tube. The voltage was measured using a Keithley 182

sensitive digital voltmeter. Readings are taken at temperatures between 600 – 800 ℃ with the set up equilibrated for 24 hours at each temperature before taking a measurement.

3.3.4 Polarisation-electric field measurement (P-E)

The P-E response of a sample may be analysed by a charge/current integration method following with compensation by a variable resistor R_v, as shown in Fig. 3.11. [175-177] Most dielectric material may be considered as a parallel R-C component during P-E measurement. Thus, the phase shift caused by R may be compensated with R_v.

Before the measurement, a DC bias is applied to the circuit to determine the resistance of the sample. The value of R_v is adjusted so that V_1 remains constant over time with the DC bias, signifying the leakage current fully compensated. The resistivity of the sample (R) is assumed to be constant with electric field, so the R_v value is fixed for each measurement. During the measurement, voltage over the sample is extracted by the horizontal plates of the oscilloscope with a value of $V\text{-}V_2$. Polarisation of the sample is extracted by the change in V_1 monitored by the vertical plates of the oscilloscope.

Compensation with R_v usually removes the contribution of conductive current, leaving only the displacive current which gives reliable P-E loops and provides information on the dipole re-orientation in the material. However, beside ohmic conduction, other mechanisms such as space charge, Schottky, and Poole-Frenkel conduction are possible in the sample, which results in variable conductivity with varying electric field. [178, 179] These cases are commonly seen in more conductive samples, where a fixed R_v for each measurement would not fully compensate for the conduction with increasing field, which gives an inaccurate P-E loop. In conclusion, we need to evaluate the sample conditions, instrument settings, measurement conditions, current-electric field (I-E) loop should be analysed in conjunction with the P-E loop to get accurate interpretation of the measurement result.

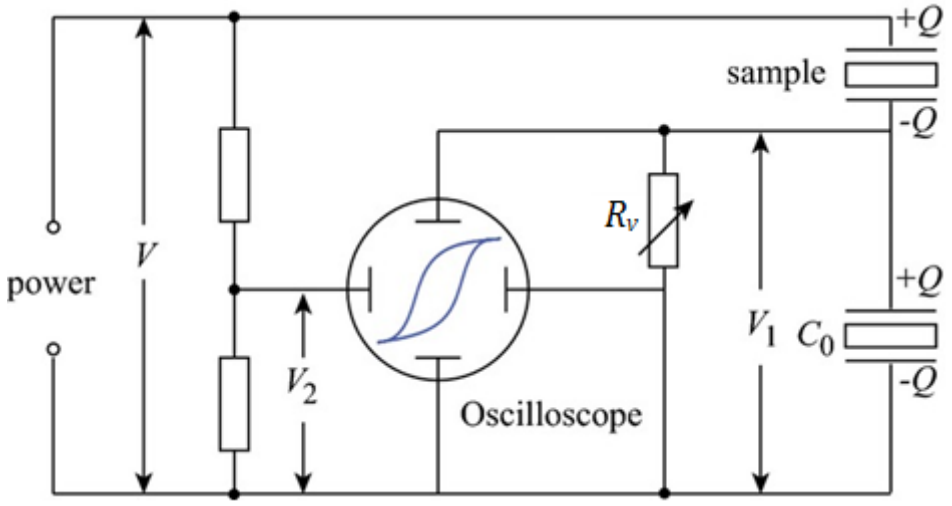

Fig. 3.11 Schematic circuit of the Sawyer-Tower bridge for measuring the P-E characteristics of materials.

The samples were ground to ~0.02 mm thick, sputtered with gold electrode on both sides, then immersed in silicon oil for the measurement to avoid dielectric breakdown over the edge of the sample. Measurement was performed at 1 Hz with TF 2000 ferroelectric tester (AixACCT, Germany). The maximum polarisation (P_{max}), remanent polarisation (P_r), and coercive field strength (E_c) were extracted from the measured P-E loops. Energy storage performance are calculated from the P-E loop with integration function in the Origin software (OriginLab). The principles of calculation are introduced in section 2.2. From the P-E hysteresis loop, the electrical energy per unit volume released into the circuit during withdrawal of the electric field (W_{rec}) and its ratio with the energy charged into the material (η) are:

$$W_{rec} = \int_{P_r}^{P_{max}} E \, \mathrm{d}P \tag{3.26}$$

$$\eta = \frac{W_{rec}}{W_{total}} * 100\% \tag{3.27}$$

where W_{total} is the total energy density.

4 Results and Discussion

4.1 Introduction

For the BT-rich end of the solid solution, a dopant (donor/acceptor) study was conducted to optimise and investigate the structure-property relations. As a consequence of this work, a rare earth, Pb and Bi free X6R dielectric was developed. The electrical microstructure of BT-NN ceramics was analysed using impedance spectroscopy and capacitance-temperature measurements to a) discern the ideal starting composition and b) to determine a feasible strategy with respect to dopants for optimizing energy density.

For the NN-rich composition a third end member was introduced to enhance relaxor characteristics, increasing the BDS and thereby the potential energy storage density. Finally, prototype MLCCs were fabricated to demonstrate the feasibility of device manufacture.

4.2 Ceramic Fabrication

Ceramics were fabricated using solid state reaction and densification. In this section, the ceramic preparation procedure is described with $BaTiO_3$-0.1$NaNbO_3$ (BT10NN) used as an example to illustrate the process.

The raw materials used in this project are all commercially available. Table 4.1 shows the purity and supplier of each raw material. No attempt, however, was made to characterise the nature and type of impurities associated with each raw material.

Table 4.1 Purity and supplier of raw materials used in the project

No	Chemical	Purity (%)	Supplier
1	$BaCO_3$	99.9	Sigma Aldrich
2	TiO_2	99.9	Sigma Aldrich
3	Na_2CO_3	99.6	Acros Organics
4	Nb_2O_5	99.5	Alfa Aesar
5	Nd_2O_3	99.9	Stanford Materials Corporation
6	MgO	99	Sigma Aldrich

Accurate weighing of raw material is critical in achieving the desired stoichiometry of the final product. Li et al have shown that only 1% of deviation in Bi concentration alters the electrical performance of $Na_{0.5}Bi_{0.5}TiO_3$ significantly. [180] The raw materials for fabricating ceramics are prone to absorb moisture and CO_2 from the atmosphere. As a result, hydroxide, carbonates and hydrocarbonates are likely to be present on the powder surface with the level of contamination dependent on the composition, particle size and storage conditions. To reduce the effect of these contaminations, raw materials were dried at different temperatures before weighing. $BaCO_3$ and Na_2CO_3 were dried at 180 ℃ to avoid decomposition. Other oxides were dried at 900-1000 ℃ for 8 hours with powders kept at 200 ℃ until weighing.

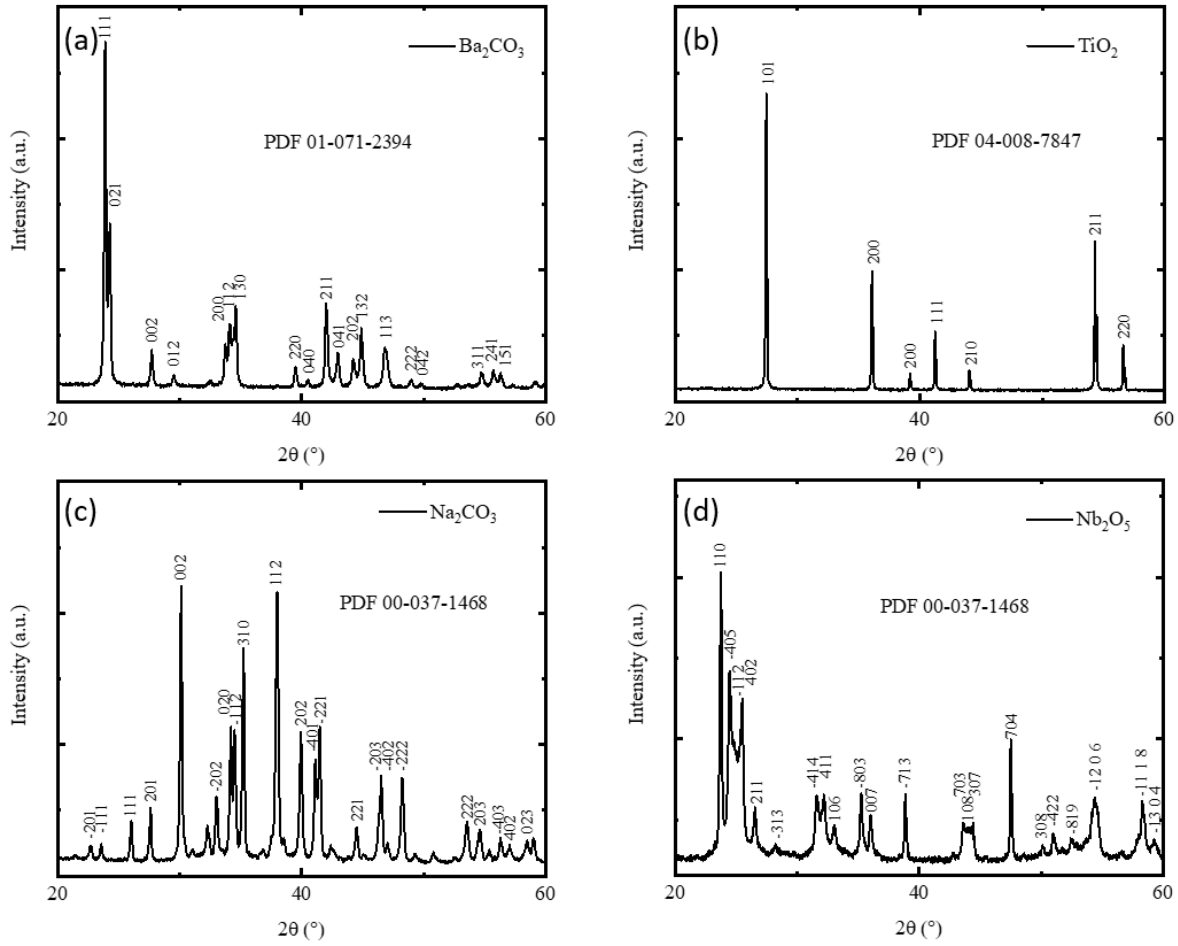

Fig.4.1 XRD patterns for raw materials of (a) $BaCO_3$, (b) TiO_2, (c) Na_2CO_3 and (d) Nb_2O_5, with their corresponding ICDD PDF card numbers and (hkl) index noted in the figures.

The XRD pattern for raw materials of $BaCO_3$, TiO_2, Na_2CO_3 and Nb_2O_5 are shown in Fig. 4.1. The matched PDF card number and hkl indices of each diffraction peaks are denoted. After drying, the raw materials were weighed with a Precisa 923M-202A balance with ± 1 mg accuracy. Each batch was around 45 g to ensure a similar processing procedure for all compositions.

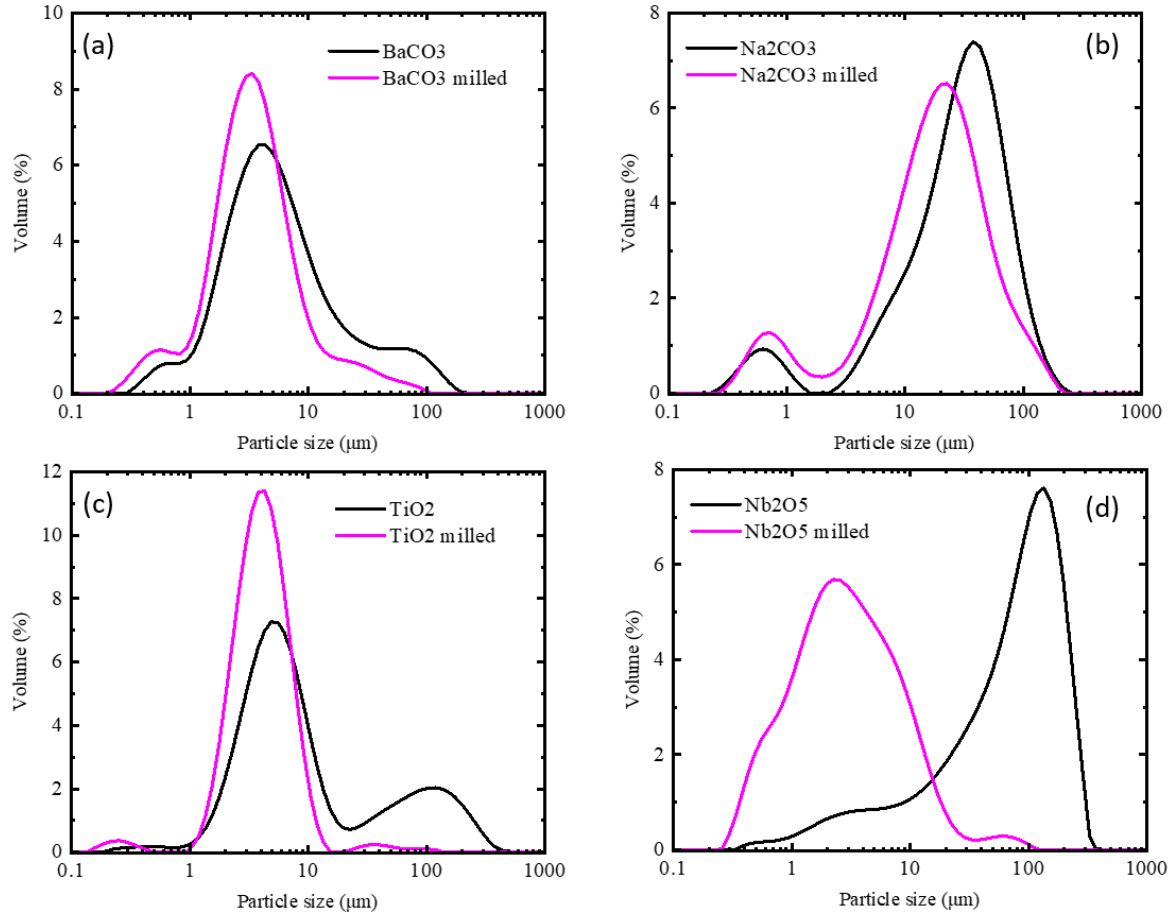

Fig. 4.2 The particle size distribution before and after ball mill for raw materials of (a) $BaCO_3$, (b) Na_2CO_3, (c) TiO_2, and (d) Nb_2O_5.

The particle size distribution of $BaCO_3$, Na_2CO_3, TiO_2, and Nb_2O_5 before and after milling are illustrated in Fig. 4.2. The particle sizes of all raw materials were reduced by the ball milling process. Smaller particle size facilitates the diffusion of ions and phase formation during calcination. In this project, powders were ball milled for 18 hours at 300 rpm to obtain a reduced and homogenous particle size distribution. Longer milling time may result in ZrO_2 contamination from the milling media.

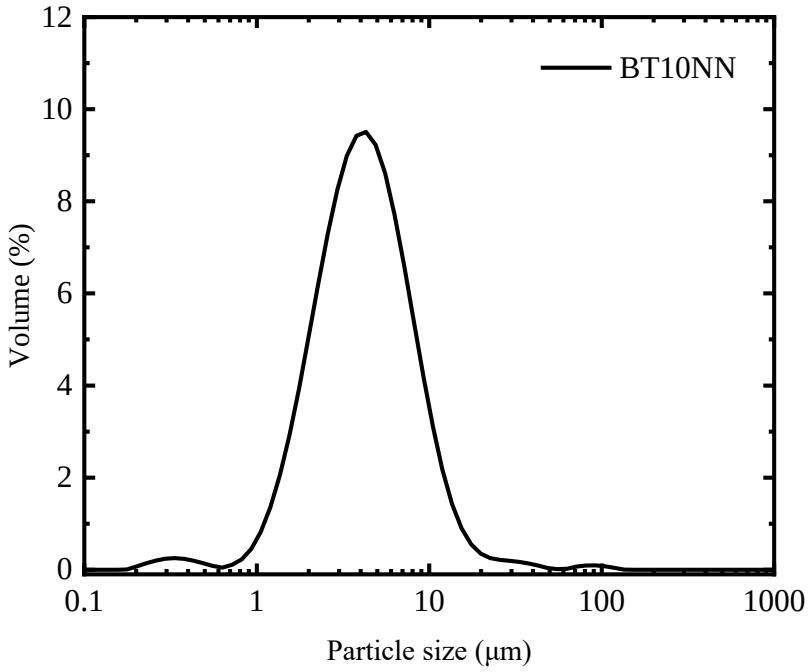

Fig. 4.3 Particle size distribution of calcined and ball milled BT10NN powder.

The particle size distribution of calcined and milled BT10NN powder is shown in Fig. 4.3. A uniform distribution with an average particle size of ~6.3 μm was obtained.

After calcination and ball milling, 0.5 wt% of poly(vinyl alcohol) was added to the powder as binder to encourage granulation. The mixture was lightly ground with a pestle and mortar, then sieved through a 250 μm mesh to form free-flowing granules. To make green pellets, ~ 0.3 g of powder was pressed with 50 MPa of uniaxial pressure to form compacts with 10 mm in diameter.

For sintering, the pellet was first heated to 550 ℃ at 3 ℃/min and held for 3 hours to burn out the binder and maintain mechanical stability. The pellets were then heated to the sintering temperature at 5 ℃/min and held for 2 hours to allow necking of grains and densification of the ceramic. Several sintering temperatures were tested for each composition before measuring and comparing the density of the pellets. At the optimised sintering temperature, a shrinkage of ~20% in diameter is usually seen in the pellets. Based on the above processing procedures, relative density of over 95% was routinely achieved.

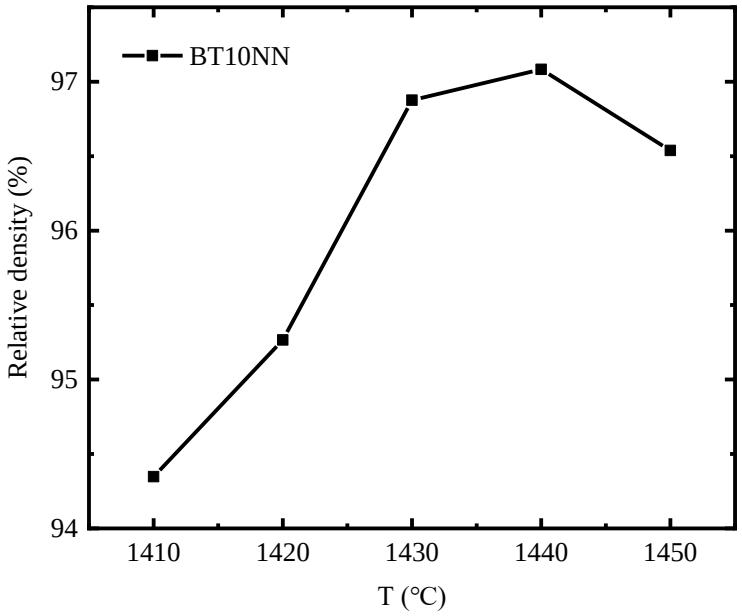

Fig. 4.4 Dependence of relative density of BT10NN ceramic on sintering temperature from 1410 – 1450 ℃.

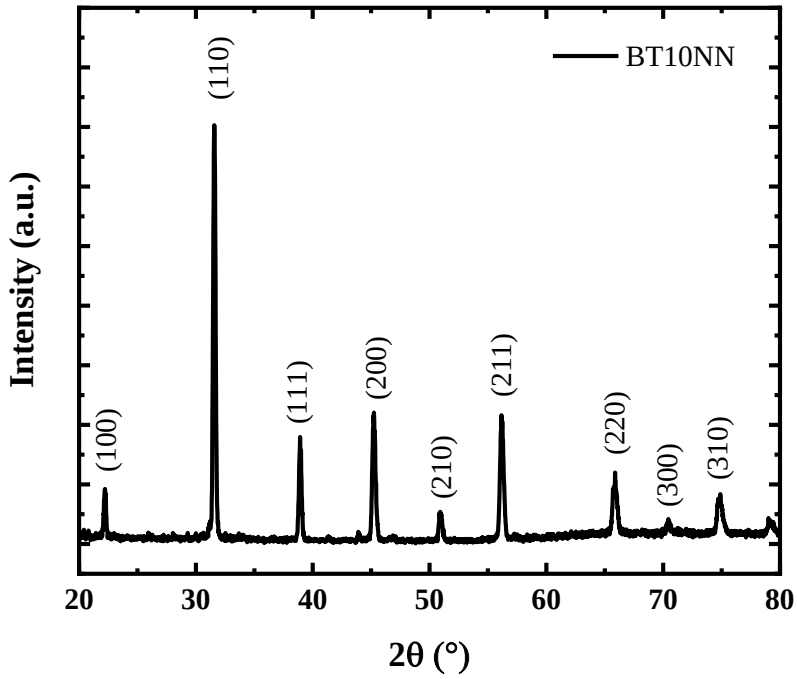

Fig. 4.5 XRD pattern of the sintered BT10NN ceramic.

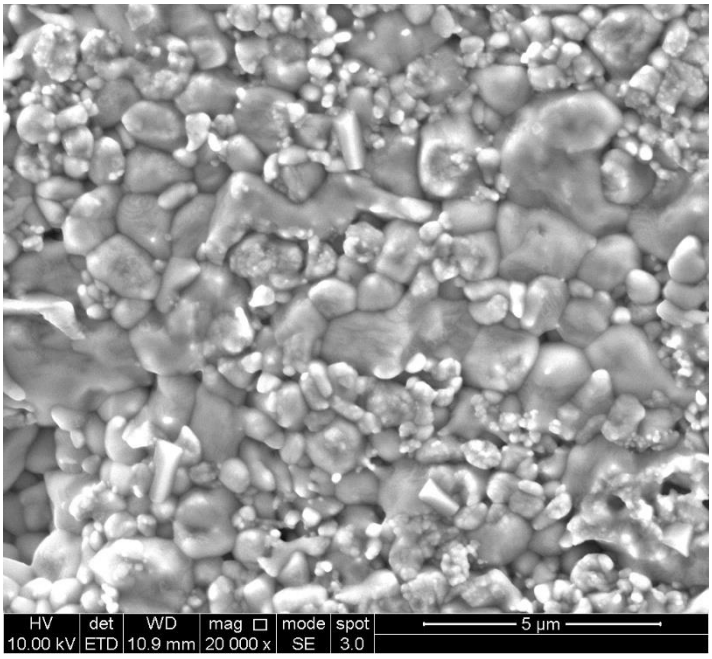

Fig. 4.6 SEM image of the polished and thermally etched BT10NN ceramic.

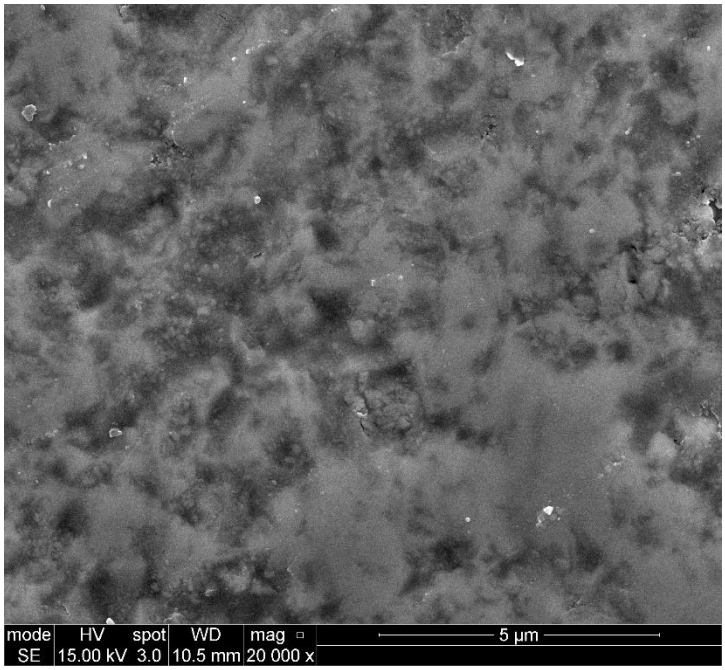

Fig. 4.7 SEM image of the polished BT10NN ceramic.

The sintering temperature of BT10NN ceramic is determined by evaluating the relative density of the ceramic. As shown in Fig. 4.4, the optimised sintering temperature for BT10NN is 1440 ℃. The crystal structure of the sintered ceramic is determined by XRD, as shown in Fig. 4.5 in which a cubic phase is identified. SEM images of the polished and thermally etched ceramic suggest two grain size distributions, one sub-micron and the other 1-3 microns in diameter.

Fig. 4.6 shows an SEM image of a polished and thermally etched BT10NN ceramic, which exhibits a smaller particle size than measured with the laser diffraction technique shown in Fig. 4.3. The difference may be due to either the presence of agglomerates of smaller particles during the laser diffraction measurement or a result of the SEM image only being a two-dimensional interception of the ceramic but not a three-dimensional representation of the grain morphology. Fig. 4.7 confirms that a dense ceramic is achieved for BT10NN.

4.3 (1-x)$BaTiO_3$-x$NaNbO_3$ (0.05≤x≤0.25)

XRD patterns of the polished surface of sintered BT-xNN pellets are shown in Fig. 4.8. All samples were pseudocubic but a minor secondary phase ($Ba_5Ti_{14}Nb_2O_{39}$) was present in samples with x ≥ 0.1. The SEM image in Fig. 4.9 shows two grain size distributions for all samples, one with sub-micron diameters, another with 1-3 microns in diameter. No obvious trend is observed in terms of the diameter or volume ratio of these two distributions with respect to x.

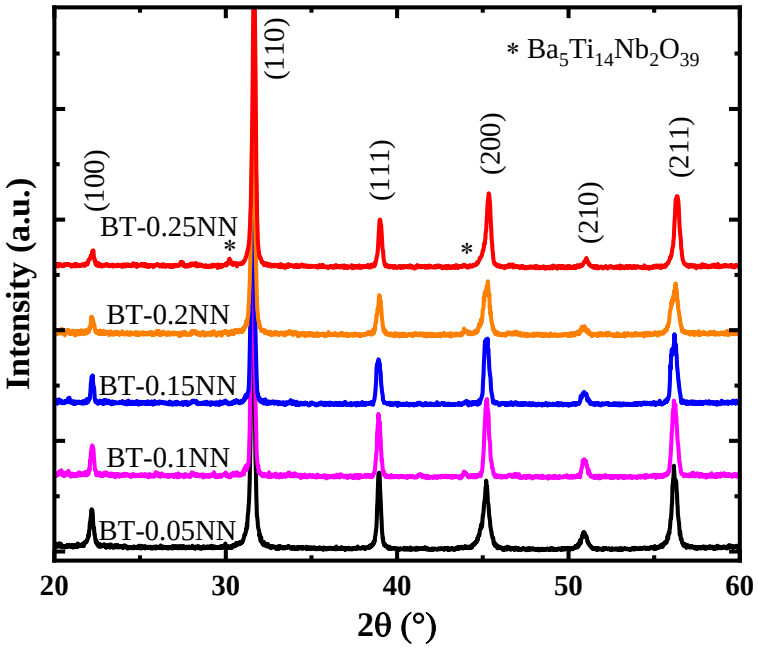

Fig. 4.8 XRD patterns of BT-xNN (0.05≤x≤0.25) ceramics.

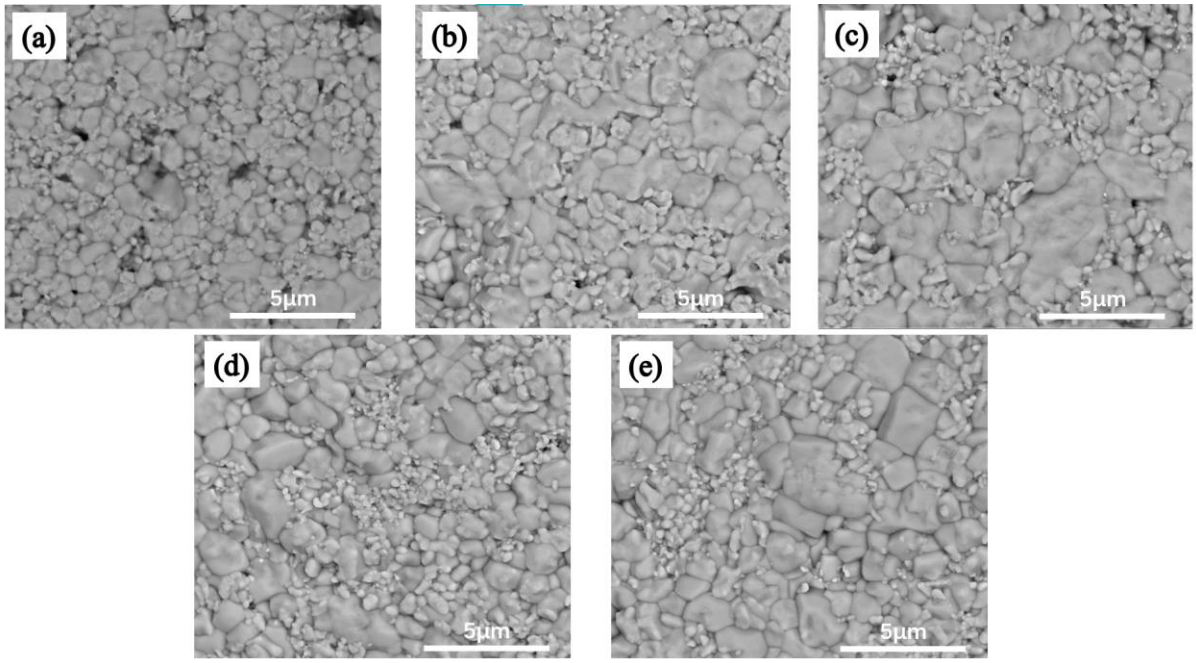

Fig. 4.9 SEM images of (a) BT-0.05NN, (b) BT-0.1NN, (c) BT-0.15NN, (d) BT-0.2NN, (e) BT-0.25NN.

The temperature dependency of permittivity ε' and loss tangent tan δ of BT-xNN are shown in Fig 4.10. A core-shell type response is observed in all compositions. The permittivity decreased with increasing x for x < 0.2 with a dielectric anomaly at 112 ℃, close to the Curie temperature of BT. However, the change in gradient at ~ 120 ℃ becomes less obvious for x = 0.25, presumably due to a more homogeneous distribution of ions in the ceramic which lessens the core-shell dielectric response. The dielectric loss increased significantly with increasing NN content, especially at high temperatures, which may be due to Na_2O loss during sintering creating A-site and oxygen vacancies, the latter of which are known to move under field at elevated temperatures in perovskites.[181]

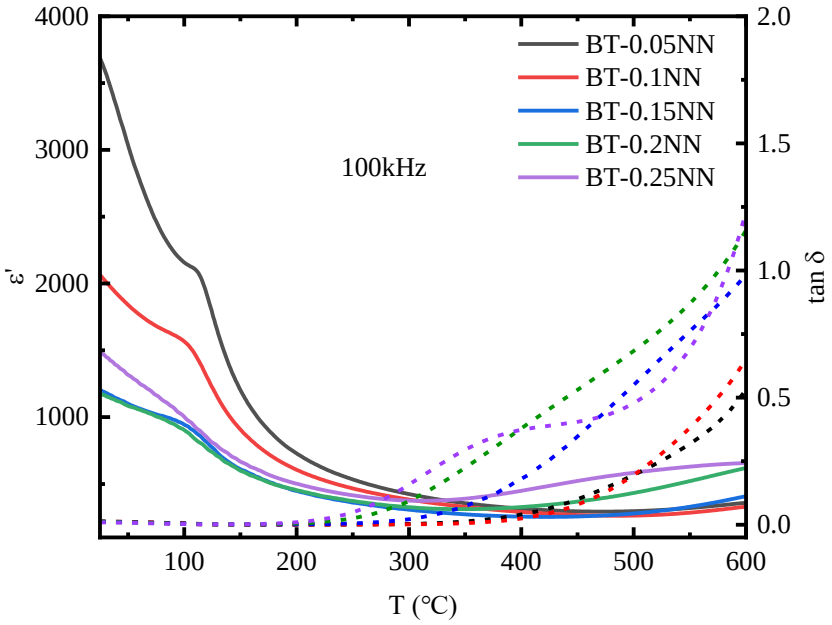

Fig. 4.10 Temperature dependency of ε' and tan δ of BT-xNN.

The high field response of BT-xNN ceramics is shown in Fig. 4.11. The trend of change in polarisation was consistent with the LCR permittivity measurements, where the polarisation under the same field decreased with x until x = 0.2, then increased from x = 0.2 to x = 0.25. The highest AC bipolar BDS is for x = 0.1 (BT10NN). The core-shell type dielectric response (ε' > 1000 up to 141 ℃) indicates that x = 0.1 is potentially a good dielectric for capacitor application, Fig. 4.12. Impedance data as a function of oxygen partial pressure (pO_2) shows that the conductivity increased when pO_2 drops from ~0.2 atm (air) to ~10^{-3} atm (N_2). The increase in conductivity indicated that more mobile charge carriers were present in the material when oxygen ions were lost from the lattice. The dominant charge carriers at this temperature and oxygen partial pressure were most likely electrons, and therefore conductivity was considered n-type. Due to the interesting dielectric and ferroelectric response of BT10NN ceramic, a donor/acceptor dopant study was performed to better understand the relationship with crystal and defect chemistry.

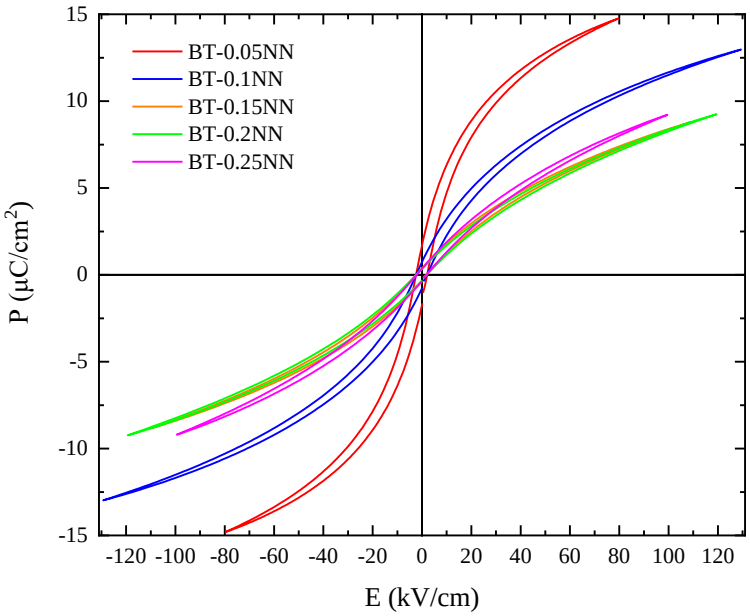

Fig. 4.11 P-E loops of BT-xNN ceramics at room temperature.

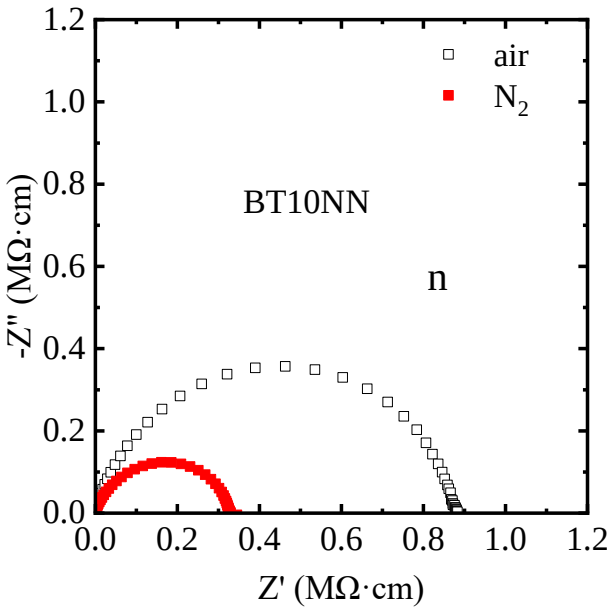

Fig. 4.12 Impedance complex plane plots of BT10NN measured at 550 ℃ in flowing air and N_2 atmosphere.

4.4 Mg and Nb doped $BaTiO_3$-$NaNbO_3$ ceramics

As mentioned in section 4.2, BT10NN ceramics were of interest for further dopant study. In this section, Mg^{2+} and Nb^{5+} ions are batched with the intention of doping the B site of BT10NN, replacing Ti^{4+} and acting as an acceptor and donor, respectively. $(Ba_{0.9}Na_{0.1})(Ti_{0.9-}$

$_x$Nb$_{0.1}$Mg$_x$)O$_{3-x}$ (BTNN-100xMg) and (Ba$_{0.9}$Na$_{0.1}$)(Ti$_{0.9-5/4x}$Nb$_{0.1+x}$)O$_3$ (BTNN-100yNb) ceramics with x, y = 0.005, 0.01, 0.02 and 0.05 are prepared with methods described in section 4.1, and characterised to investigate the structure-property relationship of these compositions.

4.4.1 Phase Assemblage and Microstructure

The XRD patterns of BTNN-100xMg ceramics are shown in Fig. 4.13, which exhibit a mixture of perovskite phases, with a secondary $Ba_5Ti_{14}Nb_2O_{39}$ (PDF 00-038-1431) phase detected for $x < 0.02$, $Ba_{11}Ti_{28}O_{66.5}$ (PDF 01-073-5502) for $x = 0.02$, and $Ba_4Ti_{11}O_{26}$ (PDF 01-083-1459) for $x = 0.05$. The change in XRD profile of the secondary phase is shown in Fig. 4.14. The peaks of perovskite phases, as exemplified by (110) in Fig. 1(b), shift to higher angles with $x \leq 0.02$, then back to lower 2θ at $x = 0.05$. The unit cell volume initially shrinks and then expands. The appearance of a Nb containing second phase for $x < 0.02$ is consistent with volatilization of Na which leaves Nb in excess, compensated by the formation $Ba_5Ti_{14}Nb_2O_{39}$ second phase. As Mg concentration increases however, the second phase for $x \geq 0.02$ no longer contains Nb suggesting that it is retained within the perovskite matrix. The simplest explanation is that Mg enters in small concentrations onto the perovskite A-site, compensating in part for Na-ion vacancies and allowing Nb to be retained. However, Mg^{2+} in 12-fold (A-site) coordination is unknown since its ionic radius is normally considered too small to occupy the cuboctahedral volume. Mg^{2+} in small concentrations on the A-site however, would explain the reduction in unit cell volume for $x \leq 0.02$. [182] The expansion of the lattice for $x > 0.02$ may relate to the substitution of Mg^{2+} (0.72 Å) for Ti^{4+} (0.605 Å) onto the B-site which is compensated by O-vacancies, giving rise to a small repulsive force on the B-site sublattice. Mg^{2+} is typically known to occupy the B-site in perovskite titanates. [183, 184] Substitution of Mg onto the B site is consistent with changes to the A_{1g} vibration mode shown at ~770 cm^{-1} and ~830 cm^{-1} in the Raman spectra in Fig. 4.15. [185]

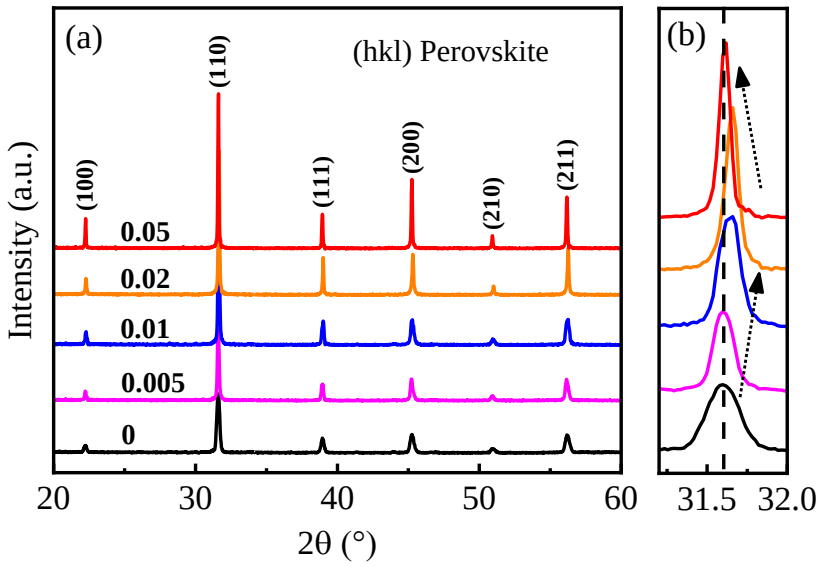

Fig. 4.13 (a) XRD patterns of BTNN-100xMg ceramics sintered at 1440-1460 °C for 2 h. (b) expanded (110) peaks in the range of 31° and 32°.

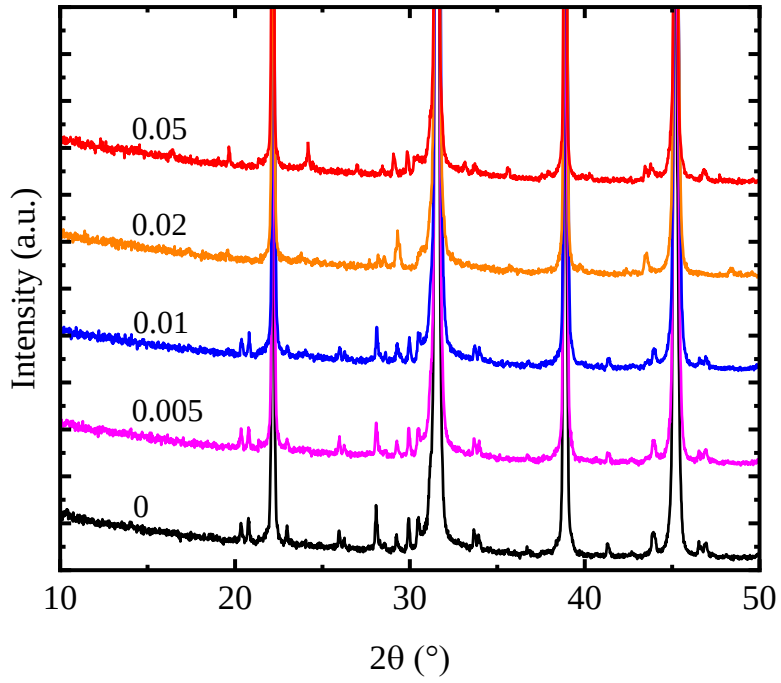

Fig. 4.14 Enlarged XRD pattern of BTNN-100xMg ceramics from 10° to 50°.

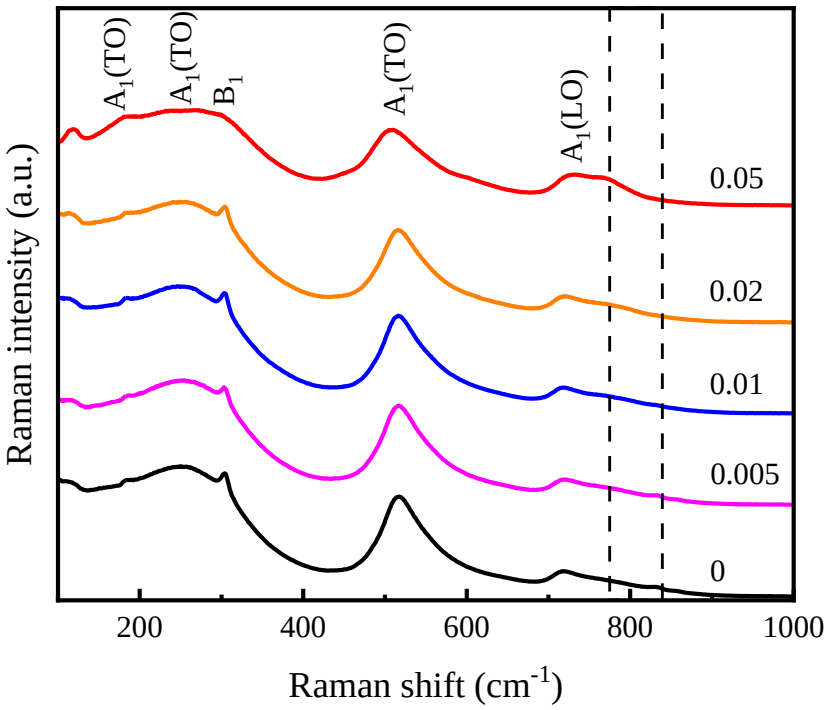

Fig. 4.15 Raman spectra with band assignments for BTNN-100xMg ceramics.

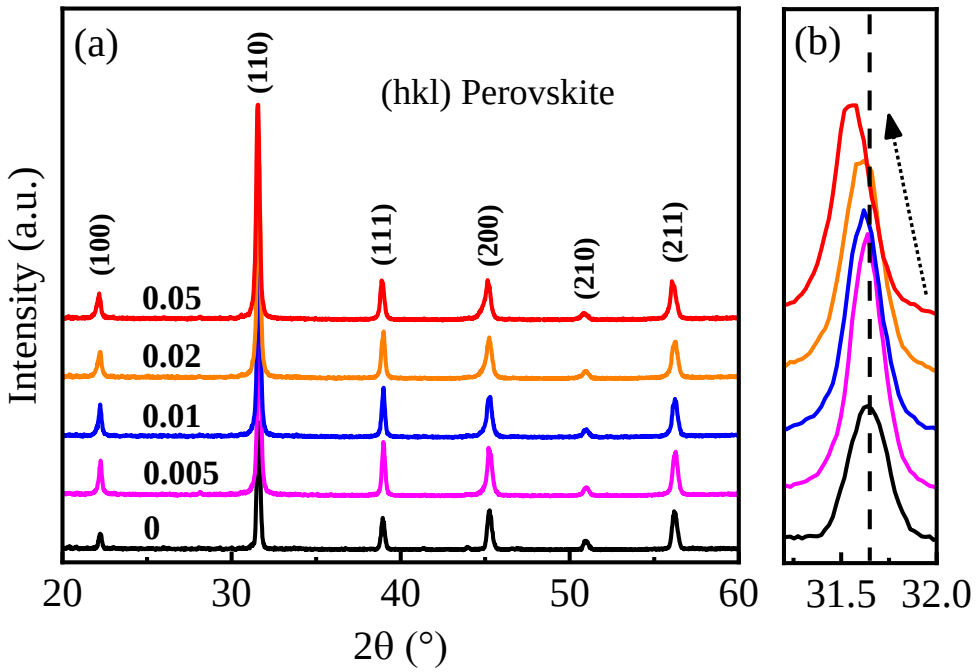

Fig. 4.16 (a) XRD patterns of BTNN-100yNb ceramics sintered at 1440-1460 °C for 2 h. (b) expanded (110) peaks in the range of 31° and 32°.

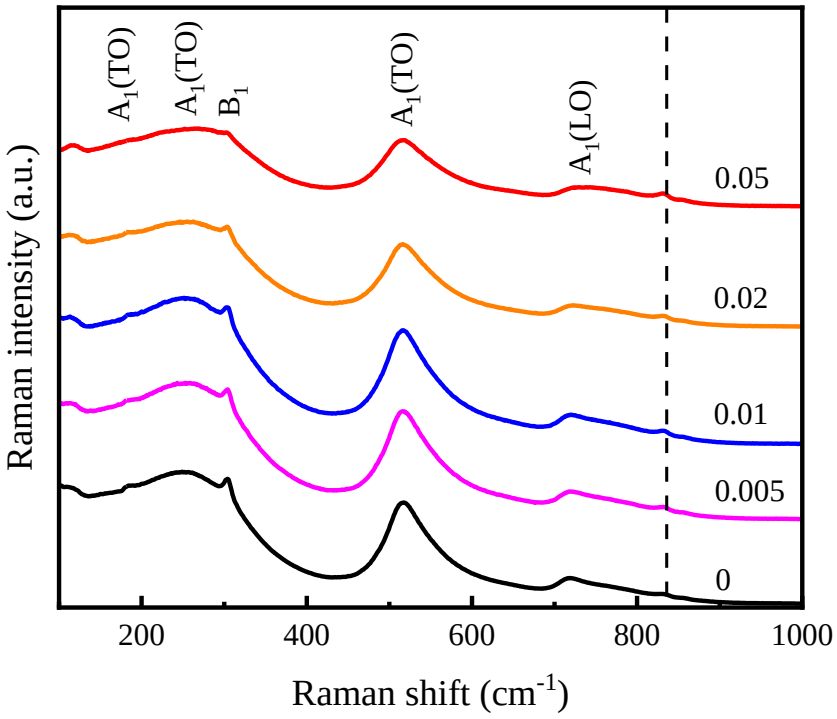

Fig. 4.17 Raman spectra with band assignments for BTNN-100yNb ceramics.

XRD patterns of BTNN-100yNb are shown in Fig. 4.16. Since Nb^{5+}(0.64 Å) is larger than Ti^{4+} (0.605 Å), Nb^{5+} substitution on B site result in an expansion in crystal lattice, causing the (110) peak shown in the expanded graph to shift to lower angles. The change in B site ion is also reflected by the enhanced Raman response from A_{1g} vibration mode associated with B-O bonds shown at ~830 cm^{-1} in the Raman spectra (Fig. 4.17). The weakened B_1 mode in Raman spectra with increasing x indicates that the structure is also more symmetric as more Nb substitute on the B site.

The defect mechanism associated with Mg^{2+} and Nb^{5+} doping are:

Since an anomaly in cell volume is detected in the XRD spectra of BTNN-100xMg ceramics, Rietveld refinements were performed on the XRD data to analyse the change in crystal structure of the compositions. A single or combination of tetragonal $P4mm$ and cubic $Pm\bar{3}m$ space group were adopted in the fitting with the best result obtained with coexistence of the two symmetries as shown in Fig. 4.17. The refinements confirm that the unit cell volume of these two phases decreases slightly then increase with x, as shown in Fig. 4.18. The phase fraction of $P4mm$ and $Pm\bar{3}m$ is ~50:50 for $x \leqslant 0.02$, but a significant increase in the proportion of cubic phase is observed for x = 0.05. This trend is confirmed by the disappearance of the B_1 mode at ~301 cm^{-1} in the Raman spectra (Fig. 4.15). [186] Based on the ionic displacements resolved in the Rietveld refinement, the spontaneous polarisation of the BTNN-100xMg samples was estimated using the Shimakawa model: [187, 188]

$$P_s = \sum_i \frac{m_i \times \Delta x_i Q_i e}{V} \tag{4.1}$$

where m_i is the site multiplicity, Δx_i is the atomic displacement along the polarisation direction, $Q_i e$ is the effective charge of the ith ion in the unit cell and V is the unit cell volume. Atomic displacement is calculated from the coordinates of ions shown in Table 4.2.

As shown in Fig. 4.17 (d), the total spontaneous polarisation decreases from ~6 to ~1 $\mu C/cm^2$ with increasing dopant concentration.

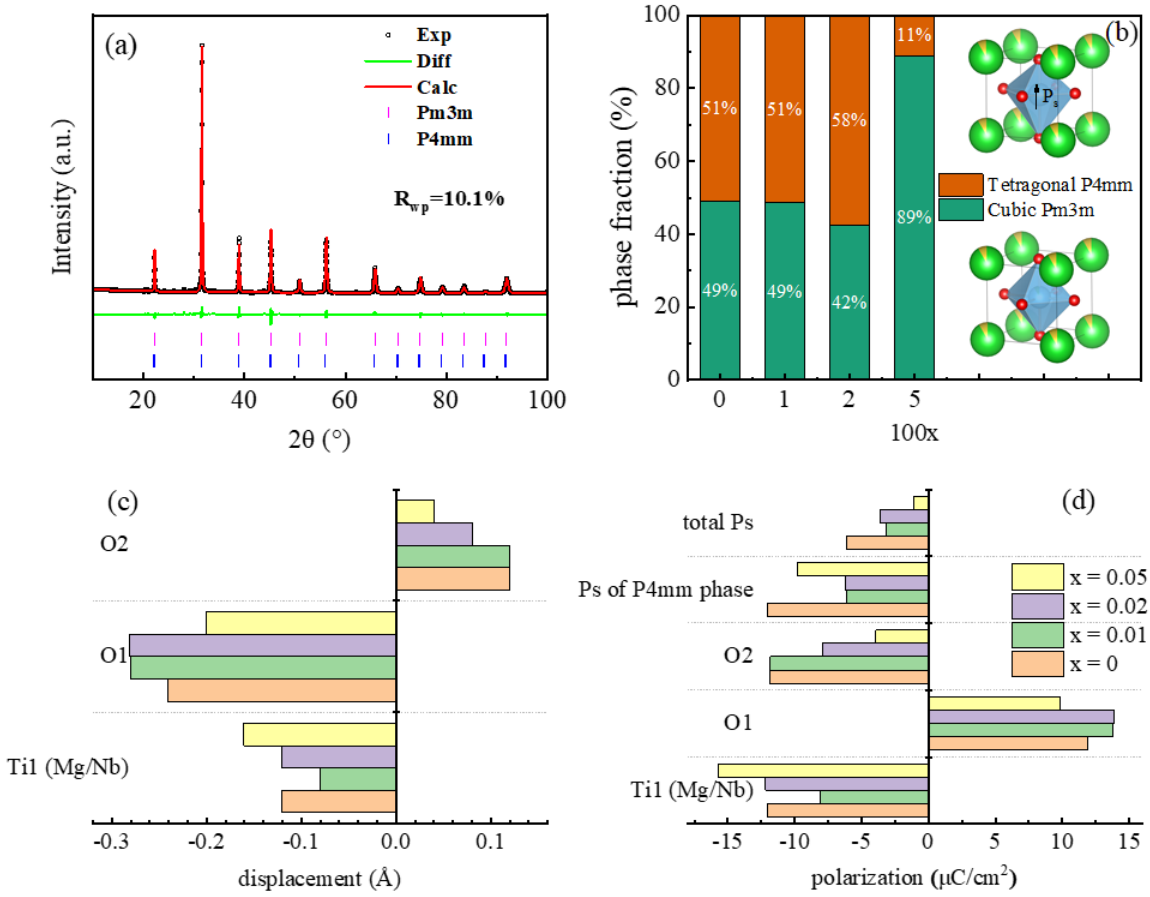

Fig. 4.17 (a) Full pattern Rietveld refinement on x = 0.01 ceramics with $Pm\bar{3}m$ and $P4mm$ space groups. (b) Change in phase assemblage of BTNN-100xMg ceramics with x, with schematic diagrams of P4mm and $Pm\bar{3}m$ structures. (c) The displacement of ions in a unit cell derived from XRD refinement results. (d) The contribution of individual ions in a unit cell to the total P_s derived from XRD refinement results.

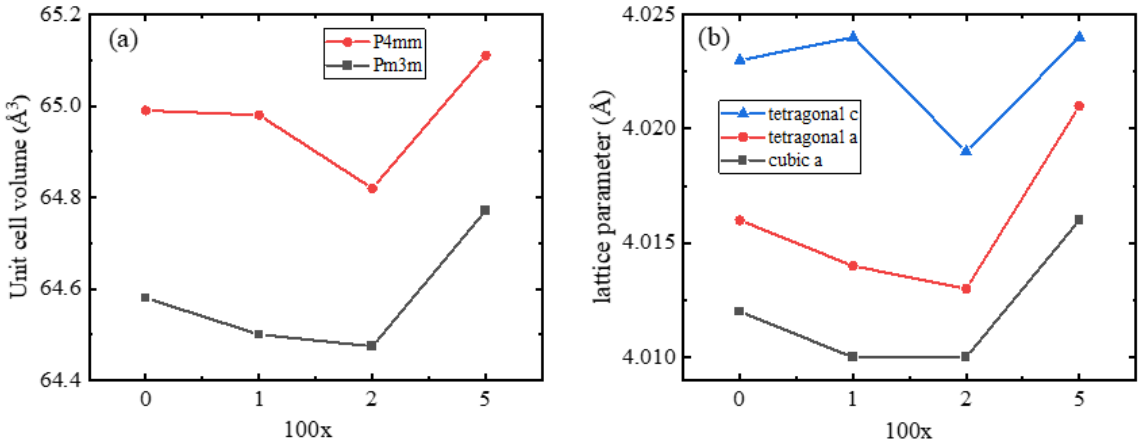

Fig. 4.18 (a) Changes in unit cell volume with increasing dopant level of BTNN-100xMg. (b) Changes in lattice parameters with x based on the refined structure.

Table 4.2 The fractional coordinates of ions in P4mm structures of BTNN-100xMg ceramics calculated from the Rietveld refinement of XRD data.

Composition	Site	Np	x	y	Z
X = 0	Ba/Na	1	0.00	0.00	0.00
	Ti/Nb	1	0.50	0.50	0.46(0)
	O1	1	0.50	0.50	0.93(1)
	O2	2	0.00	0.50	0.54(1)
X = 0.01	Ba/Na	1	0.00	0.00	0.00
	Ti/Nb/Mg	1	0.50	0.50	0.48(1)
	O1	1	0.50	0.50	0.93(1)
	O2	2	0.00	0.50	0.53(2)
X = 0.02	Ba/Na	1	0.00	0.00	0.00
	Ti/Nb/Mg	1	0.50	0.50	0.47(0)
	O1	1	0.50	0.50	0.93(1)
	O2	2	0.00	0.50	0.52(2)
X = 0.05	Ba/Na	1	0.00	0.00	0.00
	Ti/Nb/Mg	1	0.50	0.50	0.46(2)
	O1	1	0.50	0.50	0.95(1)
	O2	2	0.00	0.50	0.50(2)

The microstructure of BTNN-100xMg ceramics display dramatic changes with x, as shown in Fig. 4.19. For x < 0.02, the average grain size is ~0.5 μm, with some extremely small grains and a few that are larger but with none > 2 μm. For x = 0.02, the grain boundaries become distinct and accompanied by an increase in the average grain size to ~1.5 μm. For x = 0.05, the average grain size increases dramatically to > 10 μm. The increase in grain size is commensurate with the onset of acceptor Mg^{2+} doping onto the B-site which has been shown in BT-based materials to enhance mass transfer. [189]

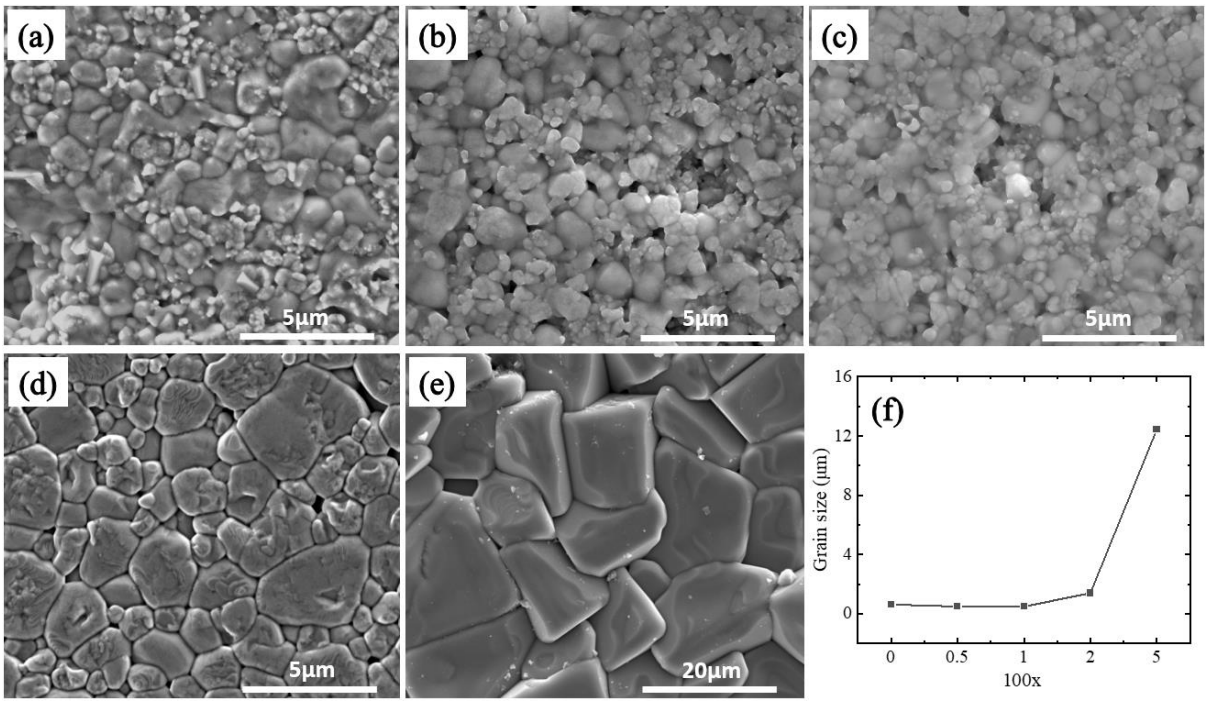

Fig. 4.19 SEM images of thermally etched polished surfaces of (a) BT10NN, (b) x = 0.005, (c) x = 0.01, (d) x = 0.02, (e) x = 0.05 ceramics, and (f) the average grain size of the BTNN-100xMg ceramics.

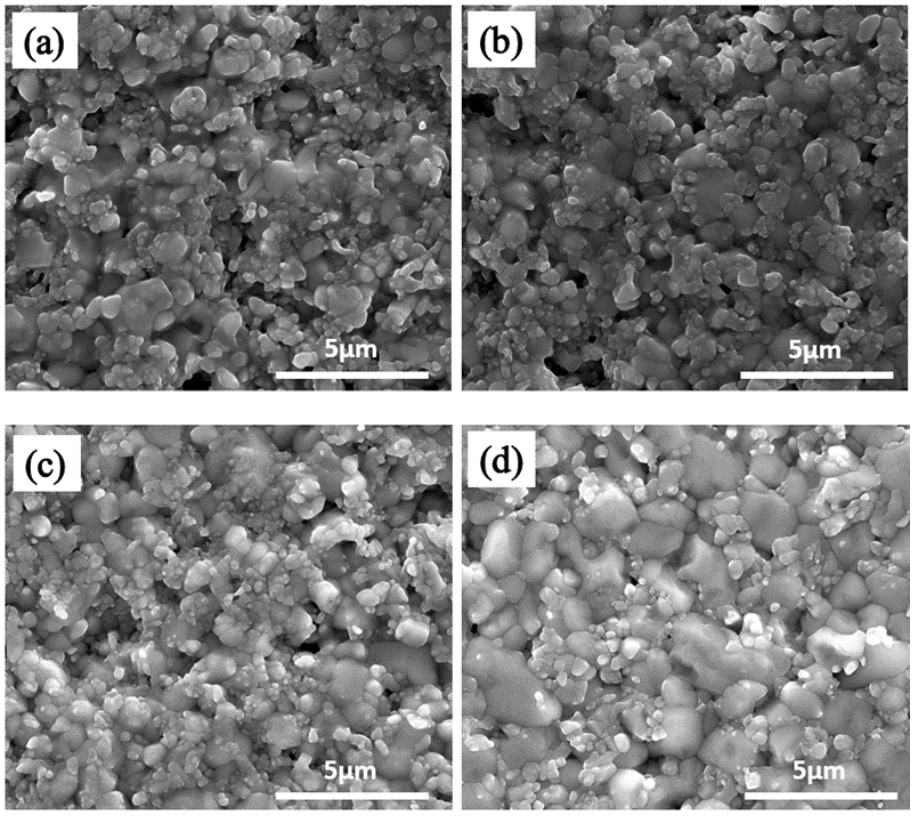

Fig. 4.20 SEM images of thermally etched polished surfaces of (a) y = 0.005, (b) y = 0.01, (c) y = 0.02, (d) y = 0.05 ceramics.

The microstructure of BTNN-100yNb ceramic does not show significant changes with increasing x, Fig. 4.20. Two groups of grains with submicron and 1-3 microns in diameters are present for all samples.

4.4.2 Low Field Dielectric and Conduction Behaviour

The permittivity-temperature plots of BTNN-100xMg ceramics are shown in Fig. 4.21 (a). In the undoped BT10NN sample, the broad phase transition suggests that the transformation from cubic to tetragonal phase is not at a distinct Curie temperature, but rather over >100 K. This is also the case for x = 0.005 and x = 0.01 and is attributed to an inhomogeneous composition and microstructure. However, a single, broad and large peak in permittivity is observed for x = 0.02, which decreases in temperature with increasing dopant concentration. The high dielectric loss of x = 0.05 suggests that the high permittivity of x = 0.05 is not entirely due to the contribution of the polar phase but also due to space charge from clusters of defects, most likely O vacancies. For x = 0.01, an additional dielectric anomaly is detected at around 32 K in Fig. 4.21(b), which may be associated with a transition to a lower symmetry phase. As shown in Fig. 4.21(c), the best dielectric temperature stability is achieved in x = 0.01, which meets the commercial specification of X6R MLCC ($\Delta C/C_0 \leq \pm 15$ % from -55 °C to 105 °C).

The permittivity-temperature plots of BTNN-100yNb ceramics are shown in Fig 4.22. The temperature of dielectric anomaly around T_c of BT remains unchanged, but the maximum temperature of the lower peak shifts to lower temperatures with increasing y. The room temperature permittivity decreased slightly at first with increasing y for y < 0.02, then dramatically from 1654 for y = 0.02 to 998 for y = 0.05. The dielectric loss remains low (~0.01) for all compositions at room temperature but increases with increasing y above 500 K.

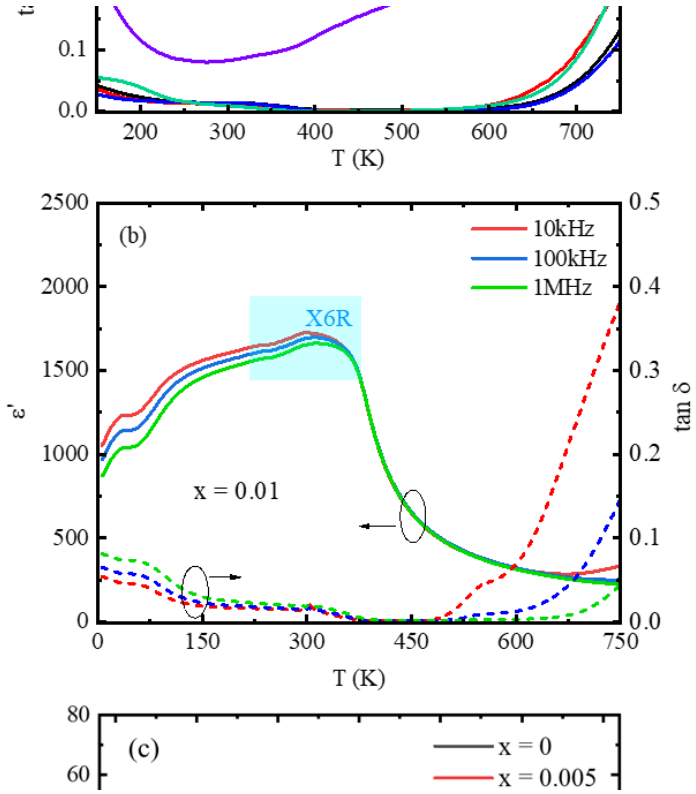

Fig. 4.21 (a) Temperature dependence of ε' and tan δ for BTNN-100xMg ceramics at 100 kHz from 150 to 750 K. (b) ε' and tan δ at different frequencies in the temperature range of 6 to 750 K for x = 0.01, with the X6R specification depicted with the cyan area. (c) Temperature Coefficient of Capacitance (TCC) of BTNN-100xMg ceramics between -55 and 105 °C.

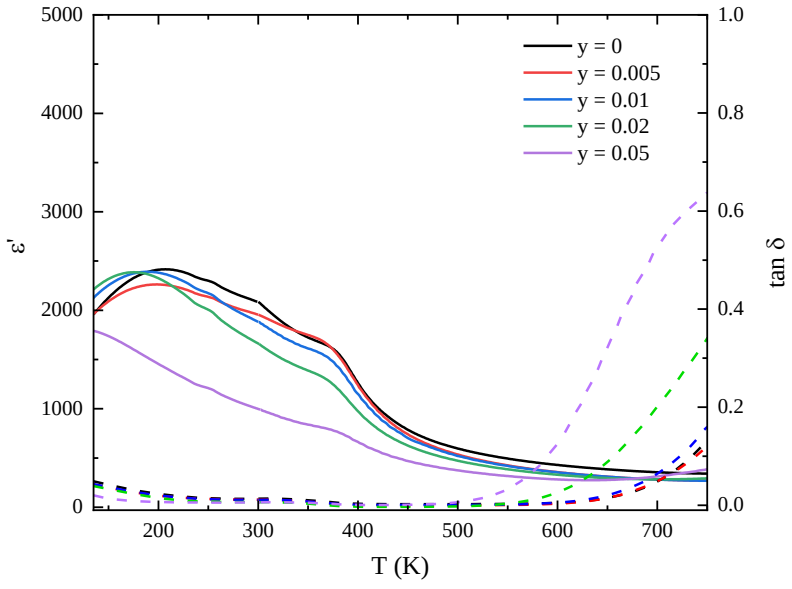

Fig. 4.22 Temperature dependence of ε' and tan δ for BTNN-100yNb ceramics at 100 kHz from 150 to 750 K.

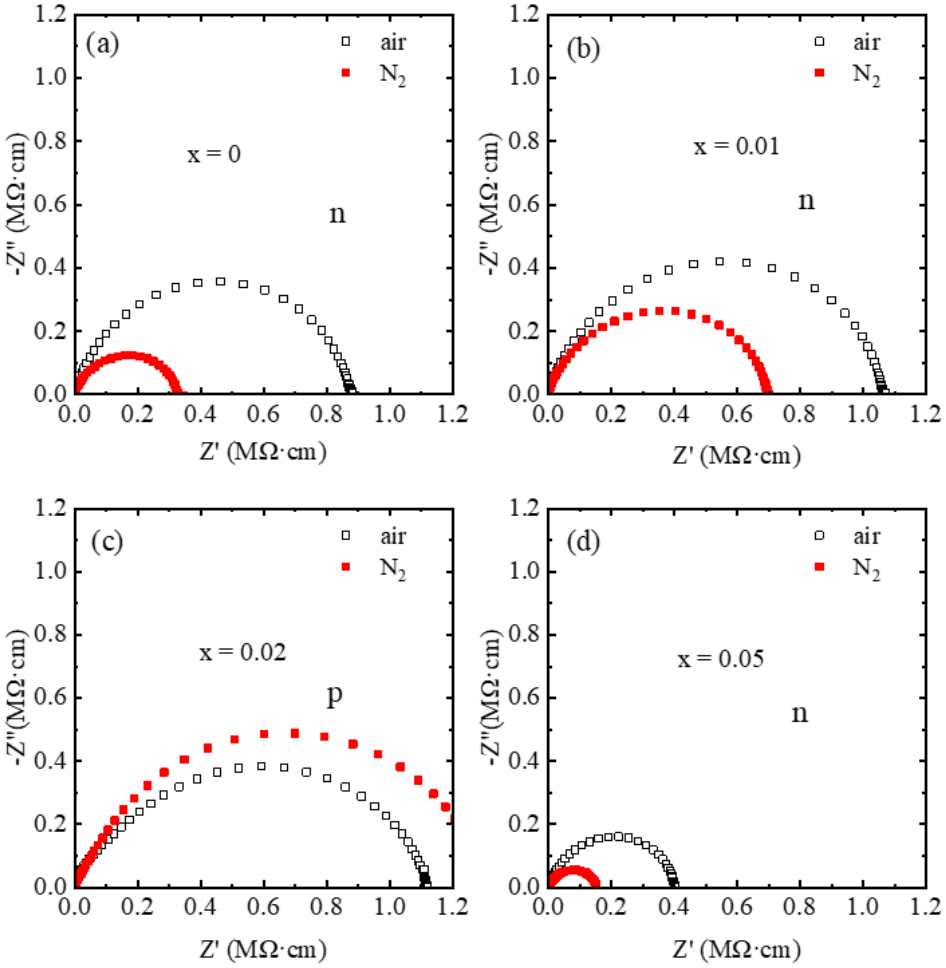

Fig. 4.23 Geometric factor corrected Impedance complex plane plots for BTNN-100xMg with (a) x = 0, (b) x = 0.01, (c) x = 0.02, (d) x = 0.05 ceramics measured in air and nitrogen atmospheres at 550 °C.

The effect of Mg^{2+} on the conduction mechanism of BTNN-100xMg ceramic is shown in Fig. 4.23. As the Mg^{2+} concentration increases, the conduction shifts from *n*- to *p*- then back to *n*-type for x = 0.05. The initial shift from *n* to *p* is due to acceptor doping on the B-site as x increases. A possible mechanism for the shift back to n is the excessive grain growth which limits the level of grain boundaries in the ceramic, which means there are fewer channels for oxygen to enter the samples during the cooling process post sintering. This would leave more oxygen vacancies for x = 0.05, which makes the sample *n*-type and more conductive. The total resistivity at 550 °C in air increases with x, then drops at x = 0.05, which may be due to an increase in the concentration of oxygen vacancies with acceptor doping.

For Nb^{5+} doped compositions, all samples remain n type (Fig. 4.24). Doping was carried out assuming ionic compensation, $Nb^{5+} \equiv 5/4Ti^{4+}$, resulting in V_{Ti}'''' n type conduction is expected to be retained as a function of y. However, Figure 4.24 illustrates that the conductivity increases as a function of x implying either an increase in the concentration of charge carriers or their mobility. Electronic compensation may play a part in increasing the conductivity.

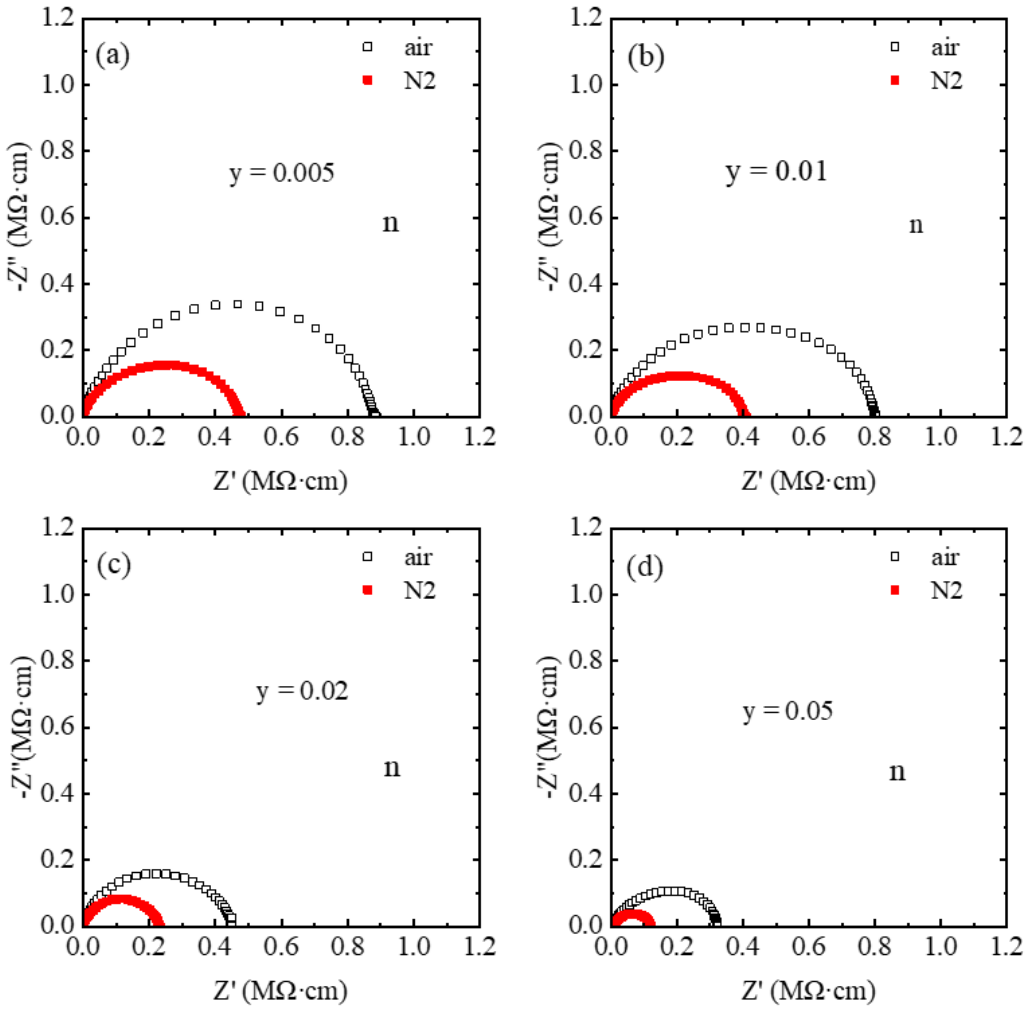

Fig. 4.24 Geometric factor corrected Impedance complex plane plot of BTNN-100yNb with (a) y = 0.005, (b) y = 0.01, (c) y = 0.02, (d) y = 0.05 ceramics measured in air and nitrogen atmospheres at 550 °C.

To investigate the electrical microstructure of the BTNN-100xMg ceramics, impedance data were collected on samples between 450 and 650 °C. The contribution of different components could be distinguished by analysing the frequency spectra of the imaginary part of impedance (Z″) and imaginary part of the modulus (M″), as shown in Fig. 4.25(a) and Fig. 4.25(b). It is clear from Fig. 4.25(b) that the M″ peaks of $x \leqslant 0.01$ are broad, consisting of at least two Debye peaks with very similar peak frequencies, which makes it difficult to identify the contributions from individual electrical components. However, the M” peaks begin to split at higher dopant levels. Peak frequencies differ by at least two orders of magnitude, providing an opportunity for more detailed analysis. Thus, data from x = 0.02 is selected to illustrate how the electrical microstructure of these ceramics may be resolved from their impedance responses. The capacitances of the electrical components of x = 0.02 are extracted from the M” peaks as shown in Fig. 4.25(c), and their Curie-Weiss behaviour is fitted in Fig. 4.25(d).

To distinguish the response between grain and grain boundary in x = 0.02, the temperature dependence of the capacitance of the low frequency and high frequency component is evaluated. The R_1-C_1 and R_2-C_2 parallel circuits are assigned to represent the low frequency and high frequency component shown in the impedance data, respectively. For impedance data of an ideal R-C circuit, the capacitance C could be extracted from peak values in Z”-f spectrum by the relation: ωRC = 1. The M” measured at this frequency would also meet the condition of: 2M” = C. As shown in Fig. 4.25(c), the capacitance of the low frequency component extracted from the Z” value is about one third larger than the capacitance extracted from the M” value at the peak frequency (f_{max}) for x = 0.02. This is due to overlapping of high and low frequency peaks, which means the measured peak values are a mixed response of the two R-C components. As a result, the R_1 and C_1 extracted from the measured peak value deviate from the ideal peak condition of $\omega R_1C_1 = 1$. For consistency, the capacitance presented in Fig. 4.25(d) are all extracted from the M” peaks. It is clear from Fig. 4.25(d) that both the high and low frequency components for x = 0.02 follow the Curie-Weiss relation. Combined with the SEM (Fig. 4.19) and the capacitance values shown in M"-f spectrum (Fig. 4.25(b)), these bulk components are most likely to be the core and shell regions in the grain of the ceramic, whereas the grain boundary response of the ceramic could not be separately identified from the M” or Z” peaks. It should also be noted that the core-shell mentioned here is resolved from the electrical impedance data, thus is the electrical core-shell structure, which may not directly represent the state of the compositional core-shell. As Fig. 4.25(d) suggests, the Curie-Weiss temperature of the core is close to the dielectric peak temperature shown in Fig. 4.21, whereas there is no significant dielectric anomaly shown near the Curie-Weiss temperature of the shell. This proves that the small signal dielectric response for x = 0.02 at 1kHz - 1MHz is dominated by the core regions of the grains.

In summary, the C_1-R_1 component is likely to be the response of shell/grain boundary (gb) since it depicts a narrower region in the ceramic than core component. This region demonstrates a weaker permittivity-temperature response which could not be explicitly distinguished in the LCR data shown in Fig. 4.21.

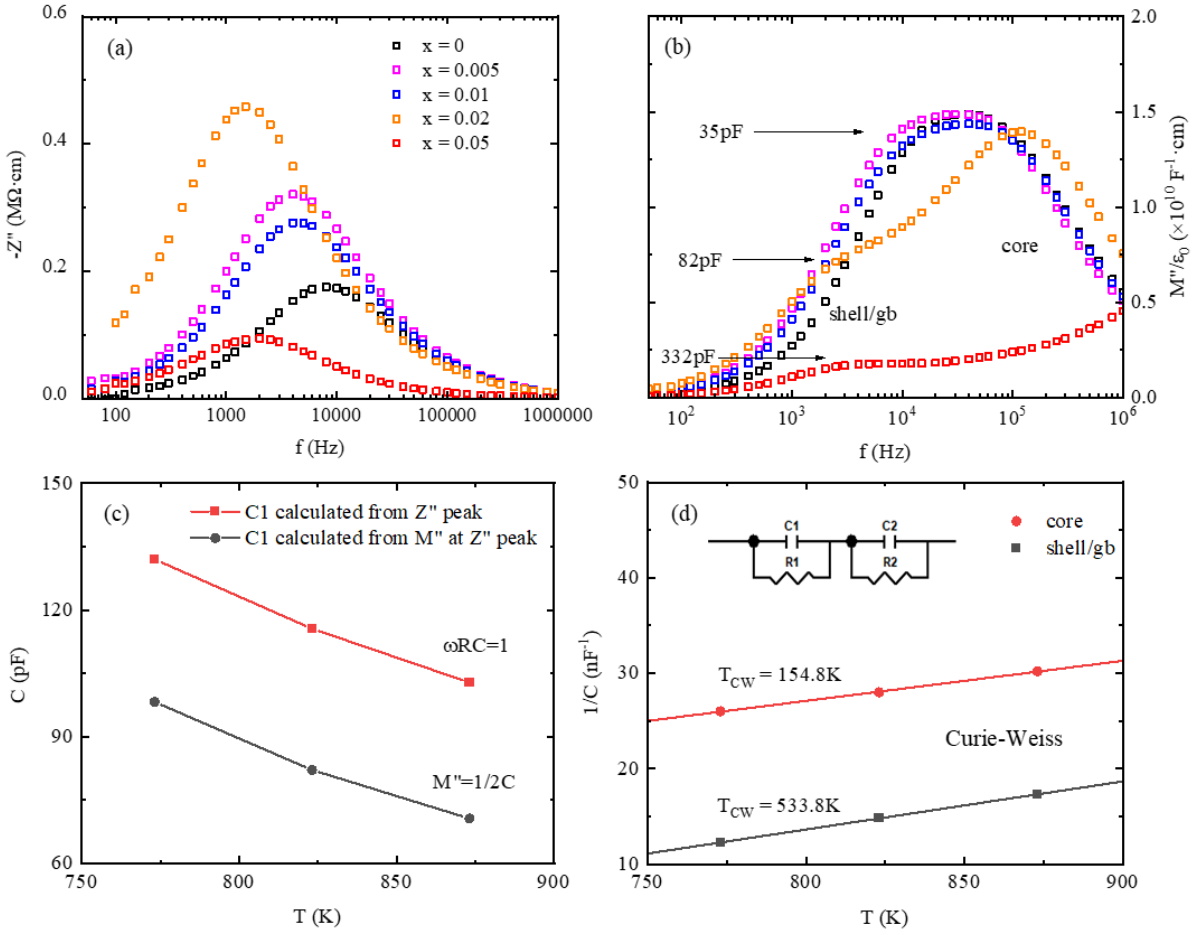

Fig. 4.25 The frequency dependence of (a) Z" and (b) M" of BTNN-100xMg ceramics at 550 °C. (c) The capacitance of shell in the grain of xMg = 0.02 extracted from the Z" values and M" values, respectively. (d) The Curie-Weiss fitting of the capacitance of core and shell/gb component, with the equivalent circuit and Curie-Weiss temperature marked in the graph.

From Fig. 4.25, we conclude that an electrical core-shell structure is shown in the impedance spectra of BTNN-100xMg ceramics. At low dopant levels, the core and shell regions share a similar capacitance of ~35 pF/cm (as corrected for overall sample geometry), and a similar f_{max} at 10 - 100 kHz. For x > 0.01, the grains grow significantly, and the resistance of the shell becomes much larger than that of the core, which separates the characteristic frequency, allowing a more detailed analysis of those regions. f_{max} for the core component shifts to much higher frequency (off scale) with x increased to 0.05, indicating a significantly more conductive core region in the sample, which could be further investigated.

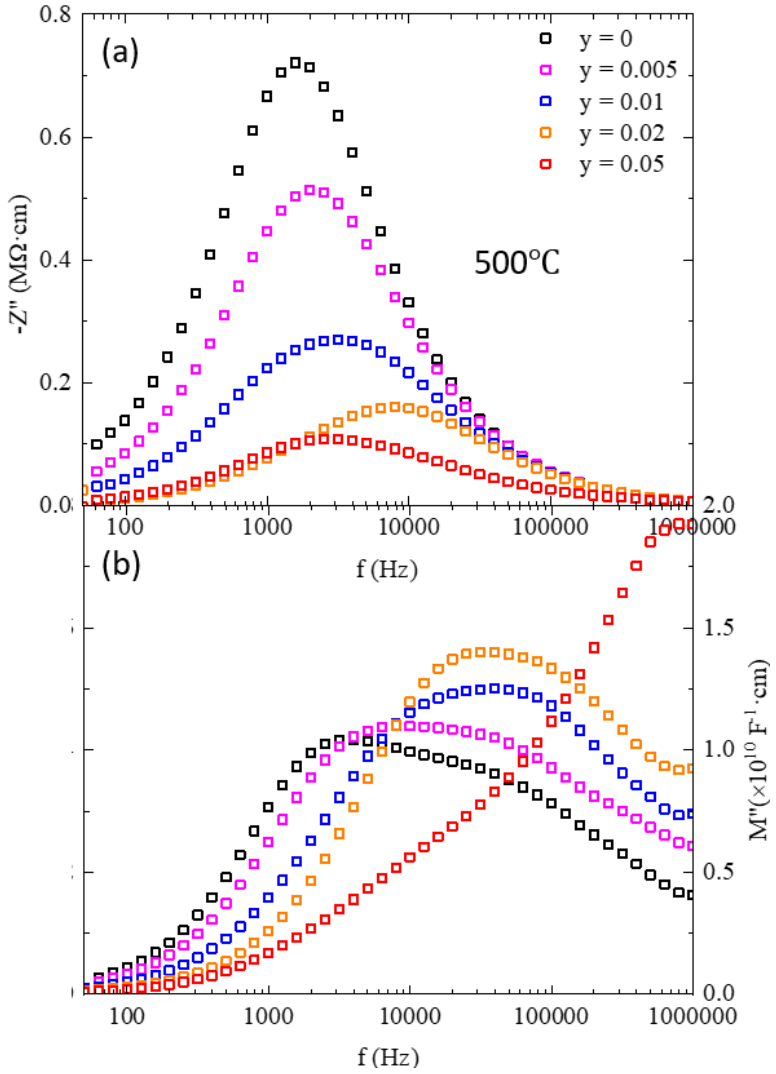

Fig. 4.26 The frequency dependence of (a) Z" and (b) M" of BTNN-100xNb ceramics at 500 °C.

As shown in Fig. 4.26, the M" peaks of Nb doped samples with y ≤ 0.02 are very broad, consisting at least two Debye peaks like that of BTNN-100xMg samples, which makes it difficult to assign the contributions to different regions in the sample. The full width at half maximum, FWHM is broader than 1.14 decades of frequency for all the peaks, indicating a non-ideal Debye behaviour which maybe a mixed response from different regions within ceramics that have similar impedance characteristics (R and C values). For y = 0.05, the peaks are split in the frequency spectrum, but are still quite broad and may each involve contributions from several regions of the sample. In analogy with the previous analyses on x = 0.02, the shoulder at ~ 10 kHz is primarily the shell/gb contribution with a capacitance of ~96 pF/cm. The high frequency component with a capacitance of ~26 pF/cm is the core/bulk contribution of the sample. The two components are not separated as clearly as in BTNN-100xMg samples, which is also consistent with the SEM images (Fig. 4.20) where no significant grain growth is detected.

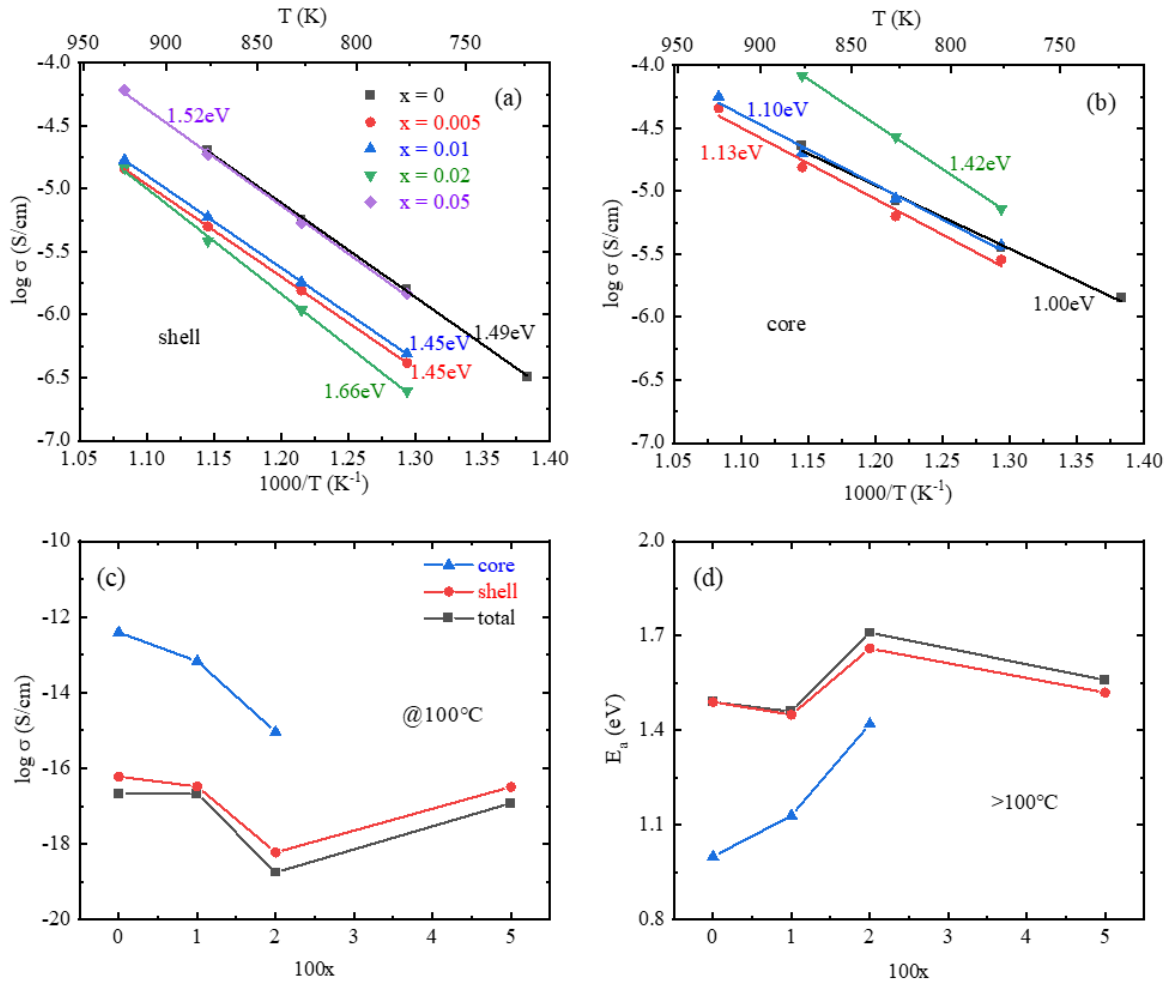

Fig. 4.27. Arrhenius plot of the (a) shell and (b) core components of the BTNN-100xMg ceramics, with the corresponding activation energy labelled near the fitted line. (c) Extrapolated log conductivity (log σ) at 100 °C and, (d) activation energy >100 °C, for the different components for BTNN-100xMg ceramics derived from conductivity Arrhenius plots.

The conductivity and activation energy of the charge carriers in the ceramic and the core-shell components correspond to the response of R_1 and R_2 in the equivalent circuit, respectively. As indicated in Fig. 4.27(a) and .27(b), the shell components have, overall, a lower conductivity and higher activation energy than the core components. When comparing Fig. 4.27(a) and 4.27(b) with Fig. 4.28, it is evident that the resistive response of the ceramics is dominated by the shell component. Since no dielectric anomaly was detected in the dielectric temperature spectrum above ~100 °C, an extrapolation of Arrhenius plot was performed to deduct the conductivity closer to room temperature. As shown in Fig. 4.27(c) and 4.27(d), x = 0.02 have the most resistive shell component and highest activation energy for both the core and shell components, which potentially improves the BDS under applied field. However, this is not the case with the P-E measurement of the samples. This may be due to the grain growth which increased the volume fraction of the electrically more conductive core regions, based on M”-f spectra.

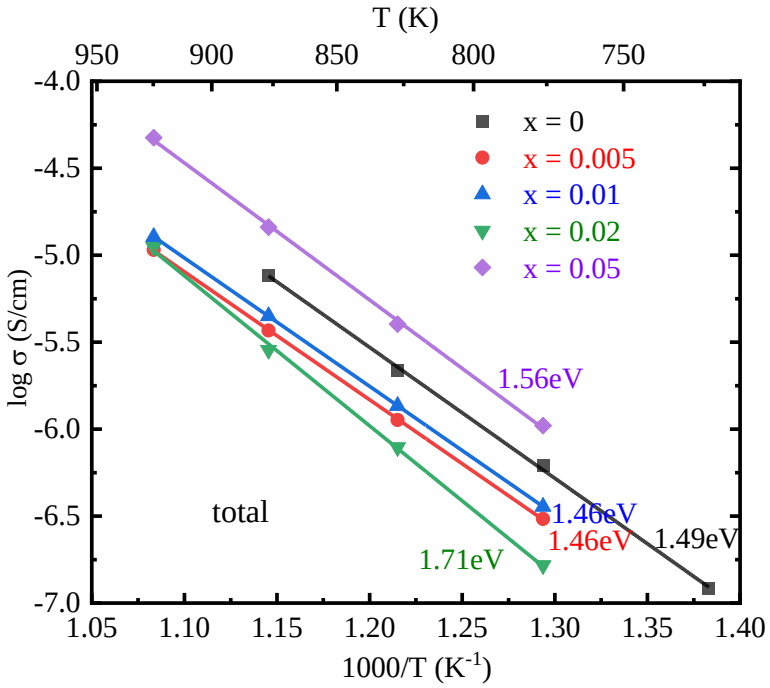

Fig. 4.28 Arrhenius plots of total electrical conductivity for BTNN-100xMg ceramics with the activation energy labelled on the fitted lines, respectively.

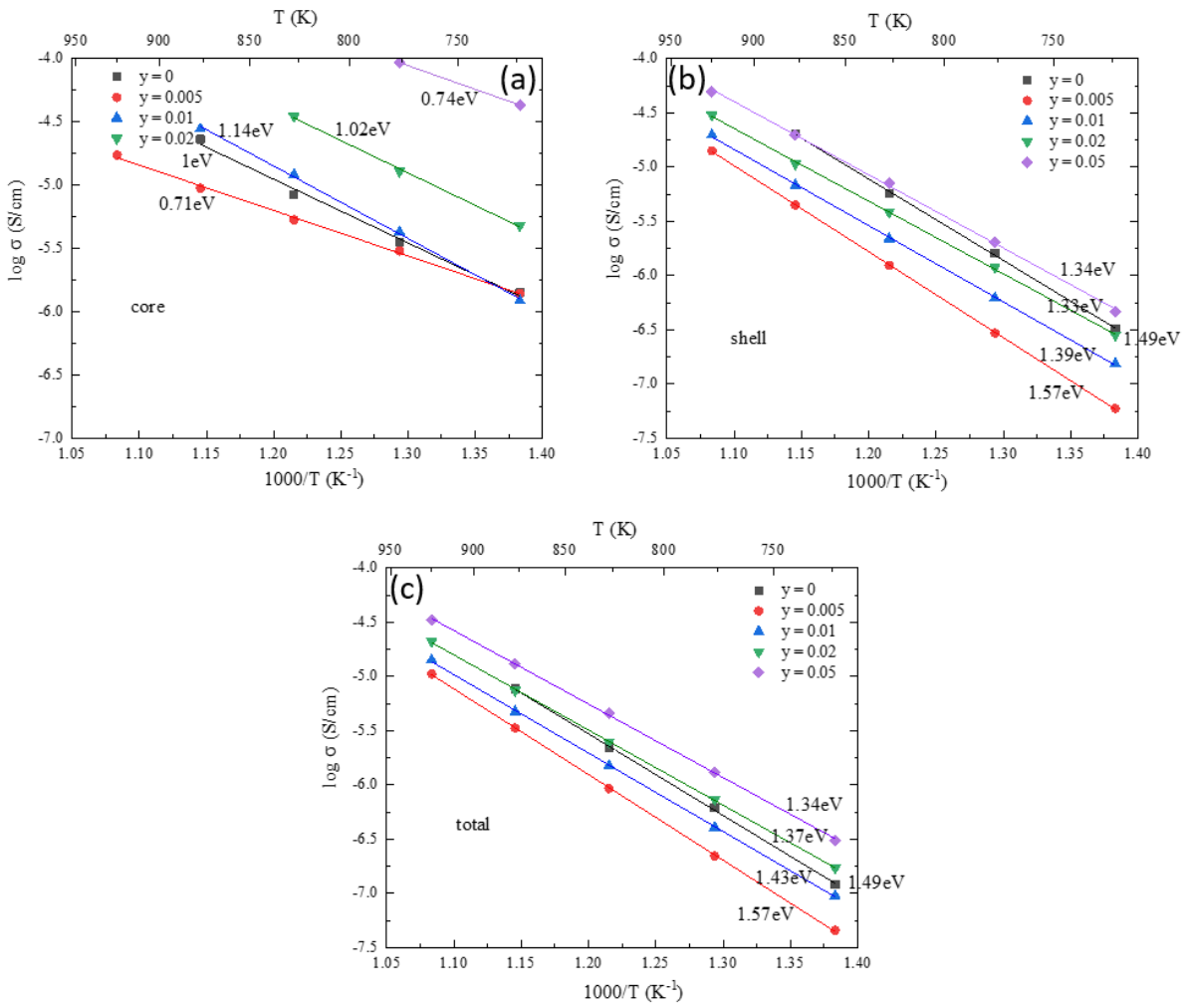

Fig. 4.29 Arrhenius plot of the (a) bulk, (b) grain boundary components and (c) total conductivity of the BTNN-100yNb ceramics, with the corresponding activation energy labelled near the fitted line.

From the Arrhenius plot of BTNN-100yNb ceramic, the low frequency shell component has a very similar conductivity and activation energy as the ceramic samples in total. This proves that the shell component dominates conduction. The more conductive core component of BTNN-100yNb ceramic generally have a lower activation energy than the shell component. Overall, the activation energy and conductivity of BTNN-100yNb decrease with increasing y, which is consistent with the increasing loss observed in the permittivity-temperature spectra.

4.4.3 High Field Performance

The spontaneous polarisation of BTNN-100xMg ceramics decrease with increasing dopant level, as shown in Fig. 4.17(d). This trend could also be observed in the P-E loops shown in Fig. 4.30(a), with polarisation measured at 380 kV/cm decreasing from ~28 to ~ 24 μC/cm^2 for x = 0.00 to 0.02. However, the measured polarisation value is significantly larger than the

calculated spontaneous polarisation (~5 μC/cm^2). A difference in maximum polarisation measured in P-E loops and spontaneous polarisation often occurs in the case for relaxor materials. A crossover from dielectric to semiconductor behaviour occurs for x > 0.02. As shown in Fig. 4.31, the I-V curve of Au-5Mg-Au device is typical for a double Schottky barrier device. [190]

In BTNN-100xMg ceramics, the optimum energy storage performance was achieved for x = 0.01, which has W_{rec} = 3.4 J/cm^3 with η of 82.6% at 400 kV/cm. As shown in Fig. 4.30 (b), E_{max} and energy storage density of the samples increased, whereas the efficiency of energy storage dropped with increasing dopant concentration. The enhanced energy storage performance may be associated with a more resistive core region with elevated activation energy. Additionally, x = 0.01 shows a broad plateau in permittivity as a function of temperature.

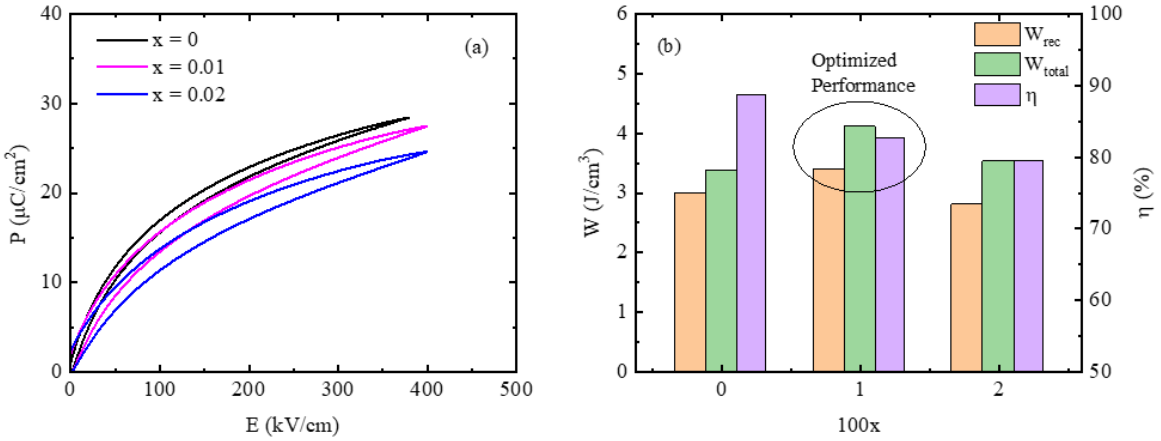

Fig. 4.30. (a) Polarisation versus electric field for BTNN-100xMg ceramics at room temperature. (b) The dependence of energy storage performance (W_{rec}, W_{total}, η) on dopant level.

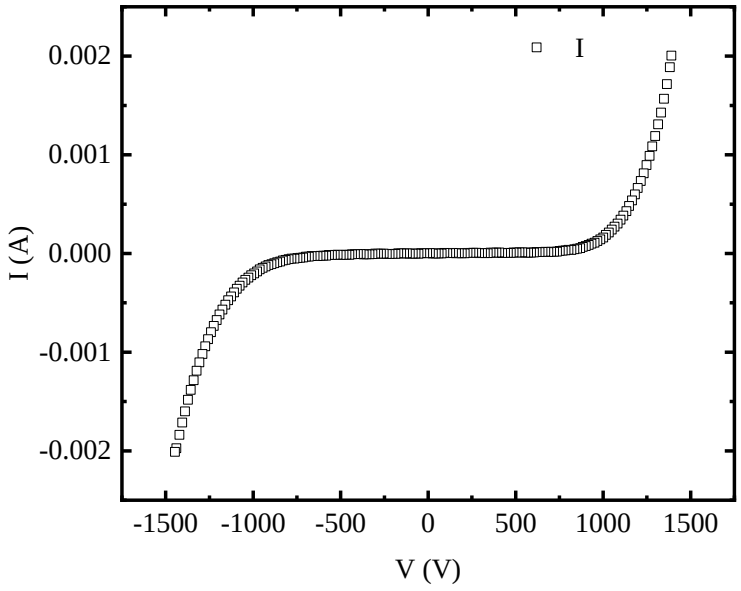

Fig.4.31 I-V curve for an Au/x = 0.05/Au device measured at room temperature, with a distance between two electrodes of $3.3*10^5$ nm.

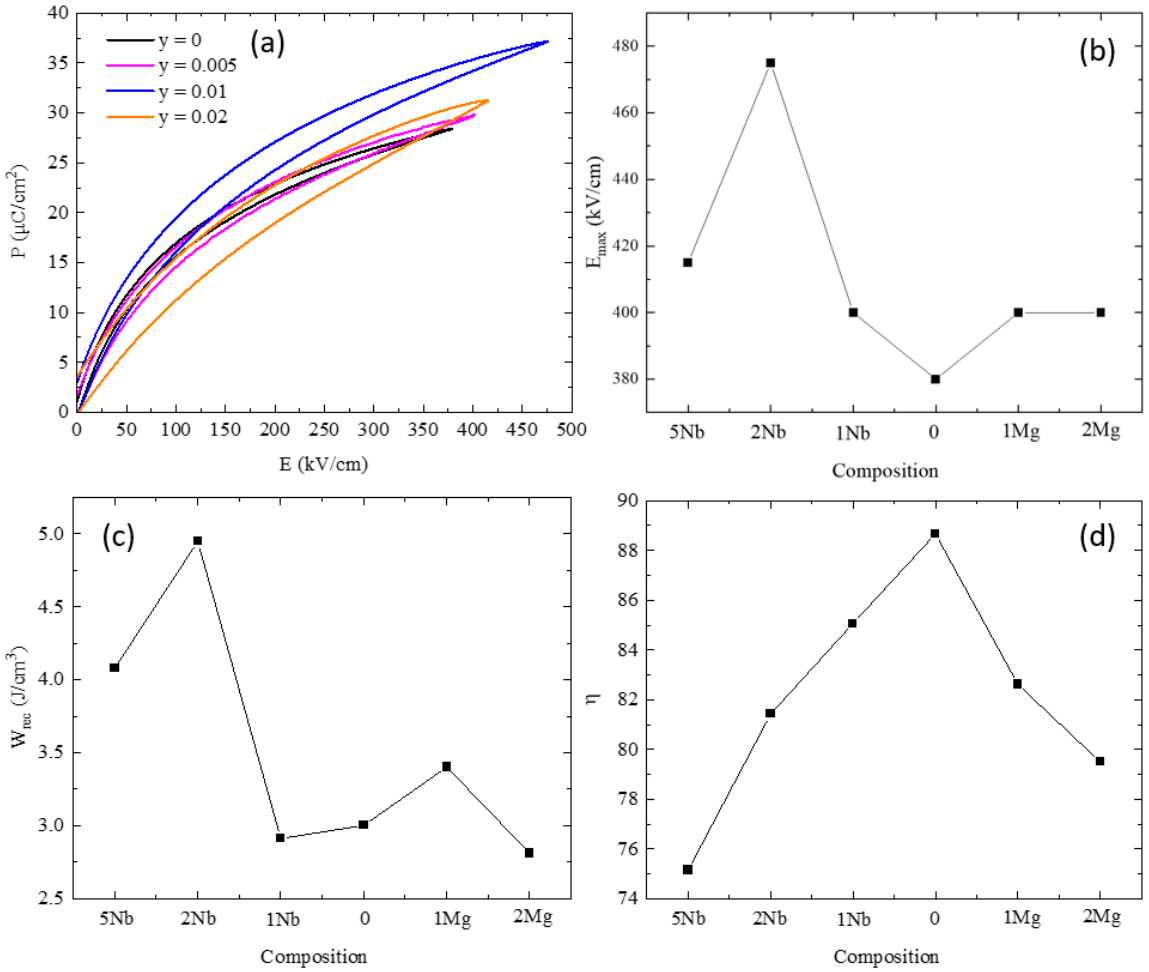

Fig. 4.32 (a) Polarisation versus electric field for BTNN-100yNb ceramics at room temperature. (b) Maximum applied AC unipolar electric field (E_{max}), (c) recoverable energy density (W_{rec}), and (d) energy storage efficiency (η) at 1 Hz for BTNN-100xMg and BTNN-100yNb ceramics.

The unipolar P-E loops of xNb compositions are shown in Fig. 4.32(a). Polarisation increases slightly with increasing x, which is inconsistent with the permittivity-temperature spectrum result. This may be due to extra contributions towards polarisation from defects in xNb at the lower frequency of 1 Hz used for P-E loop measurements. Although the permittivity-temperature spectrum is taken at 100 kHz, the increasing loss at high temperature with x indicates either an increasing number of defects or more likely their greater mobility.

The energy storage performance of BTNN-100xMg and BTNN-100yNb compositions (E_{max}, W_{rec} and η) are shown in Fig. 4.32(b)(c)(d). The highest AC BDS of 475 kV/cm and W_{rec} of 4.95 J/cm^3 are achieved in y = 0.02, with a η of 81%. The highest η is achieved in BT10NN, with W_{rec} of 3 J/cm^3 and η of 89%.

4.4.4 Summary

This chapter focuses on Mg and Nb-doped BT10NN ceramics. In Mg-doped samples, the dopant was observed to transition from the A site to the B site as concentrations increased ($x \geqslant 0.02$), resulting in a merging of the permittivity-temperature spectra plateau into a single peak. This transition correlated with significant grain growth and the emergence of an electrical core-shell response in impedance spectra. Conversely, Nb exclusively substituted on the B-site, leading to a movement of the permittivity-temperature spectra plateau to lower temperatures with increasing dopant concentration. However, the core-shell response was less distinct in the frequency spectrum of M" and Z". Mg doping at x = 0.02 exhibited the lowest resistivity and highest activation energy, indicating a shift in conduction mechanism from n- to p-type and back to n-type. For Nb-doped compositions, activation energy and resistivity decreased with increasing dopant level, while the conduction mechanism remained n-type. Regarding energy storage performance, Mg doping reduced polarization but enhanced the BDS of the ceramic. In contrast, Nb doping increased polarization and W_{rec}, with y = 0.02 demonstrating the highest W_{rec} of 4.95 J/cm3 and an efficiency (η) of 81%.

4.5 (1-x)$NaNbO_3$-x$BaTiO_3$ (0.0≤x≤0.25) ceramics

$NaNbO_3$ is a perovskite which undergoes several phase transitions from -100 to 640 °C. [16] At room temperature it is dominantly in the antiferroelectric, P phase (Pbam) but there are almost always trace amounts of the ferroelectric Q phase ($Pmc2_1$) which has a similar free energy. [18] At high temperature it transforms to the R phase. The temperature stability of permittivity is ideal for practical dielectric applications. [18] However, $NaNbO_3$ has recently been reported to have a high oxygen ion conductivity which requires optimization for dielectric applications. [191] In this chapter, (1-x)$NaNbO_3$-x$BaTiO_3$ (NN100xBT) solid solution is explored in order to investigate the structure and electrical characteristics of the NN rich end of the solid solution.

4.5.1 Phase Assemblage and Microstructure

XRD pattern of NN100xBT ceramics are shown in Fig. 4.33. With increasing BT content, the structure shift from orthorhombic to tetragonal with a secondary phase of $Ba_3Nb_4Ti_4O_{21}$ which emerges in samples with x ≥ 0.15.

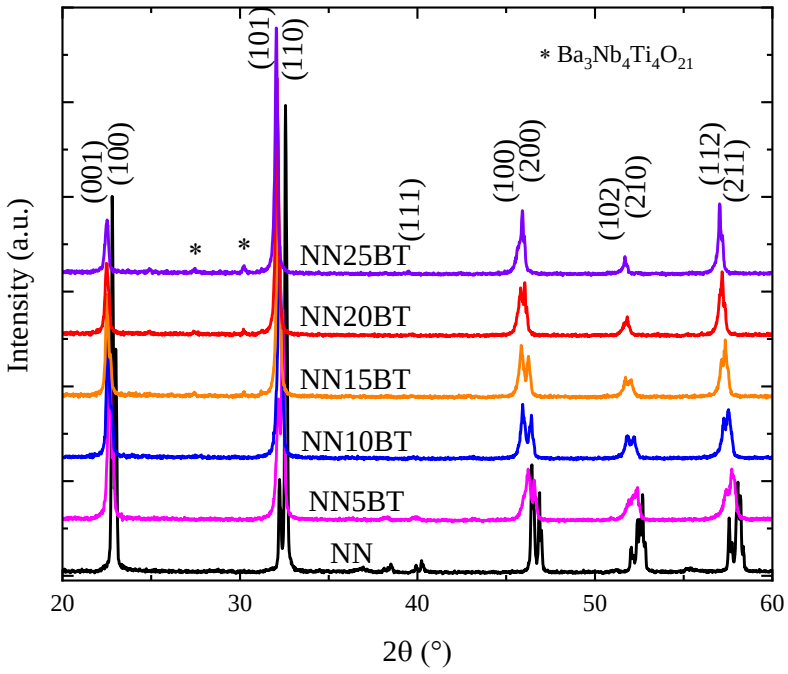

Fig. 4.33 XRD patterns of NNxBT (0.0≤x≤0.25) ceramics.

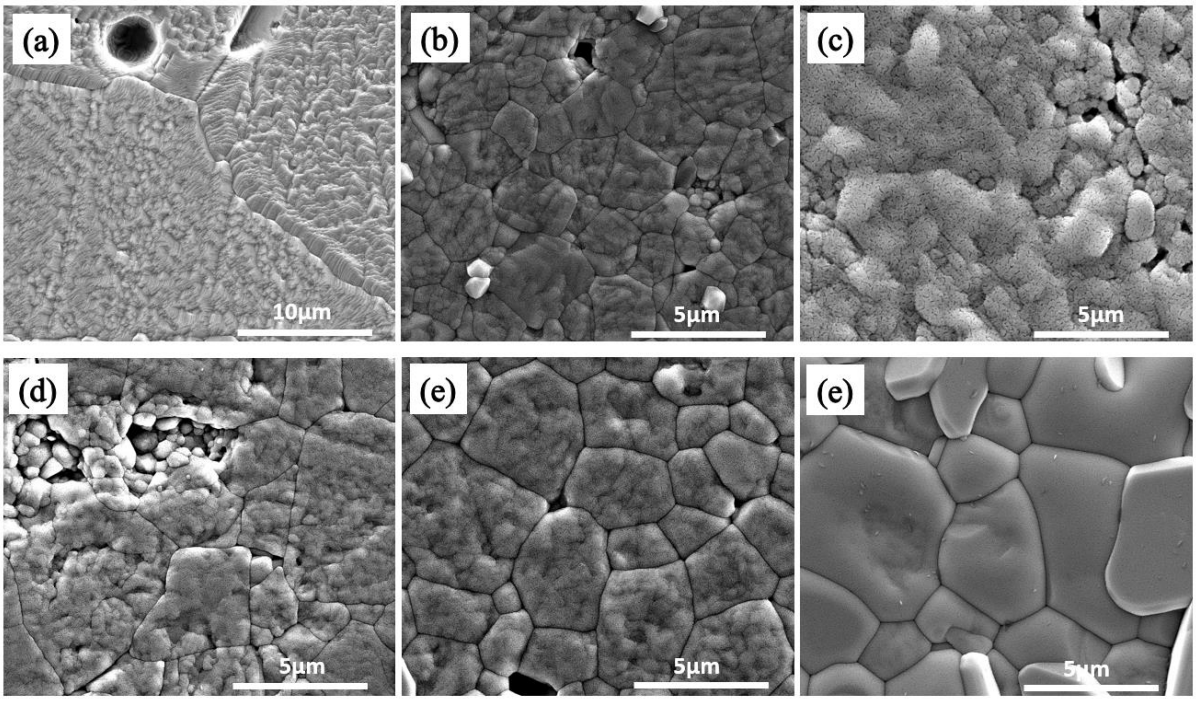

Fig. 4.34 SEM images of thermally etched polished surfaces of (a) NN, (b) NN5BT, (c) NN10BT, (d) NN15BT, (e) NN20BT, (f) NN25BT ceramics.

SEM images of NN100xBT ceramics shown in Fig 4.34 indicate the change in grain morphology with increasing BT. For undoped NN, the grains are quite large, on the scale of dozens of microns. For ceramics with $x \leq 0.2$, both small submicron grains and grains around 5 µm or larger are present, suggesting a bimodal distribution. NN25BT sample however, shows a monomodal grain size distribution ~ 3 - 6 µm diameter.

4.5.2 Low Field Dielectric and Conduction Behaviour

The permittivity-temperature spectra of NN100xBT ceramics are shown in Fig. 4.35. As x increases, the permittivity maximum (T_{max}) shifts from 385 °C to below room temperature, with the maximum ε_r increasing from 1142 to ~7500 with x increasing from 0 to 0.10, then decrease to ~6500 for x = 0.2. As x increase from 0 to 0.25, there is some degree of frequency dispersion of T_{max}, as shown in Fig. 4.36. However, the difference in T_{max} from 10 kHz to 250 kHz is only around 4 °C, smaller than most relaxors. Thus, the NN rich end of this solid solution has only weak relaxor characteristics and can be classed primarily as a system that exhibits essentially a broad ferroelectric response.

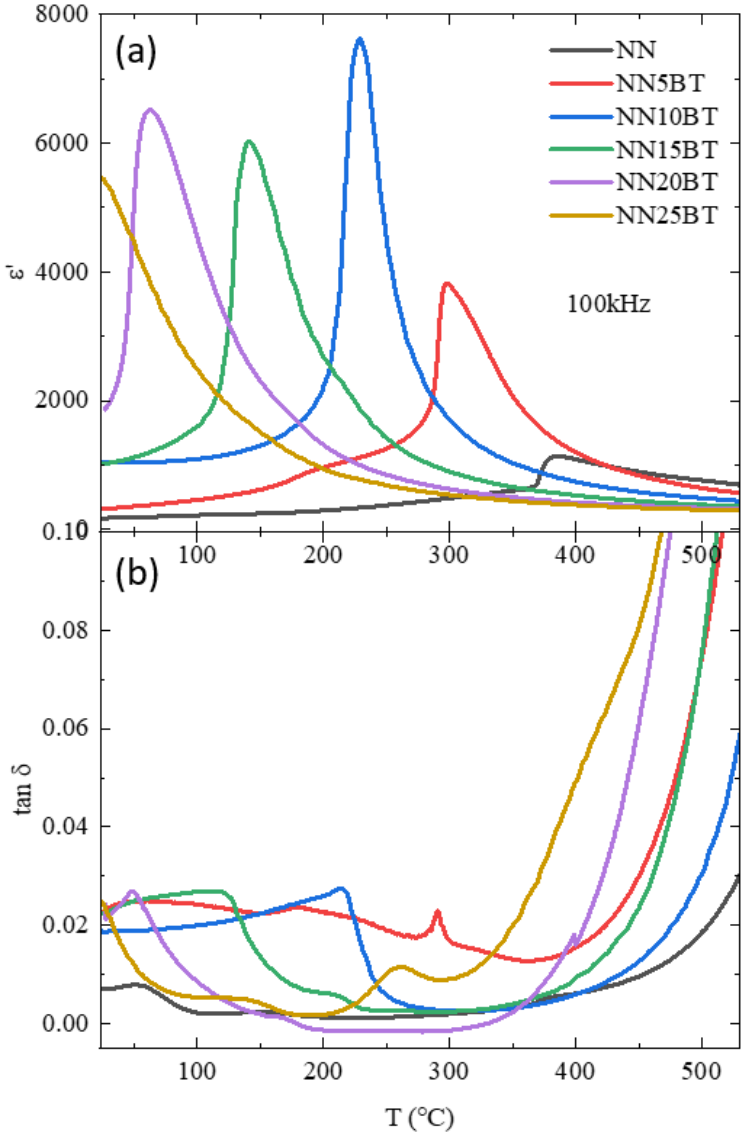

Fig. 4.35 Temperature dependence of (a) ε’ and (b) tan δ for NN100xBT ceramics at 100 kHz from 25 to 525 °C.

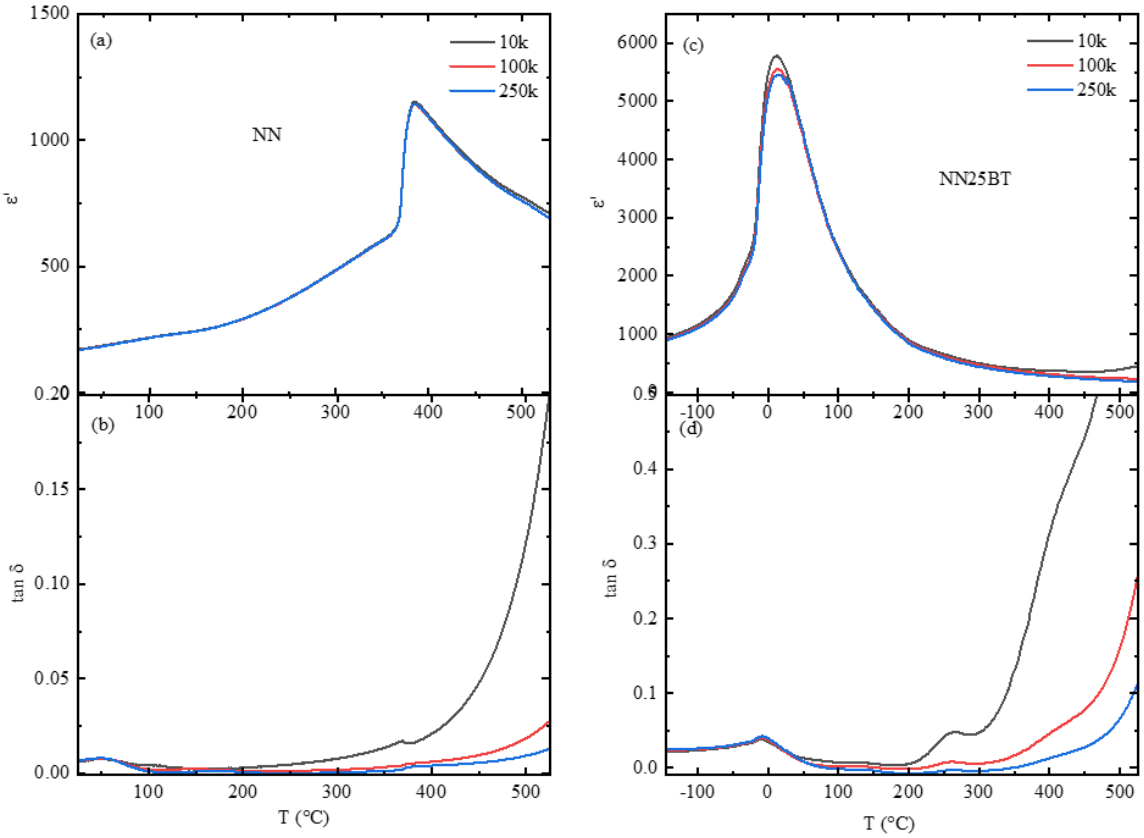

Fig. 4.36 Temperature dependence of (a) ε' and (b) tan δ for NN; (c) ε' and (d) tan δ for NN25BT ceramics at 10 K, 100 k and 250 kHz.

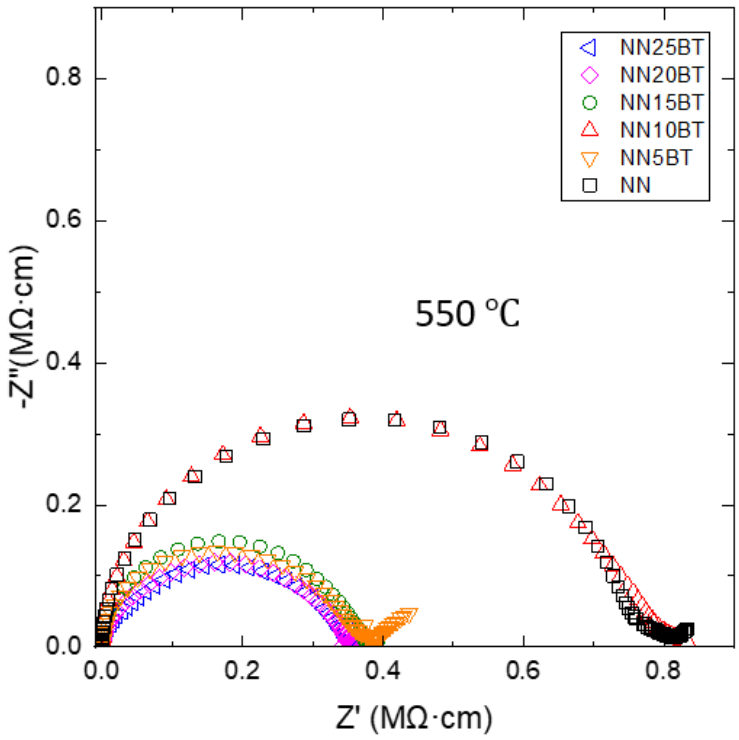

Fig. 4.37 Impedance complex plane plot of NN100xBT ceramics measured at 550 °C in air.

As shown in Fig. 4.37, Warburg impedance spike is present in the impedance response of NN and NN5BT ceramics, which indicate that ionic conduction may be contributing to the impedance response at 550 °C. A deviation from semicircle shown at the low frequency part of impedance of NN is likely to be due to transport phenomenon at the sample-electrode interface.

To investigate the level of oxygen ion conduction observed in the impedance measurement, Electromotive Force (EMF) measurement of oxygen ion transport was performed on NN100xBT ceramics. As shown in Fig. 4.38, the oxygen ion transport number (t_{ion}) of NN is higher than 0.3 at 800 °C. With increasing x, t_{ion} @ 800 °C decrease significantly to ~0.005 for NN15BT, shifting the ceramic from ionic conductor to a good dielectric material. Overall, t_{ion} increases with increasing temperature, but a reverse trend is seen in the NN10BT ceramics. The reversed trend may not represent the actual value of the t_{ion}, especially at lower temperatures, but arises from the decreased grain size and high porosity of the sample.

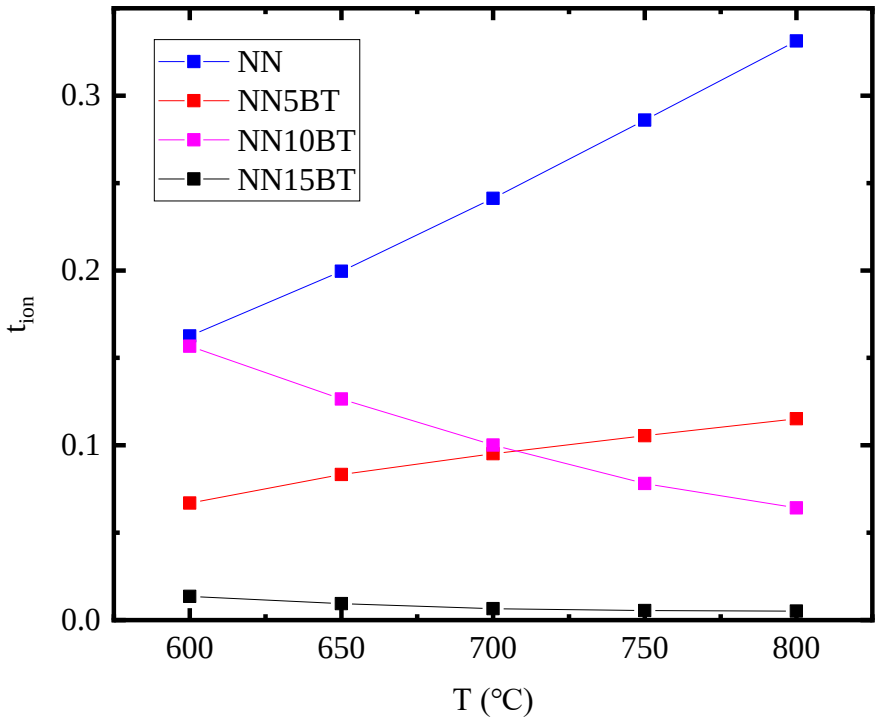

Fig. 4.38 Oxygen ion transport number (t_{ion}) of NN100xBT ceramics between 600 and 800 °C from EMF measurements using N_2 and air at the two electrodes.

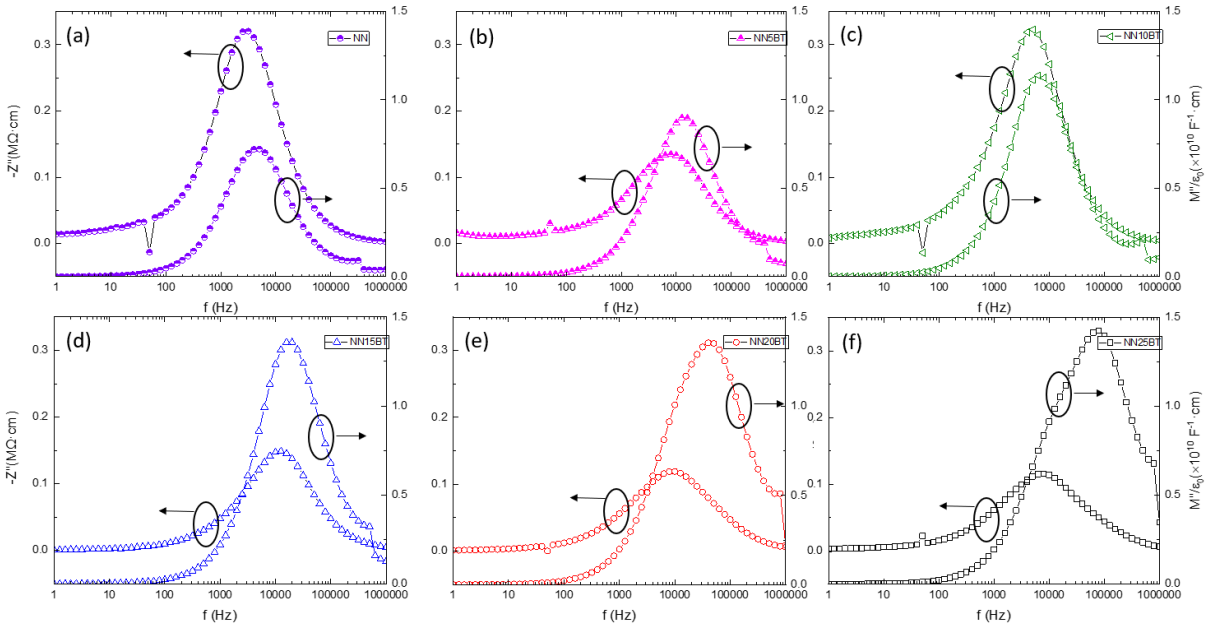

Fig. 4.39 The frequency dependence of Z" and M" of (a) NN, (b) NN5BT, (c) NN10BT, (d) NN15BT, (e) NN20BT, (f) NN25BT ceramics at 550 °C.

To investigate the electrical microstructure of NN100xBT ceramics, frequency spectra of M" and Z" are plotted in Fig. 4.39. Overall, the peak frequency of M" and Z" are close with each other, indicating a relatively more homogenous electrical microstructure compared with the BT-rich end of the solid solution in previous sections. With increasing x, the M" and Z" peak gradually separate, with different R and C values for different regions in the ceramics. For NN25BT, the capacitance value at Z" peak and M" peak are 60 pF/cm and 35 pF/cm, respectively, indicating they are likely to be both bulk components. With relatively high BT content, the components are possibly electrical core-shell structure.

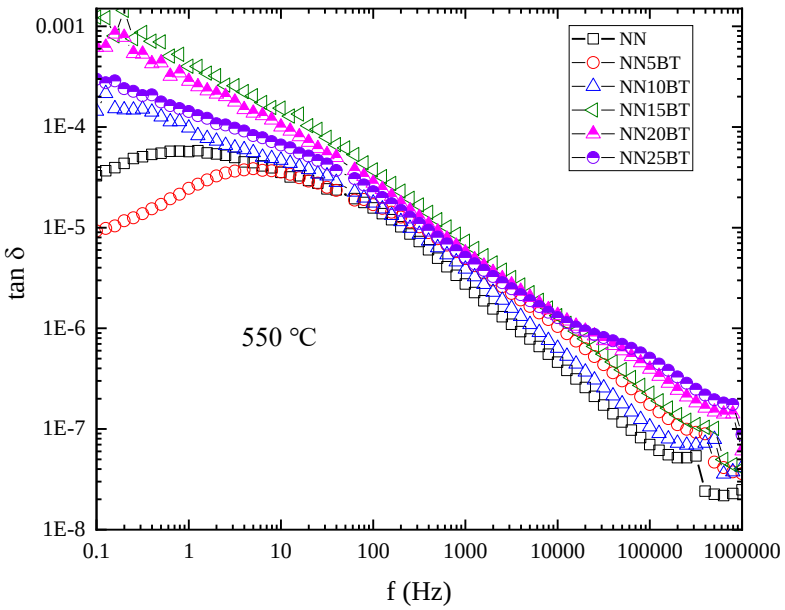

Fig. 4.40 The frequency dependence of loss tangent (tan δ) of NN100xBT ceramics at 550 °C.

Based on the frequency spectrum of tan δ (Fig. 4.40), it is reasonable to propose the following. At low frequencies with respect to tan δ, the positive gradients for NN and NN5BT indicate a response consistent with a series R-C component. With the high ionic conduction confirmed by EMF measurement, the R is likely to be the bulk ceramic contribution, and C is the double-layer capacitance at the ceramic-electrode interface. For NN20BT and NN25BT, the change in gradient at ~30 kHz indicates a second parallel R-C contribution in the ceramic sample, which agrees with the result observed in the frequency spectrum of M" and Z". Although the M" and Z" peak frequency of NN10BT and NN15BT does completely overlap, a second R-C element does not manifest in the tan δ vs f.

4.5.3 High Field Performance

The field dependent polarisation and current of BT100xNN ceramics are shown in Fig. 4.41. The antiferroelectric-ferroelectric phase transition field (E_{A-F}) of NN is higher than 80 kV/cm. Thus, the P-E loop of NN looks appears linear with some leakage current. By adding BT, a pinched hysteresis loop is obtained which may be interpreted as arising from an AFE-FE transition within part of the sample. However, such loops can also arise from unpinning of the domains from defect dipoles with the crystal lattice. Assuming however that the pinching arises from at least in part an AFE-FE transition, E_{A-F} is reduced to 60 kV/cm for NN5BT and 61 kV/cm for NN10BT, respectively. Saturation polarisation for NN5BT and NN10BT are 24.6 and 25.3 μC/cm^2, respectively. Both E_{A-F} and saturation polarisation increased but at x > 0.01, no antiferroelectric feature is seen in the ceramics. In the current-field loops (I-E loops), only a single peak is observed associated with switching micro- and eventually nano/meso domains as the loop becomes slimmer. As shown in Fig. 4.42, although the polarisation value under the same field decreases with increasing x from 0.1 to 0.25, the slimmer 'relaxor-like' loop increases the energy storage efficiency.

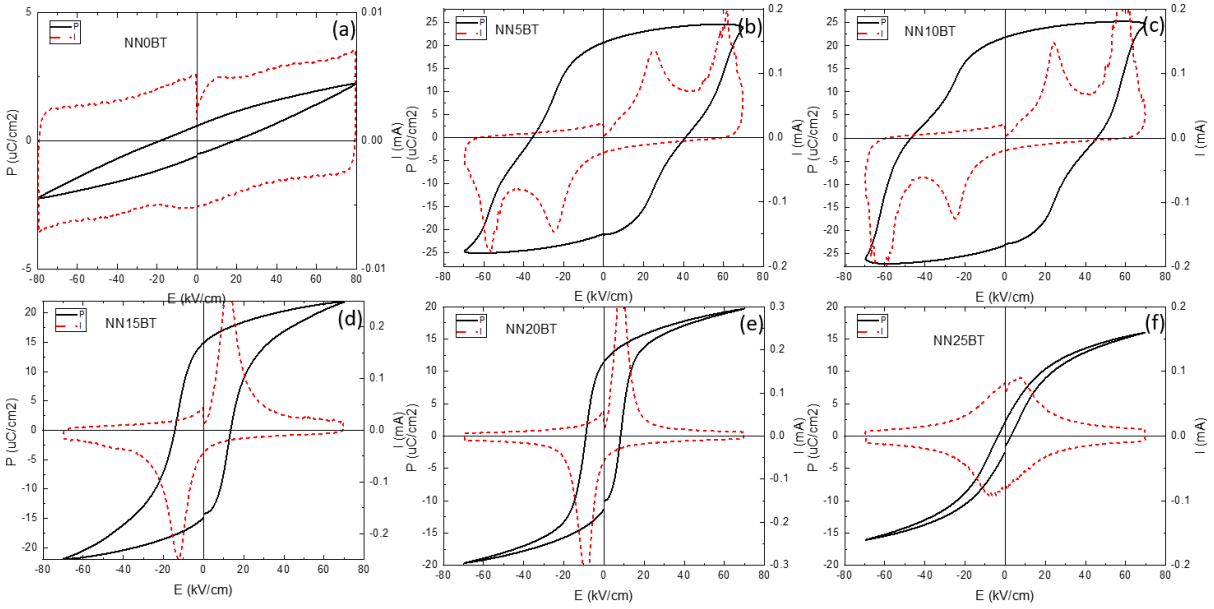

Fig. 4.41 Polarisation and leakage current versus electric field for (a) NN0BT, (b) NN5BT, (c) NN10BT, (d) NN15BT, (e) NN20BT, (f) NN25BT ceramics at room temperature.

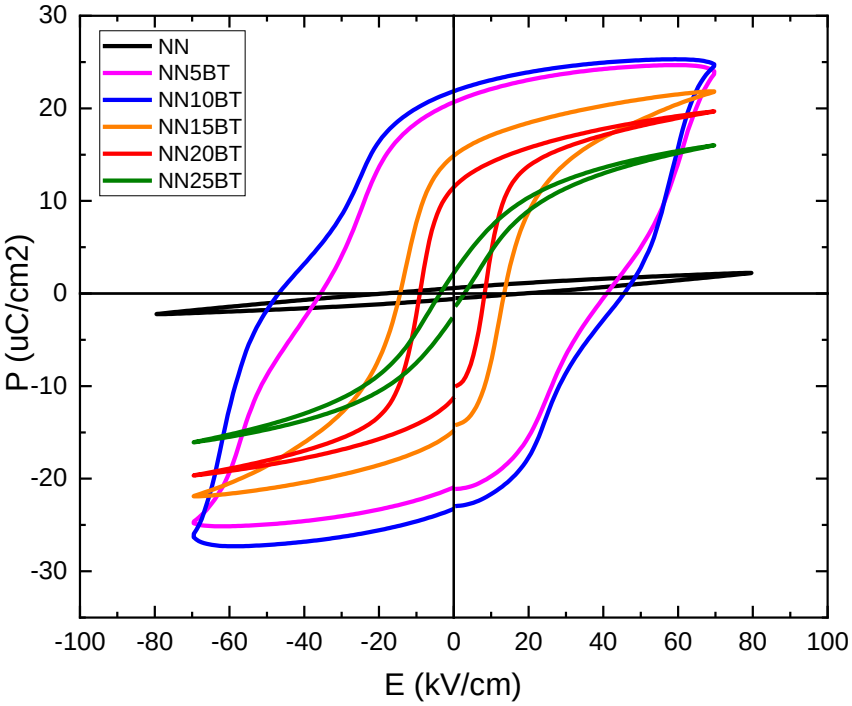

Fig. 4.42 P-E loops of NN100xBT ceramics at room temperature.

4.5.4 Summary

This chapter delves into the exploration of structural and electrical characteristics of BT100xNN ceramics (0.25 ⩾ x ⩾ 0.0). As x increases, the crystal structure undergoes a transition from orthorhombic to tetragonal. The grain size exhibits an initial decrease followed by an increase with rising x. T_{max} in the permittivity-temperature plots exhibits a decrease with increasing x, and even with x = 0.25, only a weak frequency dependency of T_{max} is observed. At 800 ℃, the oxygen ion transport number diminishes from > 0.3 to approximately 0.005 as x progresses from 0 to 0.15. This reduction in oxygen ion conductivity holds significance for dielectric capacitor applications. An analysis of the electrical microstructure reveals a high field polarisation response transitioning from antiferroelectric to ferroelectric and then to a weak relaxor-type behaviour with increasing x.

4.6 (0.85-x)$NaNbO_3$-0.15$BaTiO_3$-x$Nd(Mg_{2/3}Nb_{1/3})O_3$ and (0.75-x)$NaNbO_3$-0.25$BaTiO_3$-x$Nd(Mg_{2/3}Nb_{1/3})O_3$ ceramics

Based on section 4.5, NN15BT show the most homogeneous electrical microstructure with very low oxygen ion conductivity. NN25BT has a low T_{max} in permittivity-temperature spectrum and highest energy storage efficiency among NN100xBT composition. Thus, these two compositions were chosen for further optimization. Following principles describe by Lu et al, [35] a third end member, $Nd(Mg_{2/3}Nb_{1/3})O_3$, was introduced into the solid solution to further reduce polar coupling (loop becomes slimmer thereby increasing efficiency) and increasing the BDS of the ceramic.

4.6.1 Phase Assemblage and Microstructure

As shown in Fig. 4.43, NN15BT100xNMN and NN25BT100xNMN exhibits a dominantly pseudocubic crystal structure with x > 0.02. As x increases, the unit cell volume decrease and a secondary phase of $Ba_4Nb_2O_9$ is detected. At x = 0.1, the XRD peaks become asymmetric especially at high angles, indicating the presence of two perovskite crystal structure, suggesting either a retarded reaction or immiscibility.

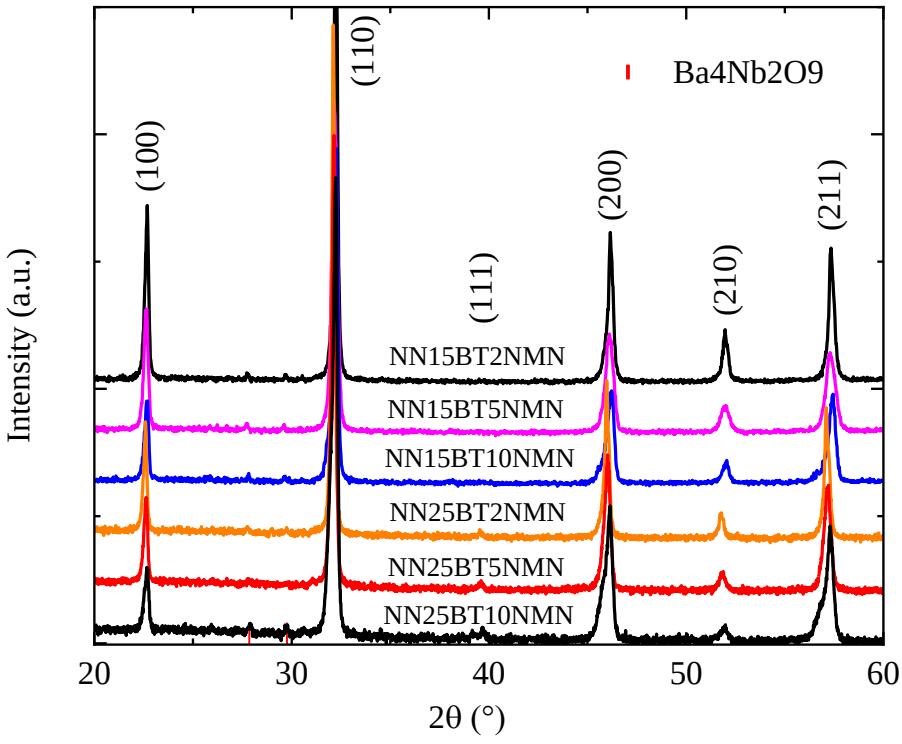

Fig. 4.43 XRD patterns of NN15BT100xNMN and NN25BT100xNMN ceramics sintered at 1320 °C.

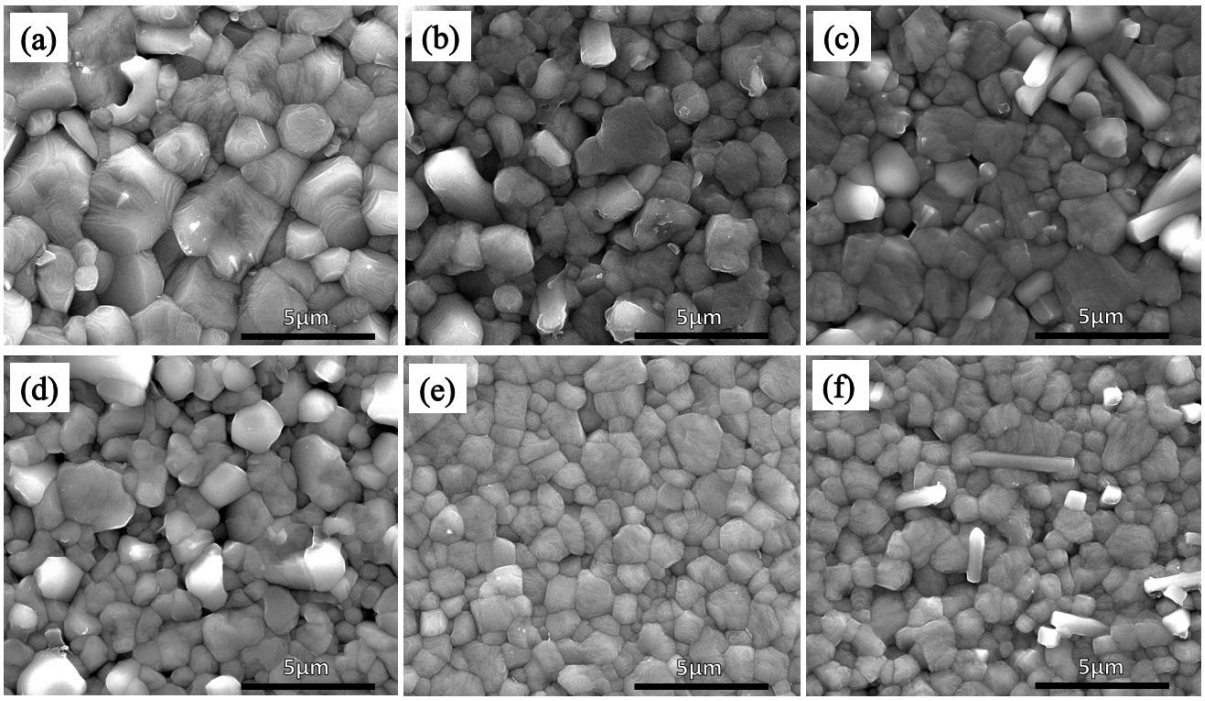

Fig. 4.44 SEM images of the thermally etched polished surface of (a) NN15BT2NMN, (b) NN15BT5NMN, (c) NN15BT10NMN, (d) NN25BT2NMN, (e) NN25BT5NMN (f) NN25BT10NMN ceramics.

Microstructure of the NN15BT100xNMN and NN25BT100xNMN ceramics are shown in Fig. 4.44. Grain sizes of 1-3 µm are common for the measured ceramics. For NN25BT5NMN ceramic, small and a more uniformed distribution of grain size of around 1 µm is present. The sintering temperature for compositions were optimised so a relative density of above 95% were achieved for all samples used in the structural, microstructural, and electrical measurements.

4.6.2 Low Field Dielectric and Conduction Behaviour

The permittivity-temperature spectra of NN15BT100xNMN and NN25BT100xNMN ceramics are shown in Fig. 4.45 and Fig. 4.46, respectively. The temperature of maximum permittivity decreases with increasing NMN content. As a result, the permittivity at room temperature generally decreases with increasing x. The permittivity moves from level of Class II dielectrics to between Class I and Class II dielectrics. The loss tangent is below 0.2 for NN15BT100xNMN from -125 to 500 ℃ and or NN25BT100xNMN composition, the loss tangent remains below 0.2 from -125 to 450 ℃.

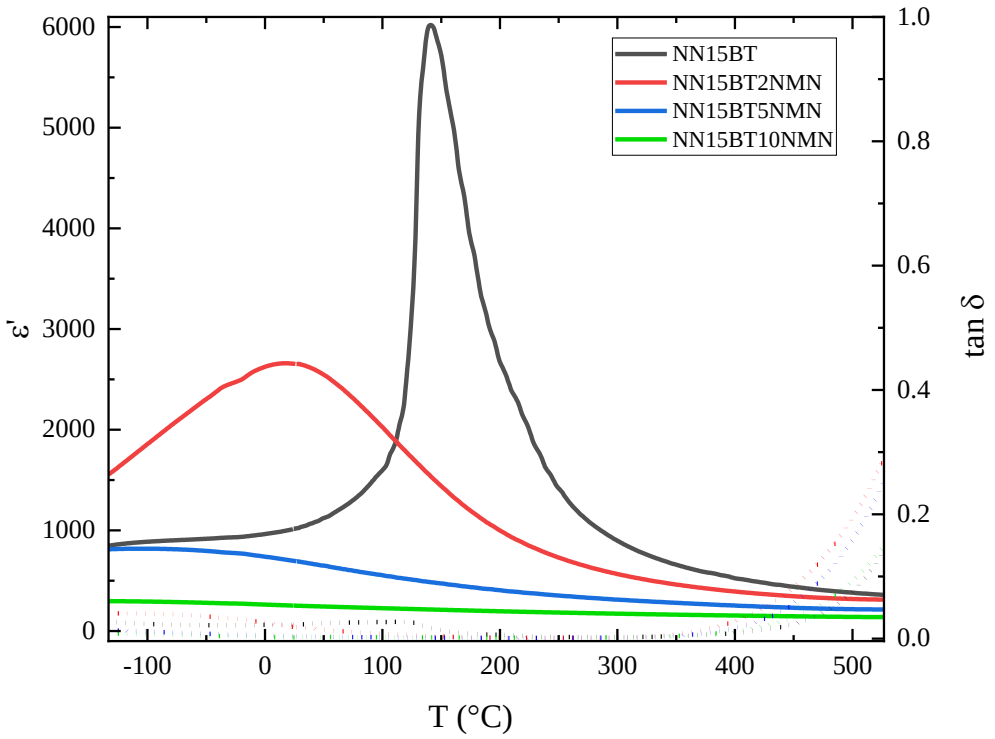

Fig. 4.45 Temperature dependence of ε’ and tan δ for NN15BT100xNMN ceramics at 100 kHz from -125 to 525 ℃.

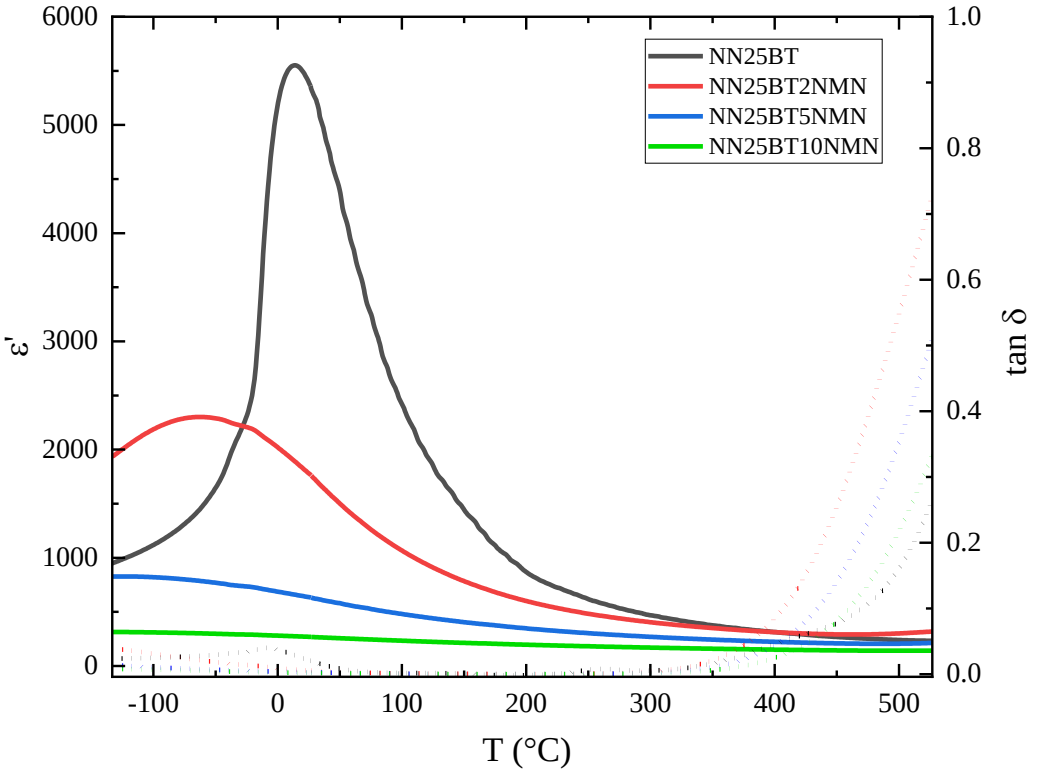

Fig. 4.46 Temperature dependence of ε' and tan δ for NN25BT100xNMN ceramics at 100 kHz from -125 to 525 ℃.

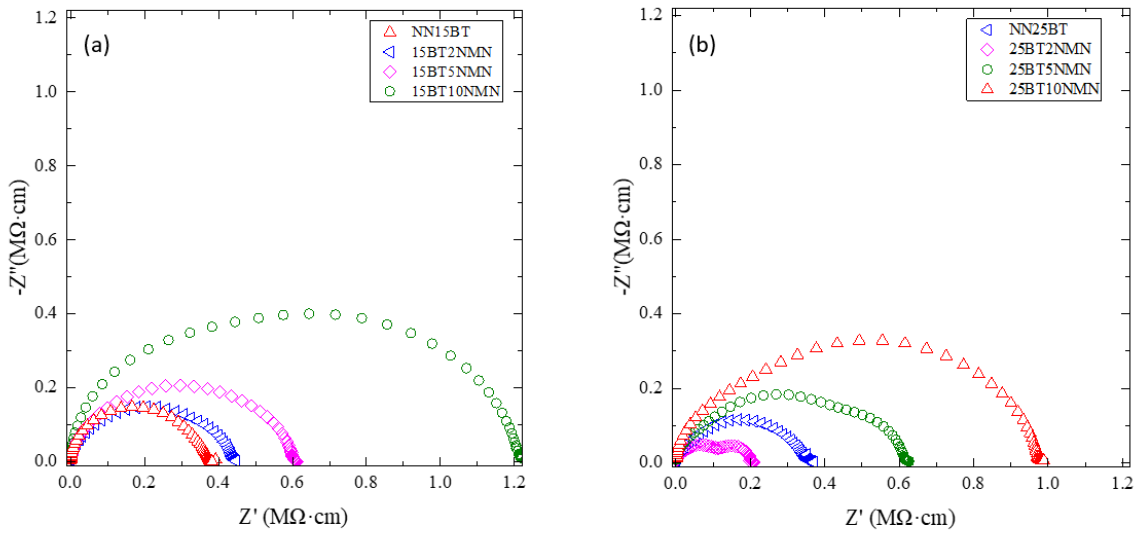

Fig. 4.47 Impedance complex plane plots for (a) NN15BT100xNMN and (b) NN25BT100xNMN ceramics measured at 550 ℃.

Impedance complex plane plot of NN15BT100xNMN and NN25BT100xNMN ceramics deviate quite far from semicircles. The level of deviation and impedance value measured at 550 °C both increase in NN15BT100xNMN with increasing NMN content. In NN25BT100xNMN, the semicircle is also not ideal, but the level of deviation is highest in NN25BT2NMN.

The frequency spectrum of M" and Z" for NN15BT100xNMN and NN25BT100xNMN are evaluated to investigate the electrical microstructure of the ceramics. For NN15BT100xNMN, the peak frequencies of M" and Z" separate more with NMN added, but the difference in peak frequencies are below one decade. The electrical microstructure is inhomogeneous, but the difference between the resistivity and capacitance of different regions of the ceramics are not significant based on the impedance data. For NN25BT100xNMN, the difference between peak frequencies is also larger with even for small amounts of NMN (2%) in the solid solution, two peaks are present in Z"-f spectra with different peak frequencies to the M" peak. With increasing x, the two peaks in Z" emerge into one broad peak, with around one decade of difference in peak frequency with the M" peak. The resistivity of the emerged Z" peak is about 3 times larger than the Z" peak value of NN25BT, indicating the formation of a different conduction pathway with the increasing NMN content. Overall, an inhomogeneous electrical microstructure is present for NN15BT100xNMN and NN25BT100xNMN ceramics.

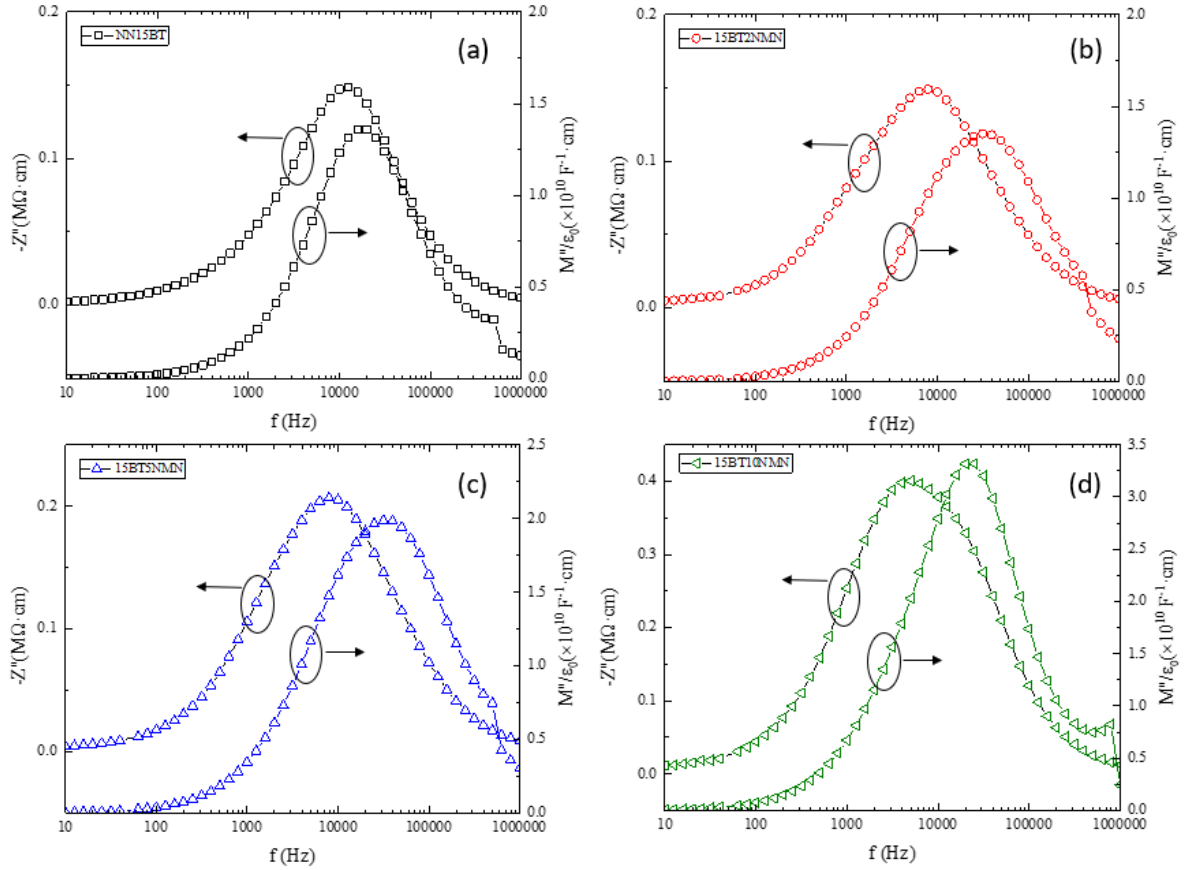

Fig. 4.48 The frequency dependence of Z" and M" of (a) NN15BT, (b) NN15BT2NMN, (c) NN15BT5NMN, (d) NN15BT10NMN ceramics at 550 °C.

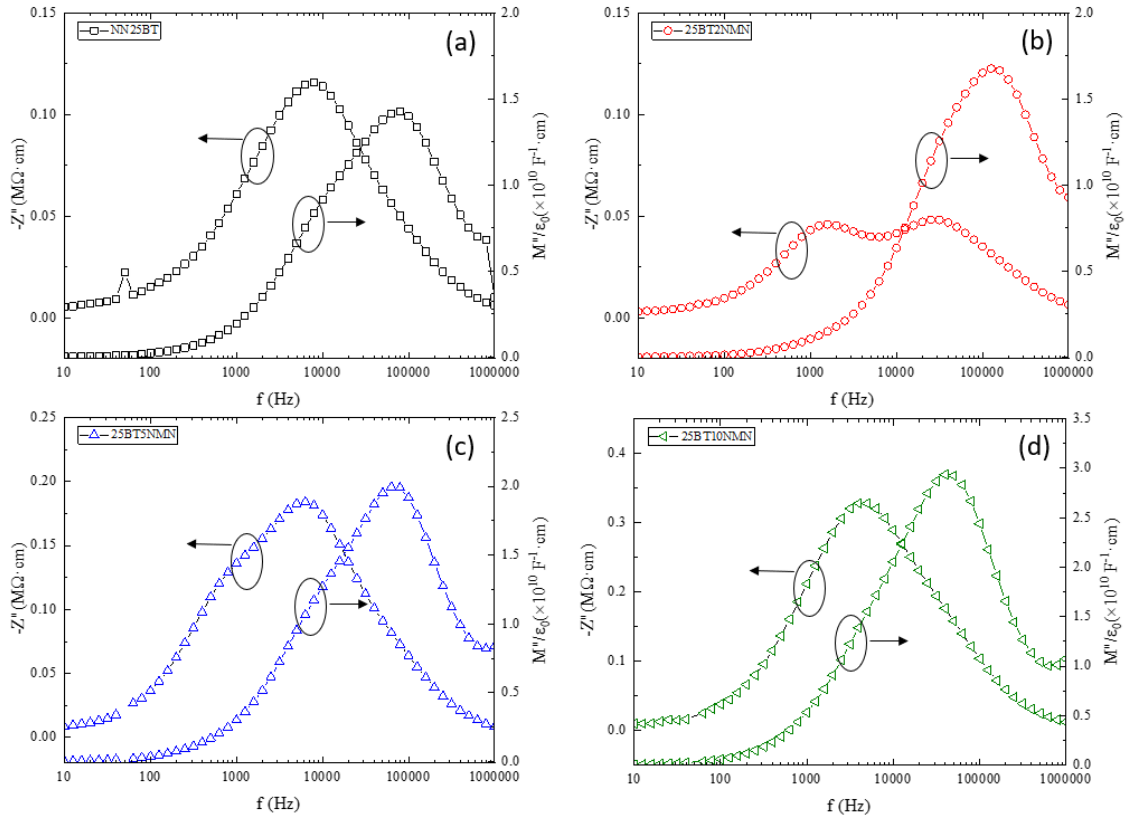

Fig. 4.49 The frequency dependence of Z" and M" of (a) NN25BT, (b) NN25BT2NMN, (c) NN25BT5NMN, (d) NN25BT10NMN ceramics at 550 °C.

4.6.3 High Field Performance

The P-E loops of NN15BT100xNMN and NN25BT100xNMN ceramics are shown in Fig. 4.50. The polarisation values under the same electric field decrease with increasing x, which is consistent with variation in permittivity shown in LCR spectra shown in Fig. 4.45 and Fig. 4.46. Permittivity value is theoretically equal to the derivative of P-E loop for linear dielectric materials. However, the permittivity of NN15BT2NMN at room temperature is higher than NN15BT, which is not reflected in the P-E loop. This may be due to the presence of ferroelectric domains in NN15BT. The long range ordered dipoles could not be switched under high frequency, low field LCR measurement, but could be switched and contribute to the polarisation under low frequency high field P-E measurement, giving a higher polarisation value than the more relaxed NN15BT2NMN composition. As shown in Fig. 4.36, NN100xBT compositions only exhibit weak relaxor characteristics even up to x = 0.25, so the presence of ferroelectric domains is reasonable in NN15BT ceramics.

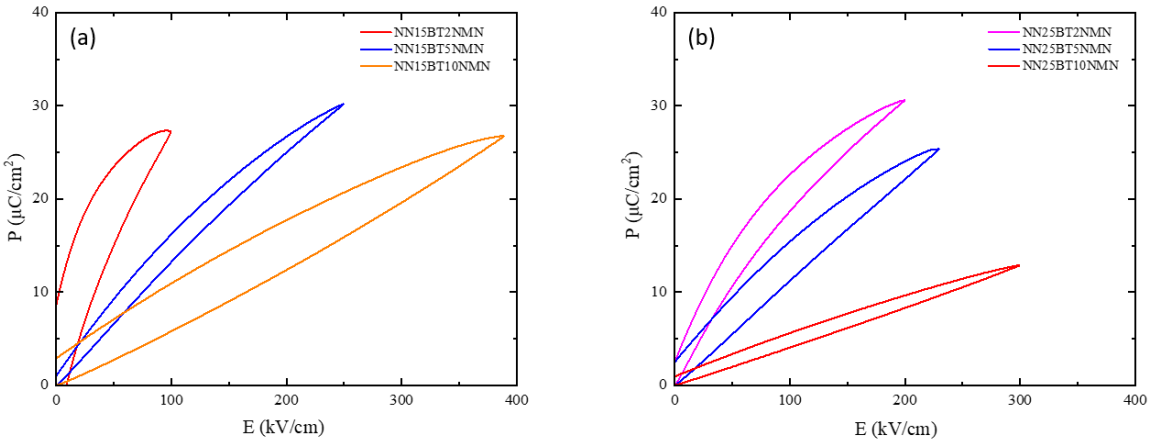

Fig. 4.50 Polarisation versus electric field for (a) NN15BT100xNMN and (b) NN25BT100xNMN ceramics at room temperature under 1 Hz.

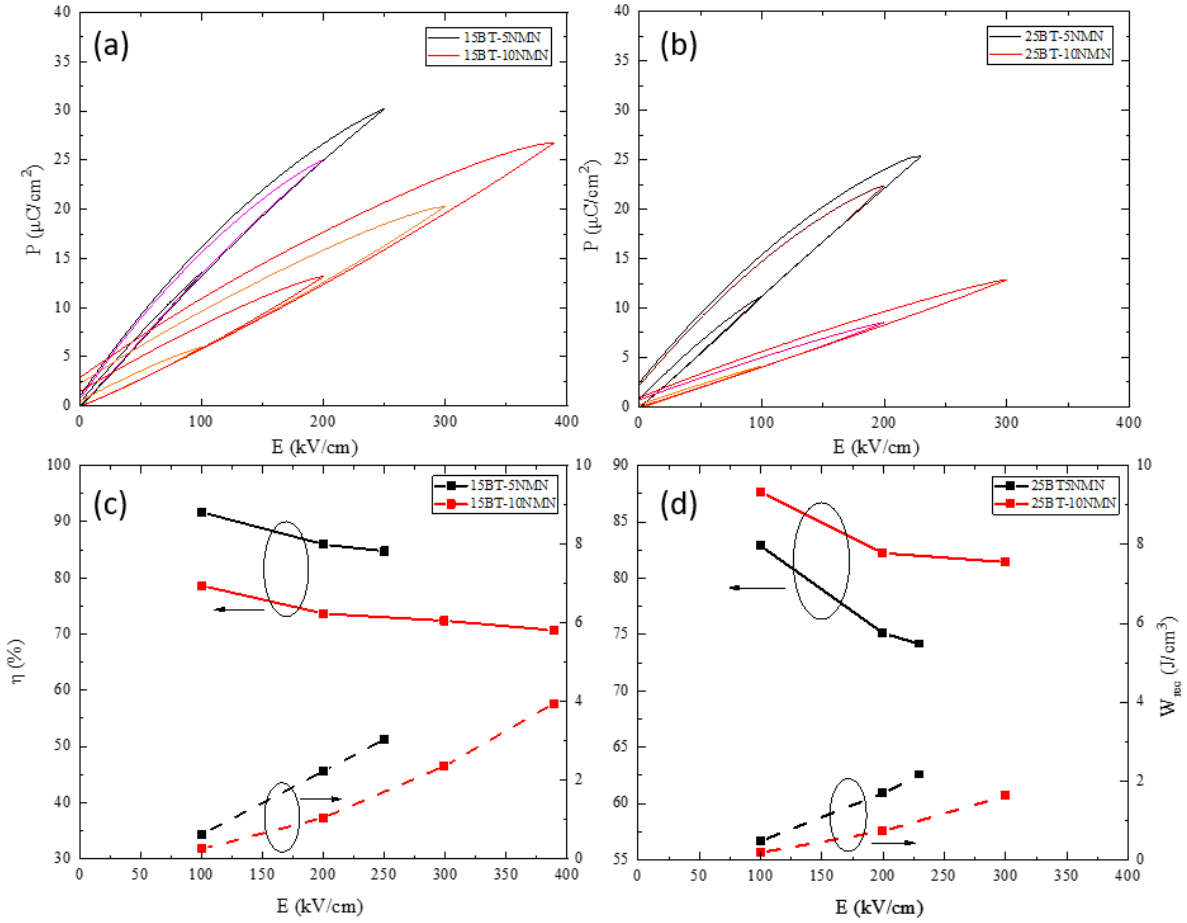

Fig. 4.51 Unipolar P-E loops of (a) NN15BT5NMN and NN15BT10NMN ceramics and (b) NN25BT5NMN and NN25BT10NMN ceramics. The dependence of energy storage performance (W_{rec}, η) on electric field for (c) NN15BT5NMN and NN15BT10NMN ceramics and (d) NN25BT5NMN and NN25BT10NMN ceramics.

The field dependency of P-E loops and energy storage performance of NN15BT5NMN, NN15BT10NMN, NN25BT5NMN and NN25BT10NMN ceramics are shown in Fig. 4.51. The

W_{rec} for all compositions increase with increasing field. The highest W_{rec} is 3.95 J/cm^2, which is achieved in NN15BT10NMN ceramics with η of 70.67 %. η for most compositions decreases with increasing field, with the highest obtained in NN15BT5NMN, 84.74 % and W_{rec} of 3.04 J/cm^2 at 250 kV/cm. For NN25BT based compositions, a high η of 81.43 % is seen in NN25BT10NMN, with W_{rec} of 1.62 J/cm^2. An AC BDS of over 300 kV/cm is achieved for both NN15BT and NN25BT based compositions.

4.6.4 Summary

This chapter focuses on (0.85-x)$NaNbO_3$-0.15$BaTiO_3$-x$Nd(Mg_{2/3}Nb_{1/3})O_3$ (NN15BT100xNMN) and (0.75-x)$NaNbO_3$-0.25$BaTiO_3$-x$Nd(Mg_{2/3}Nb_{1/3})O_3$ (NN25BT100xNMN) ceramics, forming solid solutions with a minor secondary $Ba_4Nb_2O_9$ phase. The phase transition, indicated by T_{max} in the permittivity-temperature spectrum, broadens and shifts towards lower temperature as x increases. Impedance spectra reveal at least two R-C components represented by M" and Z" peaks at various frequencies for all compositions. In NN25BT100xNMN ceramics, the electrical microstructure evolves from inhomogeneous for NN25BT2NMN to more homogeneous with increasing x. Regarding energy storage performance, NN15BT10NMN ceramics achieve the highest W_{rec} of 3.95 J/cm2 with η reaching 70.67%. NN25BT10NMN exhibits a high η of 81.43% with W_{rec} of 1.62 J/cm2. In summary, a range of novel high-field energy storage dielectrics based on NN-BT solid solutions has been developed.

4.7 Multilayer Ceramic Capacitor (MLCC) for Mg doped $0.9BaTiO_3$-$0.1NaNbO_3$

To evaluate the performance of a ceramic composition in devices, it is reasonable to fabricate and characterise prototype MLCCs. The $(Ba_{0.9}Na_{0.1})(Ti_{0.89}Nb_{0.1}Mg_{0.01})O_{2.99}$ (BT10NN-1Mg) composition investigated in section 4.2 is used in this section as it provides high permittivity and temperature stability at the same time.

4.7.1 Fabrication of MLCCs Based on $(Ba_{0.9}Na_{0.1})(Ti_{0.89}Nb_{0.1}Mg_{0.01})O_{2.99}$

The ceramic powders were batched with Ethyl methyl ketone (Fisher Chemical) as the binder, poly(propylene carbonate) (EMPOWER Materials) as the dispersant and binder, and butyl benzyl phthalate (Sigma-Aldrich) as the plasticiser in a weight ratio of 40:22.36:3.47:0.64. The mixture was ball milled for 24 hours with rolling ball mill machine and speed-mixed for 15 minutes with Speed-mixer DAC 800 FVZ (Hauschild Engineering) to ensure homogeneous particle distribution for the slurry.[192] Viscosity of the slurry was controlled, allowing the production of high-quality tape. If the slurry is too thin, it spreads out after casting; if too thick, it sticks to the back on the blade after cast. An appropriate solid loading in the slurry is also critical to achieve high relative density of sintered MLCC. The slurry was cast onto silicon coated polyethylene terephthalate (PET) carrier film using an MSK-AFA-II automatic thick film coater (MTI Corporation). After casting, the tape was dried at room temperature for 1 hour.

For screen printing, the dried green tape was first cut into appropriate dimension. Then, indentations were made with a sheet cutting jig to indicate area for the screen print. After that, a platinum electrode ink (C80225P3, Sun Chemical) was applied to the tape using a HaikuTech P-400S screen printer. The electrode pastes squeezes though a mesh with permeable area of defined geometry onto the green tape during the process. The sheet was then left at room temperature overnight to dry.

Before lamination, the green tape was cut according to the previous indentations. A blade was used to cut the tape and peel it off the PET carrier film. The square sheets were then stacked with around 1mm out of register with each neighbouring layer, exposing one electrode for each terminal only. 10 buffer layers with no electrode were added on top and bottom of the active layers, respectively. The stacked green sheets were then pressed with 10MPa of pressure at 70 ℃ for 20 minutes using a uniaxial press.

After lamination, samples were cut according to the position of the electrodes to form green devices. The devices require several steps to fully burn out the organic chemicals and sinter properly. According to the decomposition temperature of the chemicals, the binder burnout is carried out at 300 ℃ and 600 ℃ for 3 hours, with a heating rate of 1 ℃/min. Sintering temperature is typically around 40 ℃ lower than that of monolithic ceramics.

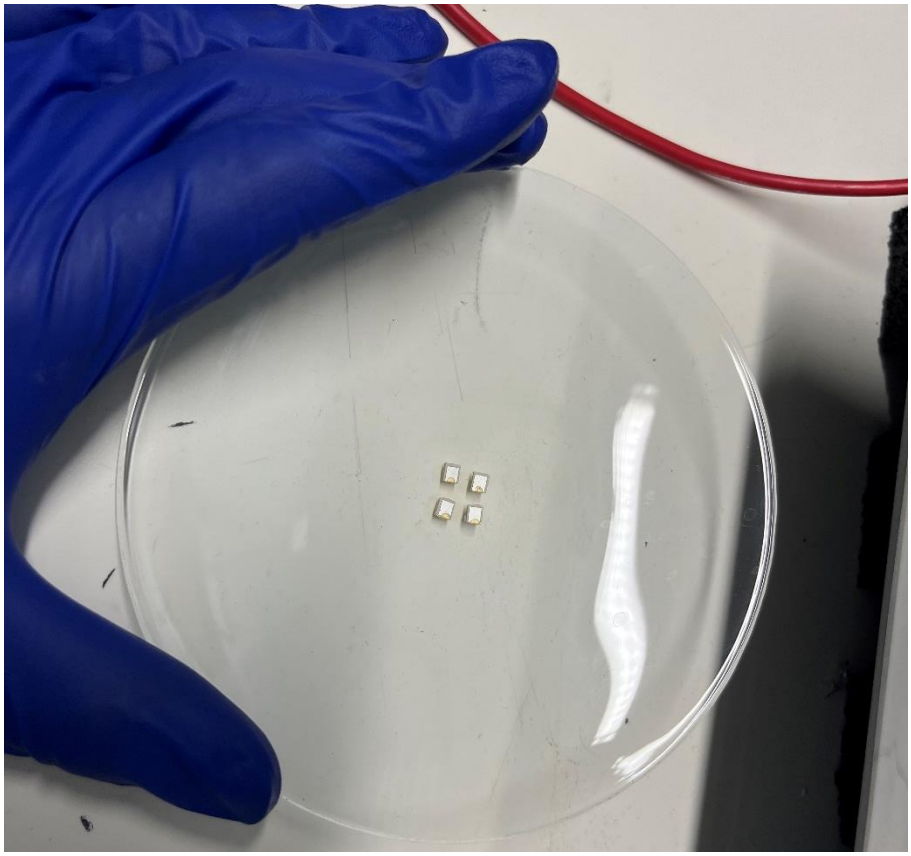

Fig. 4.52 MLCCs fabricated in this project.

Finally, the sintered devices were polished on both ends to expose the inner electrodes. Then, gold paste was applied to the two ends of the device and fired at 850 ℃ for 2 hours to form terminal electrodes. The final MLCC prototypes are shown in Fig. 4.52.

For the composition used for MLCC fabrication in this chapter, 5 wt% of Asahi glass composed of SiO_2, BaO and CaO, was added to the ceramic powder after calcination and mixed by ball milling, to reduce the sintering temperature of the MLCC.

4.7.2 Microstructure

The SEM image and EDX mapping of BT10NN-1Mg MLCC (1Mg MLCC) is shown in Fig. 4.53. Based on the SEM images, the thickness of the active layer is about 18 μm, the active area of the electrode is 4.95 mm^2. An overall homogenous distribution of Ba, Ti, Nb, and O is shown by the EDX mapping result. In the BSE image shown in Fig. 4.54, some areas are darker than the rest of regions in the ceramic sample. From the EDX spectrum shown in Fig. 4.54 (b), these areas have significantly higher Si concentration, indicating they are most likely the glass phase, added to reduce the sintering temperature (1280 ℃).

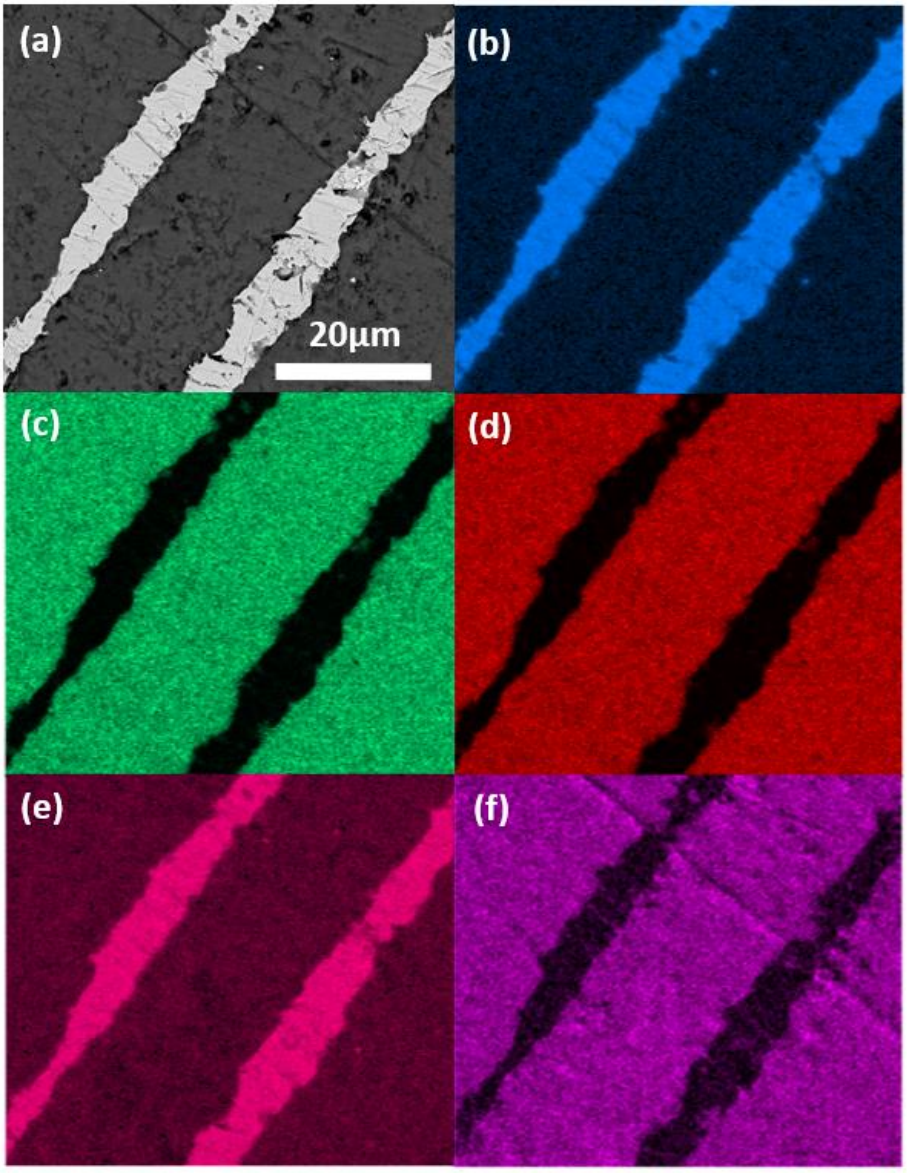

Fig. 4.53 (a) SEM image of the intercept of 1Mg MLCC; the EDX mapping of (b) Pt, (c) Ba, (d) Ti, (e) Nb, (f) O element.

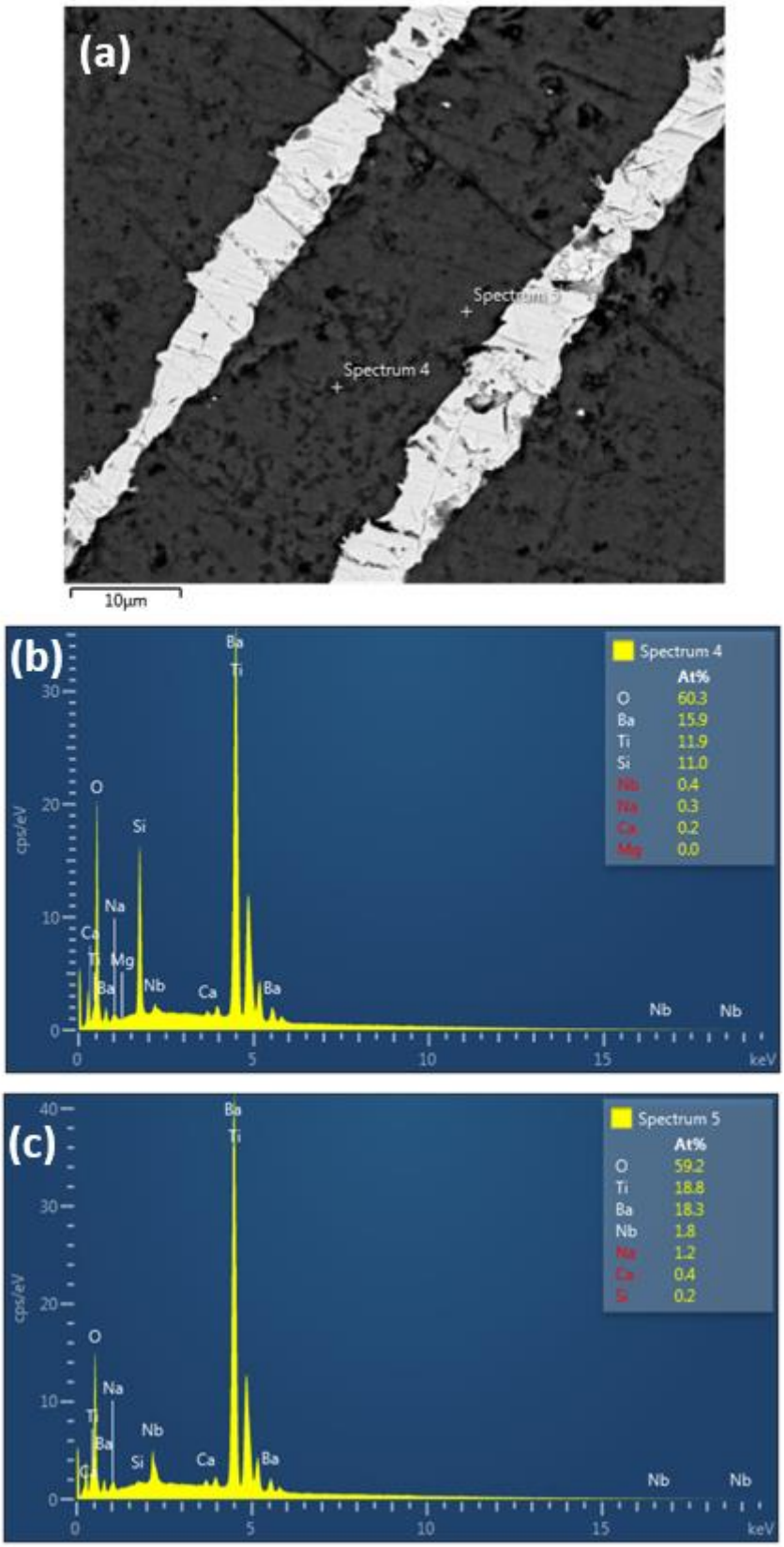

Fig. 4.54 (a) BSE image of 1Mg MLCC, (b) EDX spectrum of dark regions of the sample, (c) EDX spectrum of light regions of the sample.

4.7.3 Low Field Dielectric Behaviour

The low field dielectric behaviour shown in Fig. 4.55 is very similar to that of BT10NN-1Mg monolithic ceramic. However, the tan δ of MLCC is 0.015 at room temperature and exceeds 0.02 above 294 ℃, while the tan δ of BT10NN-1Mg monolithic ceramic is 0.013 at room temperature, and only exceeds 0.02 above 397 ℃. The higher loss of MLCC may be due to the added glass content.

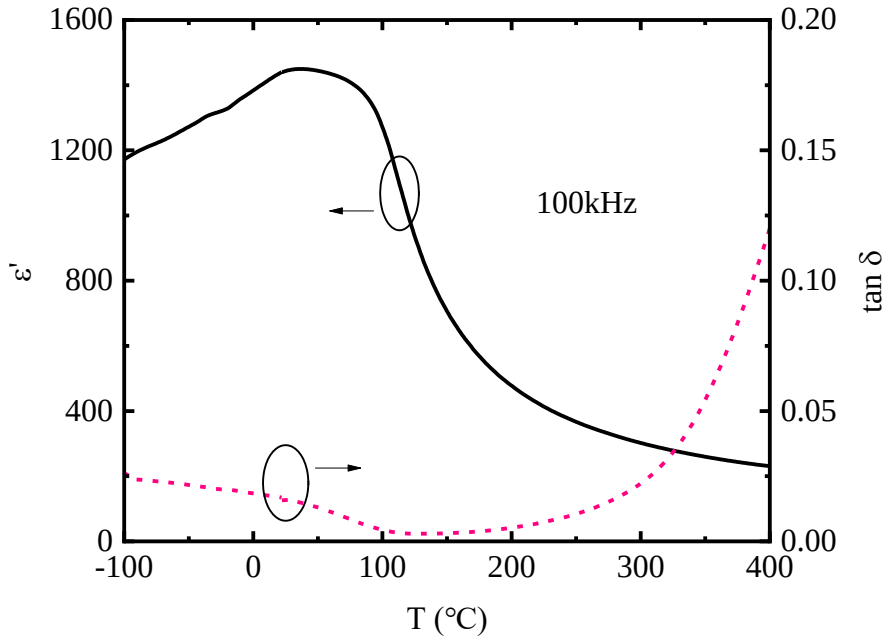

Fig. 4.55 The temperature dependence of ε_r and tan δ for 1Mg MLCC at 100 kHz.

4.7.4 High Field Performance

The high field behaviour was characterised by P-E loops along with energy storage performance. The electrode area and dielectric layer thickness were confirmed with SEM images. As shown in Fig. 4.56, the polarisation of the MLCC under 50 kV/cm is 6.82 μC/cm^2, slightly lower than that of monolithic ceramic with glass addition, 7.05 μC/cm^2. The decrease may be due to clamping of inner electrode or a decrease in effect volume of the high permittivity dielectric. As shown in Fig. 4.57 (b), a high η of > 80 % is obtained for samples measured at all fields. The highest W_{rec} of 3.36 J/cm^3 is achieved at 375 kV/cm, with a η of 80.6 %. The η of MLCC is lower than BT10NN-1Mg ceramics at the same field strength, possibly due to the addition of glass.

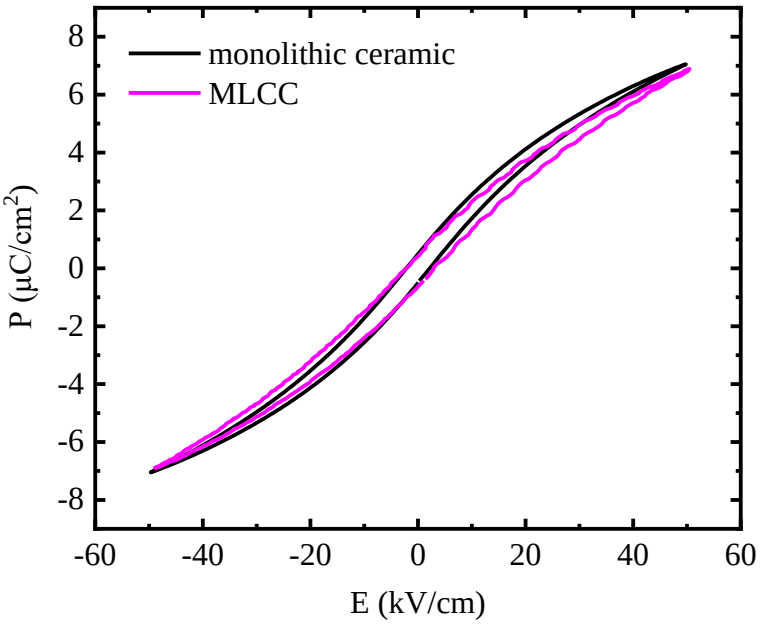

Fig. 4.56 P-E loop of the monolithic ceramic and MLCC.

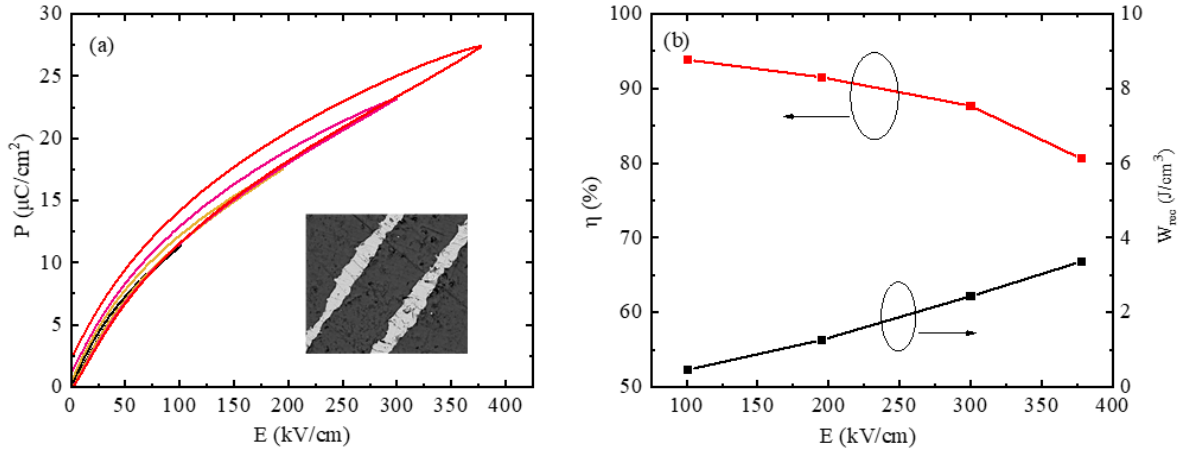

Fig. 4.57 (a)The P-E loop of 1Mg MLCC under different electric field strength, inset is the SEM image of the intercept of MLCC, (b) the dependence of W_{rec} and η for 1Mg MLCC on electric field strength.

Table 4.3 A summary and comparison of the electrical performance of BT10NN-1Mg ceramics and other ferroelectric/antiferroelectric/relaxor ceramics.

Comps.	*ε'* @ RT	*tan δ* @ RT	W_{rec} (J/cm³)	*η* (%)	*E* (kV/cm)	Sustain.	Compat.	Ref.
BT10NN-1Mg	1700	0.013	3.40	83	400	Y	Y	This work
BNT	2400	0.181	1.25	76	116	Y	N	[193]
BF	500	0.054	6.10	72	410	Y	N	[30]
AN	248	0.007	1.64	33	144	Y	N	[127]
PLZT	275	0.006	12.30	84	420	N	Y	[194]
PLZS	180	-	10.40	87	400	N	Y	[65]

Finally, a summary and comparison of the electrical performance of BT10NN-1Mg ceramics and other common electroceramics is shown in Table 4.3. Given the high dielectric and energy storage performance, as well as the sustainability of the composition (Pb, Bi and RE free), the compatibility with current industrial standard and process, BT10NN-1Mg is a good candidate for next generation energy storage MLCC applications.

4.7.5 Summary

This chapter delves into the fabrication of MLCCs based on BT10NN-1Mg, showcasing the absence of voids or delamination in the prototype device. The successful reduction of sintering temperature is attributed to the added glass phase, visibly identified in SEM images with a glass-rich phase. The frequency dependence of ε' and tan δ mirrors that of monolithic ceramic. A decrease in polarization is evident in the MLCC compared to monolithic ceramic due to the glass addition. The MLCC demonstrates excellent high-field energy storage performance, achieving W_{rec} of 3.36 J/cm3 and η of 80.6%, establishing the composition's potential for next-generation energy storage MLCC applications.

5 Conclusions

5.1 (1-x)$BaTiO_3$-x$NaNbO_3$ ceramics

The properties of BT-xNN ceramics were investigated to find suitable base material for further optimization. BT-xNN ceramics exhibited cubic crystal structures and inhomogeneous distribution of grain sizes. A core-shell type permittivity-temperature spectrum was shown for x < 0.25 compositions. Narrow P-E loops were attained for all compositions, with a more linear response with increasing x. BT10NN was adjudged to be the most suitable base material for further optimization from the permittivity-temperature spectra and P-E loops.

5.2 Mg and Nb doped $BaTiO_3$-$NaNbO_3$ ceramics

Mg and Nb doped BT10NN ceramics were fabricated and characterised. At low dopant level, Mg was thought to enter the A site but switched to the B site at higher concentrations ($x \geq 0.02$). The plateau within the permittivity-temperature spectra merged into a single peak for $x \geq 0.02$, which was accompanied by significant grain growth and an electrical core-shell response in impedance spectra. Nb substituted only on the B-site. For Nb doped compositions, the plateau in permittivity-temperature spectra moved to lower temperature with increasing dopant concentration, but the core-shell response could not be clearly resolved in the frequency spectrum of M" and Z" for these compositions.

In Mg doped samples, x = 0.02 showed the lowest resistivity and highest activation energy. For Nb doped compositions, activation energy and resistivity decreased with increasing dopant level. In Mg doped compositions, conduction mechanism shifts from n- to p-type at x = 0.02, then back to n-type. In Nb doped compositions, the conduction mechanism remained n type. In terms of energy storage performance, Mg doping was found to reduce the polarisation, but enhanced the BDS of the ceramic. Nb doping enhanced polarisation and W_{rec} of the ceramic with y = 0.02 showing the highest W_{rec} of 4.95 J/cm^3 with η of 81%.

5.3 (1-x)$NaNbO_3$-x$BaTiO_3$ ceramics

The structural and electrical properties of BT100xNN ($0.25 \geq x \geq 0.0$) ceramics are investigated in this chapter. The crystal structure transforms from orthorhombic to tetragonal with increasing x. The grain size first decreased, then increased with increasing x. T_{max} in the permittivity temperature plots decreased with increasing x. Only weak frequency dependency of T_{max} was shown in the compositions even with x = 0.25. The oxygen ion conductivity decreased from > 0.3 to ~ 0.005 at 800 ℃ with x increasing from 0 to 0.15. The reduced oxygen ion conductivity is crucial for dielectric capacitor applications. The electrical microstructure of the ceramic was analysed. The high field polarisation response shows]ed a trend from antiferroelectric to ferroelectric, then to a weak 'relaxor-type' behaviour with increasing x.

5.4 $(0.85\text{-}x)NaNbO_3\text{-}0.15BaTiO_3\text{-}xNd(Mg_{2/3}Nb_{1/3})O_3$ and $(0.75\text{-}x)NaNbO_3\text{-}0.25BaTiO_3\text{-}xNd(Mg_{2/3}Nb_{1/3})O_3$ ceramics

For $(0.85\text{-}x)NaNbO_3\text{-}0.15BaTiO_3\text{-}xNd(Mg_{2/3}Nb_{1/3})O_3$ (NN15BT100xNMN)and $(0.75\text{-}x)NaNbO_3\text{-}0.25BaTiO_3\text{-}xNd(Mg_{2/3}Nb_{1/3})O_3$ (NN25BT100xNMN)ceramics, solid solutions were formed with minor secondary $Ba_4Nb_2O_9$ phase. Phase transition indicated by T_{max} in permittivity-temperature spectrum becomes broader and moves towards lower temperature with increasing x. In the impedance spectra, at least two R-C components were indicated by M" and Z" peaks at different frequencies for all compositions. For NN25BT100xNMN ceramics, the electrical microstructure was inhomogeneous for NN25BT2NMN, then became more homogeneous with increasing x. In terms of energy storage performance, the highest W_{rec} of 3.95 J/cm^2 was achieved in NN15BT10NMN ceramics with η of 70.67 %. A high η of 81.43 % was achieved in NN25BT10NMN, with W_{rec} of 1.62 J/cm^2. Overall, a range of novel high field energy storage dielectrics based on NN-BT solid solution were developed.

5.5 Multilayer Ceramic Capacitor (MLCC) for Mg Doped $0.9BaTiO_3\text{-}0.1NaNbO_3$

MLCCs based on BT10NN-1Mg were fabricated with no voids or delamination. The added glass phase reduced the sintering temperature successfully. Some glass rich phase is visible from SEM images. The frequency dependence of ε' and tan δ are similar to that of monolithic ceramic. A decrease in polarisation was observed in the MLCC compared with monolithic ceramic, due to the glass addition. Good high field energy storage performance of with W_{rec} of 3.36 J/cm^3 and η of 80.6 % were achieved, proving the potential of the composition in application for next-generation energy storage MLCC.

6 Future Work

In this thesis, a range of compositions based on $BaTiO_3$-$NaNbO_3$ solid solution was investigated for their application as high field/energy storage dielectrics. An optimised energy storage performance was achieved in $(Ba_{0.9}Na_{0.1})(Ti_{0.89}Nb_{0.1}Mg_{0.01})O_{2.99}$ ceramics with W_{rec} = 3.4 J/cm^3 with η of 82.6% at 400 kV/cm. The successful fabrication of an MLCC based on this composition confirmed its potential for energy storage MLCC applications. Due to the limited time of this PhD project, some directions require further elucidation:

i) Structure

The evolution of crystal structure and lattice parameters for the BT-NN solid solution with different BT and NN content require more detailed analysis, such as Reitveld refinement of XRD data. The local crystal structure would benefit from selected area electron diffraction with the domain structure of the materials transmission electron microscopy (TEM) and piezoelectric force microscopy (PFM). The defect chemistry and defect types could be further analysed with electron paramagnetic resonance (EPR) and X-ray photoelectron spectroscopy (XPS). Fourier transformation infrared spectroscopy (FTIR) could be applied to investigate the state of chemical bond in the samples and the local distortion of oxygen octahedral could be probed with neutron diffraction.

ii) Properties

The energy storage performance of the compositions could be further improved by adding end members in the solid solution or doping, taking into account the polarizability, electronegativity, size, valence, shell electron state of ions. The ease of fabrication, such as the volatility of elements and the possible existence of competing phases should be considered. Processing should be better controlled with improvement in the raw material purity and particle size with more comprehensive studies to further refine the time and temperature for the calcination and sintering. Overall, provided careful design of composition, optimised processing route, and controlled operation environment, ceramics with higher quality and stability may be achievable in these solid solutions.

iii) MLCC

In this project, prototype MLCCs were fabricated with Pt inner electrode, which is an expensive noble metal not suitable for commercial applications. In the future, sintering temperature could be reduced by using ceramic powders with smaller particle sizes and/or alternative glass additions as sintering aids. Ag-Pd or even Ni internal electrodes may then be utilised. From a device design perspective, different configurations of inner electrode could be applied to enhance the reliability of MLCCs, allowing local breakdown without device failure.

References

1. Z. Lu, G. Wang, W. Bao, J. Li, L. Li, A. Mostaed, H. Yang, H. Ji, D. Li, A. Feteira, F. Xu, D. C. Sinclair, D. Wang, S.-Y. Liu and I. M. Reaney, Energy & Environmental Science **13** (9), 2938-2948 (2020).
2. Lucintel, (https://www.lucintel.com/capacitor-market.aspx, 2022).
3. E. S. news, (https://passive-components.eu/ecia-reports-north-america-capacitor-sales-up-0-5-and-bookings-up-6-5/, 2017).
4. ReportLinker, (https://uk.finance.yahoo.com/news/multi-layer-ceramic-capacitor-mlcc-133400162.html?guccounter=1&guce_referrer=aHR0cHM6Ly93d3cuZ29vZ2xlLmNvLnVrLw&guce_referrer_sig=AQAAADGakY8mqR7NDYOcxxxCWtkUGvb31JkxJFTkaX5UImvoisMTom4VRRxwIuLq20Ye5z7-TVQ05_a49oq31G3O2pgYBOeq885nLsrEP4SrjNx7cbgtRlKxiggF18ZwlwwNcYfgVIodw82sxpTnNwKVIVp5gQzsSIxWDwGWy1xkcz-C, 2022).
5. EMR, (https://www.expertmarketresearch.com/reports/multi-layer-ceramic-capacitor-market, 2022).
6. (https://article.murata.com/en-sg/article/automotive-mlcc-3, 2021).
7. D. Fu and M. Itoh, arXiv preprint arXiv:1108.5819 (2011).
8. C. I. Cheon, H. W. Joo, K. W. Chae, J. S. Kim, S. H. Lee, S. Torii and T. Kamiyama, Materials Letters **156**, 214-219 (2015).
9. Y. Noguchi and H. Matsuo, Nanomaterials (Basel) **12** (23) (2022).
10. W. Travis, E. N. K. Glover, H. Bronstein, D. O. Scanlon and R. G. Palgrave, Chemical Science **7** (7), 4548-4556 (2016).
11. A. M. Glazer, Acta Crystallographica Section B **28** (11), 3384-3392 (1972).
12. N. A. Benedek and C. J. Fennie, The Journal of Physical Chemistry C **117** (26), 13339-13349 (2013).
13. F. H. Schader, (2016).
14. T. Ishidate, S. Abe, H. Takahashi and N. Môri, Physical review letters **78** (12), 2397 (1997).
15. M. Acosta, N. Novak, V. Rojas, S. Patel, R. Vaish, J. Koruza, G. Rossetti Jr and J. Rödel, Applied Physics Reviews **4** (4), 041305 (2017).
16. K. E. Johnston, C. C. Tang, J. E. Parker, K. S. Knight, P. Lightfoot and S. E. Ashbrook, Journal of the American Chemical Society **132** (25), 8732-8746 (2010).
17. M.-H. Zhang, L. Fulanović, C. Zhao and J. Koruza, Journal of Materiomics **9** (1), 1-18 (2023).
18. S. Aso, H. Matsuo and Y. Noguchi, Scientific Reports **13** (1), 6771 (2023).
19. C. Ricca and U. Aschauer, Applied Physics A **128** (12), 1083 (2022).
20. A. Chandrasekaran, D. Damjanovic, N. Setter and N. Marzari, Physical Review B **88** (21), 214116 (2013).
21. Y. Jia, H. Fan, A. Zhang, H. Wang, L. Lei, Q. Quan, G. Dong, W. Wang and Q. Li, Journal of the European Ceramic Society **43** (3), 947-956 (2023).
22. B. Wang, W. Huang, L. Chi, M. Al-Hashimi, T. J. Marks and A. Facchetti, Chemical reviews **118** (11), 5690-5754 (2018).
23. R. Dorey, in *Ceramic Thick Films for MEMS and Microdevices*, edited by R. Dorey (William Andrew Publishing, Oxford, 2012), pp. 85-112.
24. T. Kimura, T. Goto, H. Shintani, K. Ishizaka, T. Arima and Y. Tokura, Nature **426** (6962), 55-58 (2003).
25. X. Liu, P. Tan, X. Ma, D. Wang, X. Jin, Y. Liu, B. Xu, L. Qiao, C. Qiu, B. Wang, W. Zhao, C. Wei, K. Song, H. Guo, X. Li, S. Li, X. Wei, L.-Q. Chen, Z. Xu, F. Li, H. Tian and S. Zhang, Science **376** (6591), 371-377 (2022).
26. X. Xu, T. Wang, P. Chen, C. Zhou, J. Ma, D. Wei, H. Wang, B. Niu, X. Fang, D. Wu, S. Zhu, M. Gu, M. Xiao and Y. Zhang, Nature **609** (7927), 496-501 (2022).
27. C. Qiu, B. Wang, N. Zhang, S. Zhang, J. Liu, D. Walker, Y. Wang, H. Tian, T. R. Shrout, Z. Xu, L.-Q. Chen and F. Li, Nature **577** (7790), 350-354 (2020).

28. H. Palneedi, M. Peddigari, G.-T. Hwang, D.-Y. Jeong and J. Ryu, Advanced Functional Materials **28** (42), 1803665 (2018).
29. F. Yan, H. Bai, G. Ge, J. Lin, C. Shi, K. Zhu, B. Shen, J. Zhai and S. Zhang, Small **18** (10), 2106515 (2022).
30. X. Wang, Y. Fan, Z. Bin, A. Mostaed, L. Li, A. Feteira, D. Wang, D. C. Sinclair, G. Wang and I. M. Reaney, Journal of the European Ceramic Society **42** (15), 7381-7387 (2022).
31. H. Ji, D. Wang, W. Bao, Z. Lu, G. Wang, H. Yang, A. Mostaed, L. Li, A. Feteira, S. Sun, F. Xu, D. Li, C.-J. Ma, S.-Y. Liu and I. M. Reaney, Energy Storage Materials **38**, 113-120 (2021).
32. H. Qi, R. Zuo, A. Xie, A. Tian, J. Fu, Y. Zhang and S. Zhang, Advanced Functional Materials **29** (35), 1903877 (2019).
33. X. Hao, J. Zhai, L. B. Kong and Z. Xu, Progress in Materials Science **63**, 1-57 (2014).
34. L. Li, P. Fan, M. Wang, N. Takesue, D. Salamon, A. N. Vtyurin, Y. Zhang, H. Tan, B. Nan, Y. Lu, L. Liu and H. Zhang, Journal of Physics D: Applied Physics **54** (29), 293001 (2021).
35. G. Wang, Z. Lu, Y. Li, L. Li, H. Ji, A. Feteira, D. Zhou, D. Wang, S. Zhang and I. M. Reaney, Chemical Reviews **121** (10), 6124-6172 (2021).
36. Z. Liu, T. Lu, J. Ye, G. Wang, X. Dong, R. Withers and Y. Liu, Advanced Materials Technologies **3** (9), 1800111 (2018).
37. H. Pan, S. Lan, S. Xu, Q. Zhang, H. Yao, Y. Liu, F. Meng, E.-J. Guo, L. Gu, D. Yi, X. Renshaw Wang, H. Huang, J. L. MacManus-Driscoll, L.-Q. Chen, K.-J. Jin, C.-W. Nan and Y.-H. Lin, Science **374** (6563), 100-104 (2021).
38. W.-H. Lee and C.-Y. Su, Journal of the American Ceramic Society **90** (10), 3345-3348 (2007).
39. Y. H. Song, J. H. Hwang and Y. H. Han, Japanese journal of applied physics **44** (3R), 1310 (2005).
40. Y. Sakabe, Y. Hamaji, H. Sano and N. Wada, Japanese Journal of Applied Physics **41** (9R), 5668 (2002).
41. Y. Mizuno, H. Kishi, K. Ohnuma, T. Ishikawa and H. Ohsato, Journal of the European Ceramic Society **27** (13), 4017-4020 (2007).
42. C.-H. Kim, K.-J. Park, Y.-J. Yoon, M.-H. Hong, J.-O. Hong and K.-H. Hur, Journal of the European Ceramic Society **28** (6), 1213-1219 (2008).
43. H. Kishi, Y. Okino, M. Honda, Y. Iguchi, M. Imaeda, Y. Takahashi, H. Ohsato and T. Okuda, Japanese Journal of Applied Physics **36** (9S), 5954 (1997).
44. R. T. Shannon and C. T. Prewitt, Acta Crystallographica Section B: Structural Crystallography and Crystal Chemistry **25** (5), 925-946 (1969).
45. M. J. Pan and C. A. Randall, IEEE Electrical Insulation Magazine **26** (3), 44-50 (2010).
46. H. Kishi, Y. Mizuno and H. Chazono, Japanese journal of applied physics **42** (1R), 1 (2003).
47. , Vol. 2023.
48. D. N. Donahoe, University of Maryland, 2005.
49. G. Kuegerl, (2012).
50. C.-N. Xu, M. Akiyama, K. Nonaka and T. Watanabe, IEEE transactions on ultrasonics, ferroelectrics, and frequency control **45** (4), 1065-1070 (1998).
51. Y. Li, N. Sun, X. Li, J. Du, L. Chen, H. Gao, X. Hao and M. Cao, Acta Materialia **146**, 202-210 (2018).
52. R. N. Perumal and V. Athikesavan, Journal of Materials Science: Materials in Electronics **30** (1), 902-913 (2019).
53. T. F. Zhang, X. G. Tang, Q. X. Liu, Y. P. Jiang, X. X. Huang and Q. F. Zhou, Journal of Physics D: Applied Physics **49** (9), 095302 (2016).
54. M. Chao, J. Liu, M. Zeng, D. Wang, H. Yu, Y. Yuan and S. Zhang, Applied Physics Letters **112** (20), 203903 (2018).
55. S. I. Shkuratov, J. Baird, V. G. Antipov, W. Hackenberger, J. Luo, S. Zhang, C. S. Lynch, J. B. Chase, H. R. Jo and C. C. Roberts, Applied Physics Letters **112** (12), 122903 (2018).

56. X. Qi, Y. Zhao, E. Sun, J. Du, K. Li, Y. Sun, B. Yang, R. Zhang and W. Cao, Journal of the European Ceramic Society **39** (14), 4060-4069 (2019).
57. Y. Li, N. Sun, J. Du, X. Li and X. Hao, Journal of Materials Chemistry C **7** (25), 7692-7699 (2019).
58. E. Sawaguchi, H. Maniwa and S. Hoshino, Physical review **83** (5), 1078 (1951).
59. H. R. Jo and C. S. Lynch, Journal of Applied Physics **119** (2), 024104 (2016).
60. J. Gao, Y. Liu, Y. Wang, D. Wang, L. Zhong and X. Ren, Scripta Materialia **137**, 114-118 (2017).
61. B. Li, Q. Liu, X. Tang, T. Zhang, Y. Jiang, W. Li and J. Luo, Materials **10** (2) (2017).
62. X. Wang, J. Shen, T. Yang, Y. Dong and Y. Liu, Journal of Alloys and Compounds **655**, 309-313 (2016).
63. S. Chen, X. Wang, T. Yang and J. Wang, Journal of Electroceramics **32** (4), 307-310 (2014).
64. F. Zhuo, Q. Li, Y. Li, J. Gao, Q. Yan, Y. Zhang, X. Chu and W. Cao, Materials Research Express **1** (4), 045501 (2014).
65. H. Wang, Y. Liu, T. Yang and S. Zhang, Advanced Functional Materials **29** (7), 1807321 (2019).
66. X. Liu, Y. Li and X. Hao, Journal of Materials Chemistry A **7** (19), 11858-11866 (2019).
67. V. A. Isupov, Ferroelectrics **289** (1), 131-195 (2003).
68. G. Samara, Physical Review B **1** (9), 3777 (1970).
69. X. Tan, C. Ma, J. Frederick, S. Beckman and K. G. Webber, Journal of the American Ceramic Society **94** (12), 4091-4107 (2011).
70. J. Wei, T. Yang and H. Wang, Journal of the European Ceramic Society **39** (2), 624-630 (2019).
71. P. Gao, Z. Liu, N. Zhang, H. Wu, A. A. Bokov, W. Ren and Z.-G. Ye, Chemistry of Materials **31** (3), 979-990 (2019).
72. L. Xu, C. He, X. Yang, Z. Wang, X. Li, H. N. Tailor and X. Long, Journal of the European Ceramic Society **37** (10), 3329-3334 (2017).
73. X. Yang, Y. Liu, C. He, H. Tailor and X. Long, Journal of the European Ceramic Society **35** (15), 4173-4180 (2015).
74. C. Moure and O. Peña, Progress in Solid State Chemistry **43** (4), 123-148 (2015).
75. P. Qiao, Y. Zhang, X. Chen, M. Zhou, G. Wang and X. Dong, Journal of Alloys and Compounds **780**, 581-587 (2019).
76. B. Li, Q.-X. Liu, X.-G. Tang, T.-F. Zhang, Y.-P. Jiang, W.-H. Li and J. Luo, RSC Advances **7** (68), 43327-43333 (2017).
77. I. V. Ciuchi, L. Mitoseriu and C. Galassi, Journal of the American Ceramic Society **99** (7), 2382-2387 (2016).
78. A. Kumar, S. H. Kim, M. Peddigari, D.-H. Jeong, G.-T. Hwang and J. Ryu, Electronic Materials Letters **15** (3), 323-330 (2019).
79. Z. Fu, X. Chen, Z. Li, T. Hu, L. Zhang, P. Lu, S. Zhang, G. Wang, X. Dong and F. Xu, Nature Communications **11** (1), 3809 (2020).
80. Y. Dan, H. Xu, K. Zou, Q. Zhang, Y. Lu, G. Chang, H. Huang and Y. He, Applied Physics Letters **113** (6), 063902 (2018).
81. G. Engel, M. Schossmann, M. Koini, A. Testino and C. Hoffmann, (Google Patents, 2016).
82. G. Engel, M. Koini, J. Konrad and M. Schossmann, presented at the Proc. of the IEEE Intern. Exhibit. and Conf. for Power Electron., Intel. Motion, Renew. Energy and Energy Managem.(PCIM), Nuremberg, 2012 (unpublished).
83. J. Konrad, M. Koini, M. Schossmann and M. Puff, presented at the Proceedings of the Congress on Automotive Electronic Systems, Deutschlandsberg, Austria, 2014 (unpublished).
84. C. M. Sylvia E. Gebhardt, Holger Neubert, presented at the IEEE International Symposium on Applications of Ferroelectrics, Tours, France, 2022 (unpublished).
85. G. R. Love, Journal of the American Ceramic Society **73** (2), 323-328 (1990).
86. R. Ma, B. Cui, M. Shangguan, S. Wang, Y. Wang, Z. Chang and Y. Wang, Journal of Alloys and Compounds **690**, 438-445 (2017).

87. X. Lai, H. Hao, Z. Liu, S. Li, Y. Liu, M. Emmanuel, Z. Yao, M. Cao, D. Wang and H. Liu, Journal of Materials Science: Materials in Electronics **31** (11), 8963-8970 (2020).
88. Q. Zhao, X. Wang, H. Gong, B. Liu, B. Luo and L. Li, Journal of the American Ceramic Society **101** (3), 1245-1254 (2018).
89. B. Liu, X. Wang, Q. Zhao and L. Li, Journal of the American Ceramic Society **98** (8), 2641-2646 (2015).
90. D. Zhan, Q. Xu, D.-P. Huang, H.-X. Liu, W. Chen and F. Zhang, Journal of Physics and Chemistry of Solids **114**, 220-227 (2018).
91. J.-P. Ma, X.-M. Chen, W.-Q. Ouyang, J. Wang, H. Li and J.-L. Fang, Ceramics International **44** (4), 4436-4441 (2018).
92. B. Liu, Y. Wu, Y. H. Huang, K. X. Song and Y. J. Wu, Journal of Materials Science **54** (6), 4511-4517 (2019).
93. T. Hasegawa and T. Otagiri, Japanese Journal of Applied Physics **45** (9B), 7360-7364 (2006).
94. T. Wang, X. Wei, Q. Hu, L. Jin, Z. Xu and Y. Feng, Materials Science and Engineering: B **178** (16), 1081-1086 (2013).
95. M. Zeng, J. Liu, H. Yu, M. Chao, B. Tang and S. Zhang, Energy Technology **6** (5), 899-905 (2018).
96. T. Wang, L. Jin, C. Li, Q. Hu and X. Wei, Journal of the American Ceramic Society **98** (2), 559-566 (2015).
97. L. Wu, X. Wang and L. Li, RSC Advances **6** (17), 14273-14282 (2016).
98. Z. Shen, X. Wang, B. Luo and L. Li, Journal of Materials Chemistry A **3** (35), 18146-18153 (2015).
99. H. Yang, F. Yan, Y. Lin, T. Wang, F. Wang, Y. Wang, L. Guo, W. Tai and H. Wei, Journal of the European Ceramic Society **37** (10), 3303-3311 (2017).
100. N. Kumar, A. Ionin, T. Ansell, S. Kwon, W. Hackenberger and D. Cann, Applied Physics Letters **106** (25), 252901 (2015).
101. Q. Hu, Y. Tian, Q. Zhu, J. Bian, L. Jin, H. Du, D. O. Alikin, V. Y. Shur, Y. Feng, Z. Xu and X. Wei, Nano Energy **67**, 104264 (2020).
102. Q. Yuan, G. Li, F.-Z. Yao, S.-D. Cheng, Y. Wang, R. Ma, S.-B. Mi, M. Gu, K. Wang, J.-F. Li and H. Wang, Nano Energy **52**, 203-210 (2018).
103. W.-B. Li, D. Zhou, B. He, F. Li, L.-X. Pang and S.-G. Lu, Journal of Alloys and Compounds **685**, 418-422 (2016).
104. J. Wan, Y. Pu, C. Hui, C. Cui and Y. Guo, Journal of Materials Science: Materials in Electronics **29** (8), 6556-6563 (2018).
105. Z. Yang, H. Du, S. Qu, Y. Hou, H. Ma, J. Wang, J. Wang, X. Wei and Z. Xu, Journal of Materials Chemistry A **4** (36), 13778-13785 (2016).
106. T. Shao, H. Du, H. Ma, S. Qu, J. Wang, J. Wang, X. Wei and Z. Xu, Journal of Materials Chemistry A **5** (2), 554-563 (2017).
107. B. Qu, H. Du, Z. Yang and Q. Liu, Journal of the American Ceramic Society **100** (4), 1517-1526 (2017).
108. B. Qu, H. Du, Z. Yang, Q. Liu and T. Liu, RSC Advances **6** (41), 34381-34389 (2016).
109. T. Correia, M. Stewart, A. Ellmore and K. Albertsen, Advanced Engineering Materials **19** (6), 1700019 (2017).
110. L. Zhang, Y. Pu, M. Chen, R. Li, X. Guo and Y. Cui, Ceramics International **44**, S207-S210 (2018).
111. B. Hu, H. Fan, L. Ning, S. Gao, Z. Yao and Q. Li, Ceramics International **44** (9), 10968-10974 (2018).
112. J. Yin, X. Lv and J. Wu, Ceramics International **43** (16), 13541-13546 (2017).
113. Y. Qiu, Y. Lin, X. Liu and H. Yang, Journal of Alloys and Compounds **797**, 348-355 (2019).
114. Z. Yang, Y. Yuan, L. Cao, E. Li and S. Zhang, Ceramics International **46** (8, Part A), 11282-11289 (2020).

115. L. Zhang, Y. Pu and M. Chen, Ceramics International **46** (1), 98-105 (2020).
116. Q. Xu, H. Liu, L. Zhang, J. Xie, H. Hao, M. Cao, Z. Yao and M. T. Lanagan, RSC Advances **6** (64), 59280-59291 (2016).
117. C. Cui and Y. Pu, Journal of Alloys and Compounds **747**, 495-504 (2018).
118. W. P. Cao, J. Sheng, Y. L. Qiao, L. Jing, Z. Liu, J. Wang and W. L. Li, Journal of the European Ceramic Society **39** (14), 4046-4052 (2019).
119. L. Zhang, Y. Pu, M. Chen and G. Liu, Journal of the European Ceramic Society **38** (16), 5388-5395 (2018).
120. W. Shi, L. Zhang, P. Chen, Y. Li, Y. Wang, G. Liu, K. Yu and Y. Yan, Materials Research Express **6** (8), 086329 (2019).
121. Q. Jin, Y. Pu, C. Wang, Z. Gao, Y. Wang, H. Zheng and M. Yao, Materials Letters **188**, 159-161 (2017).
122. H. Yang, F. Yan, Y. Lin and T. Wang, Applied Physics Letters **111** (25), 253903 (2017).
123. H. Yang, F. Yan, Y. Lin and T. Wang, Journal of the European Ceramic Society **38** (4), 1367-1373 (2018).
124. X. Kong, L. Yang, Z. Cheng and S. Zhang, Journal of the American Ceramic Society **103** (3), 1722-1731 (2020).
125. R. H. Dungan and R. D. Golding, Journal of the American Ceramic Society **47** (2), 73-76 (1964).
126. M.-H. Zhang, L. Fulanović, S. Egert, H. Ding, P. B. Groszewicz, H.-J. Kleebe, L. Molina-Luna and J. Koruza, Acta Materialia **200**, 127-135 (2020).
127. Y. Fan, W. Wang and J. Zhao, Ceramics International **46** (8, Part B), 12269-12274 (2020).
128. Y. Xu, Y. Guo, Q. Liu, G. Wang, J. Bai, J. Tian, L. Lin and Y. Tian, Journal of the European Ceramic Society **40** (1), 56-62 (2020).
129. K. Han, N. Luo, S. Mao, F. Zhuo, X. Chen, L. Liu, C. Hu, H. Zhou, X. Wang and Y. Wei, Journal of Materiomics **5** (4), 597-605 (2019).
130. N. Luo, K. Han, F. Zhuo, C. Xu, G. Zhang, L. Liu, X. Chen, C. Hu, H. Zhou and Y. Wei, Journal of Materials Chemistry A **7** (23), 14118-14128 (2019).
131. A. Song, J. Song, Y. Lv, L. Liang, J. Wang and L. Zhao, Materials Letters **237**, 278-281 (2019).
132. Z. Yan, D. Zhang, X. Zhou, H. Qi, H. Luo, K. Zhou, I. Abrahams and H. Yan, Journal of Materials Chemistry A **7** (17), 10702-10711 (2019).
133. R. W. Johnson, J. L. Evans, P. Jacobsen, J. R. Thompson and M. Christopher, IEEE Transactions on Electronics Packaging Manufacturing **27** (3), 164-176 (2004).
134. H. Wang, Y. Ge and L. Shi, Natural Gas Industry B **4** (5), 319-326 (2017).
135. R. Roy, R. C. Devries, D. E. Lase, M. W. Shafer and E. F. Obsorn, The Pennsylvania State College, School of Mineral Industries, Eighth Quarterly Progress Report, 16 (1953).
136. I. P. Raevskii, L. M. Proskuryakova, L. A. Reznichenko, E. K. Zvorykina and L. A. Shilkina, Soviet Physics Journal **21** (2), 259-261 (1978).
137. S. Ito, T. Kokubo and M. Tashiro, Bulletin of the Institute for Chemical Research, Kyoto University **52** (5-6), 641-651 (1975).
138. D.-K. Kwon, Y. Goh, D. Son, B.-H. Kim, H. Bae, S. Perini and M. Lanagan, Journal of Electronic Materials **45** (1), 631-638 (2016).
139. R. Zuo, H. Qi, J. Fu, J.-F. Li and L. Li, Applied Physics Letters **111** (13), 132901 (2017).
140. M. Ben Mrad, R. Hannachi, M. Dammak, N. Abdelmoula, S. Zghal and H. Khemakhem, Materials Today Communications **24**, 101223 (2020).
141. Y. Goh, B.-H. Kim, H. Bae and D.-K. Kwon, J. Korean Ceram. Soc **53** (2), 178-183 (2016).
142. M. Y, S. H and H. S, (1973).
143. J. T. Zeng, K. W. Kwok and H. L. W. Chan, Journal of the American Ceramic Society **89** (9), 2828-2832 (2006).
144. Y.-t. Sakamoto, W. Ichihara and W. Sakamoto, Japanese Journal of Applied Physics **60** (SF), SFFC03 (2021).
145. U. Miki, W. Takayuki and M. Shunsuke, (2019).

146. S. Murakami, T. Watanabe and K. Makoto, (2012).
147. T. Watanabe, S. Murakami and M. Ueda, (2016).
148. R. Zuo, H. Qi, J. Fu, J. Li, M. Shi and Y. Xu, Applied Physics Letters **108** (23), 232904 (2016).
149. S.-T. Zhang, M.-H. Lu, Y.-F. Chen, Z.-G. Liu, N.-B. Ming, J. Wang and G.-X. Cheng, Applied Physics Letters **88** (9), 092901 (2006).
150. S. Yamazoe, S. Oda, H. Sakurai, H. Adachi and T. Wada, Journal of the Ceramic Society of Japan **117** (1361), 66-71 (2009).
151. Y.-i. Hamazaki, W. Sakamoto, M. Moriya and T. Yogo, Japanese Journal of Applied Physics **48** (9S1), 09KA08 (2009).
152. P. Zhao, L. Li and X. Wang, Microstructures **3** (1), 2023002 (2023).
153. V. Buscaglia and C. A. Randall, Journal of the European Ceramic Society **40** (11), 3744-3758 (2020).
154. G. Mie, Annalen der Physik **330** (3), 377-445 (1908).
155. Bettersize.
156. S. GmbH.
157. A. A. Coelho, Journal of Applied Crystallography **51** (1), 210-218 (2018).
158. R. W. Cheary, A. A. Coelho and J. P. Cline, Journal of Research of the National Institute of Standards and Technology **109** (1), 1 (2004).
159. P. Graves and D. Gardiner, Springer **10**, 978-973 (1989).
160. L. Agilent, (Agilent Technologies, Inc, 2005).
161. K. Tehnologies, (Application Note, 2003).
162. X. Liu, Z. Feng and L. Qi, IET Science, Measurement & Technology **15** (2021).
163. A. K. Jonscher, Nature **267** (5613), 673-679 (1977).
164. P. Lunkenheimer and A. Loidl, Physical review letters **91** (20), 207601 (2003).
165. C. Tsonos, Current Applied Physics **19** (4), 491-497 (2019).
166. R. H. Chen, R. Y. Chang and S. C. Shern, Journal of Physics and Chemistry of Solids **63** (11), 2069-2077 (2002).
167. C. Tsonos, in *Journal of Composites Science* (2022), Vol. 6.
168. M. R. Shoar Abouzari, F. Berkemeier, G. Schmitz and D. Wilmer, Solid State Ionics **180** (14), 922-927 (2009).
169. T. Kaplan, L. J. Gray and S. H. Liu, Physical Review B **35** (10), 5379-5381 (1987).
170. S. M. Rezaei Niya and M. Hoorfar, Electrochimica Acta **188**, 98-102 (2016).
171. B. E. McNealy and J. L. Hertz, Solid State Ionics **256**, 52-60 (2014).
172. S. J. Cooper, A. Bertei, D. P. Finegan and N. P. Brandon, Electrochimica Acta **251**, 681-689 (2017).
173. M. Janssen and J. Bisquert, The Journal of Physical Chemistry C **125** (28), 15737-15741 (2021).
174. M. Alotaibi, L. Li and A. R. West, Physical Chemistry Chemical Physics **23** (45), 25951-25960 (2021).
175. C. B. Sawyer and C. H. Tower, Physical Review **35** (3), 269-273 (1930).
176. L. Jin, F. Li and S. Zhang, Journal of the American Ceramic Society **97** (1), 1-27 (2014).
177. J.-H. Park, B.-K. Kim, J.-G. Park, I.-T. Kim, H.-J. Je, Y. Klm and S. J. Park, Ferroelectrics **230** (1), 151-156 (1999).
178. C. Neusel, H. Jelitto and G. A. Schneider, Journal of Applied Physics **117** (15), 154902 (2015).
179. F.-C. Chiu, Advances in Materials Science and Engineering **2014**, 578168 (2014).
180. M. Li, M. J. Pietrowski, R. A. De Souza, H. Zhang, I. M. Reaney, S. N. Cook, J. A. Kilner and D. C. Sinclair, Nature Materials **13** (1), 31-35 (2014).
181. M. Cherry, M. S. Islam and C. R. A. Catlow, Journal of Solid State Chemistry **118** (1), 125-132 (1995).
182. M. Z. Ouafae. El ghadraoui, Farid.Abdi, Taj-dine. Lamcharfi, Hamza. Bali, El houssine. El ghadraoui and Michel. Aillerie, International Journal of Current Research **8** (12), 42815-42820 (2016).
183. S. H. Cha and Y. H. Han, Japanese Journal of Applied Physics **45** (10R), 7797 (2006).

184. H. Kishi, N. Kohzu, J. Sugino, H. Ohsato, Y. Iguchi and T. Okuda, Journal of the European Ceramic Society **19** (6-7), 1043-1046 (1999).
185. J. Pokorný, U. M. Pasha, L. Ben, O. P. Thakur, D. C. Sinclair and I. M. Reaney, Journal of Applied Physics **109** (11), 114110 (2011).
186. Y. I. Yuzyuk, Physics of the Solid State **54** (5), 1026-1059 (2012).
187. C. Long, Q. Chang, Y. Wu, W. He, Y. Li and H. Fan, Journal of Materials Chemistry C **3** (34), 8852-8864 (2015).
188. Y. Shimakawa, Y. Kubo, Y. Nakagawa, T. Kamiyama, H. Asano and F. Izumi, Applied Physics Letters **74** (13), 1904-1906 (1999).
189. S.-H. Yoon, J.-H. Lee, D.-Y. Kim and N. M. Hwang, Journal of the American Ceramic Society **85** (12), 3111-3113 (2002).
190. A. J. Chiquito, C. A. Amorim, O. M. Berengue, L. S. Araujo, E. P. Bernardo and E. R. Leite, Journal of Physics: Condensed Matter **24** (22), 225303 (2012).
191. G. Gouget, F. Mauvy, U. C. Chung, S. Fourcade, M. Duttine, M.-D. Braida, T. L. Mercier and A. Demourgues, Advanced Functional Materials **30** (11), 1909254 (2020).
192. H. Ogihara, C. A. Randall and S. Trolier-McKinstry, Journal of the American Ceramic Society **92** (8), 1719-1724 (2009).
193. D. Li, Z.-Y. Shen, Z. Li, W. Luo, F. Song, X. Wang, Z. Wang and Y. Li, Journal of Materials Chemistry C **8** (23), 7650-7657 (2020).
194. X. Liu, T. Yang and W. Gong, Journal of Materials Chemistry C **9** (36), 12399-12407 (2021).